From Knowledge to Wisdom

JEPE

ISSN 1934-8975 (Print)
ISSN 1934-8983 (Online)
DOI:10.17265/1934-8975

Journal of Energy and Power Engineering

Volume 9, Number 8, August 2015

David Publishing Company
www.davidpublisher.com

Journal of Energy and Power Engineering

Volume 9, Number 8, August 2015 (Serial Number 93)

David Publishing Company
www.davidpublisher.com

Publication Information:
Journal of Energy and Power Engineering is published monthly in hard copy (ISSN 1934-8975) and online (ISSN 1934-8983) by David Publishing Company located at 1840 Industrial Drive, Suite 160, Libertyville, IL 60048, USA.

Aims and Scope:
Journal of Energy and Power Engineering, a monthly professional academic journal, covers all sorts of researches on Thermal Science, Fluid Mechanics, Energy and Environment, Power System and Automation, Power Electronic, High Voltage and Pulse Power, Sustainable Energy as well as other energy issues.

Manuscripts and correspondence are invited for publication. You can submit your papers via Web Submission, or E-mail to energy@davidpublishing.com or info@davidpublishing.com. Submission guidelines and Web Submission system are available at www.davidpublisher.com.

Editorial Office:
1840 Industrial Drive, Suite 160, Libertyville, IL 60048, USA
E-mail: energy@davidpublishing.com; energy@davidpublishing.org; energy-power@hotmail.com; energy@davidpublishing.net.

Abstracted / Indexed in:
Database of EBSCO, Massachusetts, USA
Database of Cambridge Science Abstracts (CSA), USA
Chinese Database of CEPS, American Federal Computer Library Center (OCLC), USA
Ulrich's Periodicals Directory
Summon Serials Solutions
Chinese Scientific Journals Database, VIP Corporation, Chongqing, China
Chemical Abstracts Service (CAS)
ProQuest
CNKI
Google Scholar

Subscription Information:
Price:
Print $800 (per year)
Online $600 (per year)
Print and Online $880 (per year)

David Publishing Company
Tel: 1-323-984-7526, 001-323-410-1082; Fax: 1-323-984-7374; 323-908-0457
E-mail: order@davidpublishing.com
Digital Cooperative Company: www.bookan.com.cn

David Publishing Company
www.davidpublisher.com

Journal of Energy and Power Engineering

Volume 9, Number 8, August 2015 (Serial Number 93)

Contents

Clean and Sustainable Energy

Journal of Energy and Power Engineering 9 (2015) 679-686
doi: 10.17265/1934-8975/2015.08.001

Numerical Simulation of Char Particle Gasification

Syed Shabbar Raza[1], Isam Janajreh[1], Rizwan Ahmed[2] and Ashjan AlKatheeri[2]

1. Waste to Energy Lab, Masdar Institute of Science and Technology, Abu Dhabi 54224, UAE

2. Takreer Research Center, Abu Dhabi 3593, UAE

Received: June 15, 2015 / Accepted: July 17, 2015 / Published: August 31, 2015.

Abstract: A first principal modeling of the gasification of a char particle is performed using single step mechanism. The char particle is considered to be spherical in shape and only the physical and chemical properties can change in the radial direction. The carbon dioxide is used as the gasification agent that reacts with the char and form carbon monoxide. The presence of both solid and gaseous phase species makes the reaction heterogeneous. The char particle is considered with varying porosity that also allows the change in the surface area of the particle. A time invariant temperature and pressure profile is used at which the Arrhenius rate constant and diffusion is calculated. The mass conservation of model results in the form of two coupled partial differential and one ordinary differential equation. The equations are solved with a set of initial and boundary conditions using the bulk species concentration at the particle surface. A second order accurate central differencing scheme is used to discretize space while backward differencing is used to discretize time. Finally, the results are presented for the concentration distribution of CO and CO_2 in radial direction with respect to time. It shows that, maximum concentration of CO is present at the center of the particle while the concentration gradient becomes higher near the particle surface. The nonlinear concentration trend due to the diffusion is effectively captured. The results show that, completed conversion of char depend upon the time provided for the reaction which can be reduced by decreasing the size of particle or increasing the reaction temperature. The sensitivity study of temperature and initial porosity also performed and showed that temperature has high impact on char conversion as compare to initial porosity.

Key words: Coal, particle conversion, biomass, porosity, CO_2 gasification.

1. Introduction

Char gasification is one of the important processes to generate fuel, electricity and variety of chemical. Char is normally generated by de-volatalizing coal or biomass at high temperature to remove its moisture and volatile contents [1]. Then this porous char can be reacted with gasification agent i.e., air, oxygen, steam, CO_2 etc. to produce a useful syngas product, i.e., CO and H_2. Ash is also a compulsory part of the char and its quantity depends upon the type of coal or biomass used to produce the char.

Char can be derived from any carbonaceous material that includes mainly coal and biomass. The primary constituent of char is carbon and it is directly related to the amount of carbon present in the carbonaceous material. Fig. 1 shows the H/C and O/C ratios for coal, lignite, peat and biomass. It is clearly evident from the figure that both H/C and O/C ratios for coal are lower than that off the biomass and as a results a higher heating value according to Channiwala's formula [2]. It means that, coal have high percentage of carbon present as compare to biomass. The ultimate analysis for coal and biomass presented in Table 1 which carried elsewhere [3] demonstrate the higher percentage of carbon in coal as compare to pine needle biomass.

But this high percentage of carbon is not the only criteria to select coal or the other feedstock for the high yield of char. As the char represents the solid form of carbon, therefore it is necessary to know the percentage of solid or fixed carbon presents in coal and biomass. Table 2 shows the proximate analysis (as received) of coal and biomass that fraction the feedstock into

Corresponding author: Isam Janajreh, associate professor, research fields: chemical reaction engineering, gasification, computational mechanics and aerodynamics. E-mail: ijanajreh@masdar.ac.ae.

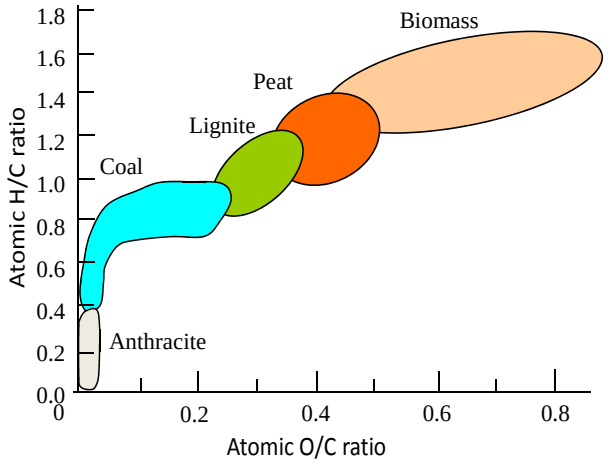

Fig. 1 Van Krevelen diagram.

Table 1 Ultimate analysis of coal and biomass.

	Coal	Pine needles
C wt.%	82.17	48.58
H wt.%	5.60	6.30
O wt.%	8.60	43.64
N wt.%	2.50	1.48
S wt.%	1.13	0

Table 2 Proximate analysis of coal and biomass (as received).

	Coal	Pine needles
Moisture wt.%	0.30	9.01
Volatile wt.%	37.81	44.58
Fixed carbon wt.%	54.65	42.28
Ash wt.%	7.22	4.12

moisture, volatiles, fixed carbon and ash fractions that present in the sample.

The result of proximate analysis shows the higher percentage of fixed carbon present in coal as compare to biomass. This clearly indicates this tested grade of coal as a better choice to produce high quantity char per unit weight of feedstock. On other hand, biomass exhibit higher quantity of volatile material which is expected to yield a high porous char as biomass particle agglomerate, baked, through the de-moisturization and de-volatilization processes. This high porosity provides more surface area inside the pores for reaction to occur. Therefore, it is kind of trade-off to produce char using fixed-carbon rich coal or high-volatile biomass.

The modelling of coal de-volatilization, combustion and gasification in the form comprehensive model and CFD (computational fluid dynamic) code are already performed in Waste to Energy Lab at Masdar Institute, Abu Dhabi with variety of different feedstock [3-9]. The similar modelling techniques that are used for coal or biomass cannot be used directly for char due to the large difference in the physical and chemical properties. Reaction kinetics of char is much simpler than coal/biomass as its main composition is carbon.

A considerable amount of literature is available in which gasification of char is presented. Kim, et al. [10] prepared char from 12 different bituminous coals at different reaction temperature for the gasification with CO_2 under isothermal conditions. The concentration of CO and CO_2 measured using online gas analyser. The results show that, the reactivity is increased as the particle size decreases at the given temperature. Modelling of char gasification performed that accounts for the shrinking core model better for large particle size while the volumic reaction model is also more suitable for smaller particle size. Singer, et al. [11] developed an adaptive random pore model for the application to the char gasification. This model allows different pore sizes to grow at different rates at a given location within a reacting porous particle. The model satisfactory reproduce some coal char oxidation experiments from the literature, however because of the complexity of the model no attempt to integrate it to reactive flow environment is pursued. Seo, et al. [12] use volume of reaction model, shrinking core model and random pore model to interpret the experimental data for biomass char CO_2 gasification. The result presented in term of CO and CO_2 yield at different operating conditions. The final comparison shows that, random pore model agreed with the experimental data more than the other two models. Suresh, et al. [13] performed palm shell char gasification using CO_2 through TGA (thermo gravimetric analyser) at temperature ranging from 800 °C to 1,000 °C. Four different models are used to identify the correct pattern of experimental data and based on RMSE (root mean

square error) the random pore model is found in good agreement with the data.

In this research study, an attempt is made to build a model for char particle gasification. The main motivation behind modelling is to develop a simplified approach so that it can further integrate with commercial CFD software at low computational expenses. This integration will help to run the large number of discrete particle simulation in a single step. The model used in this study comprise of a single heterogeneous reaction which represent the CO_2 gasification. A constant value of temperature and pressure is used throughout the domain. Finally, the results are presented in term of the yield of CO and CO_2.

2. Physical and Computational Model

Gasification is a complex process that occurs inside the pores of the particle. There are several chemical and physical processes taking place inside the particle. The reactants diffuse inside the particle and reacts with the char and multiple heterogeneous and homogeneous reactions occur. Due to the reaction, the size and shape of the pores are continuously changing which also change the physical shape of the char particle. Combining both chemical and physical process makes the char gasification quite complex and hence the need of modelling this process is necessary for understanding the evolution of the syngas species.

By considering char as coal or biomass, a primary gasification reaction can be written as follow:

$$\mathrm{CH}_x\mathrm{O}_y\mathrm{N}_z + l(\mathrm{O}_2 + 3.76\mathrm{N}_2) + m\,\mathrm{H}_2\mathrm{O} + n\,\mathrm{CO}_2 \rightarrow x_1\,\mathrm{CO} + x_2\mathrm{H}_2 + x_3\mathrm{CH}_4 + x_4\mathrm{CO}_2 + x_5\mathrm{H}_2\mathrm{O} + 3.76l\,\mathrm{N}_2 \quad (1)$$

where, x, y, z and l, m, n, x_1, x_2, x_3, x_3 and x_5 are the respective moles of each element and component per mole of carbon in the system.

The above reaction shows that, gasification can be achieved by using the combination of air, H_2O and CO_2 as oxidizer and moderator, but, it is not necessary, either anyone of them can be used. This primary gasification reaction can be split into numbers of intermediate reaction and the most important reaction are given below:

char reforming:

$$\mathrm{C} + \mathrm{H}_2\mathrm{O} = \mathrm{CO} + \mathrm{H}_2 + 131\frac{MJ}{Kmole} \quad (2)$$

boudouard reaction:

$$\mathrm{C} + \mathrm{CO}_2 = 2\mathrm{CO} + 172\frac{MJ}{Kmole} \quad (3)$$

methane cracking-hydro gasification:

$$\mathrm{C} + 2\mathrm{H}_2 = \mathrm{CH}_4 - 75\frac{MJ}{Kmole} \quad (4)$$

methane reformation:

$$\mathrm{CH}_4 + \mathrm{H}_2\mathrm{O} = \mathrm{CO} + 3\mathrm{H}_2 + 206\frac{MJ}{Kmole} \quad (5)$$

water gas shift reaction:

$$\mathrm{CO} + \mathrm{H}_2\mathrm{O} = \mathrm{CO}_2 + \mathrm{H}_2 - 41\frac{MJ}{Kmole} \quad (6)$$

In this study, the physical model is based on the gasification of a char particle. The char particle normally is the yield of high temperature devolatilization of coal or biomass particle. These particles have porous structure throughout. The reactant moves inside the pores during the reaction and product species move outside. The heterogeneous reaction takes place at the surface of the particle while the homogenous reaction occurs inside the pores and outside the particle.

To develop a simplified model only a heterogeneous reaction is considered that represents the CO_2 gasification of the char particle, as given by Eq. (3). This reaction is commonly known as boudouard reaction and represents the gasification of char by carbon dioxide.

Eq. (3) shows one solid phase (C/char) and two gas phase species (CO and CO_2). The governing equations to model the physical system of gasification can be represented by mass conservation in both solid and gas phase reaction, as given below:

$$\frac{\partial(\phi C_{\mathrm{CO}})}{\partial \mathrm{t}} = \frac{1}{r^2}\frac{\partial}{\partial r}\left(r^2 D_{eff}(\phi)\frac{\partial C_{\mathrm{CO}}}{\partial \mathrm{r}}\right) + f_1\left(C_{\mathrm{CO}_2}, C_{\mathrm{CO}}, \phi\right) \quad (7)$$

$$\frac{\partial(\phi C_{\mathrm{CO_2}})}{\partial t} = \frac{1}{r^2}\frac{\partial}{\partial r}\left(r^2 D_{eff}(\phi)\frac{\partial C_{\mathrm{CO_2}}}{\partial r}\right) + f_2\left(C_{\mathrm{CO_2}}, \phi\right) \tag{8}$$

$$\frac{\mathrm{d}X}{\mathrm{d}t} = f_3\left(C_{\mathrm{CO_2}}, \phi\right) \tag{9}$$

where, ϕ represents the porosity of the particle; C_i represents the concentration of gas phase species; *r* and *t* represents the radial and time coordinate, respectively; D_{eff} represents the effective diffusivity; f_i represents the source term due to reaction and *X* represents the conversion of char. Eqs. (7) and (8) represent partial differential equation showing the reaction-diffusion model for the gas phase species. Eq. (9) represents an ordinary differential equation for the conversion of char.

The porosity of the particle can be represented in term of initial porosity (ϕ_0) and char conversion, and is written as:

$$\phi(r,t) = \phi_0 + (1-\phi_0)X(r,t) \tag{10}$$

Similarly the effective diffusion is given as,

$$D_{eff}(r,t) = D\phi^2\,(r,t) \tag{11}$$

The reaction source term is given as,

$$f_i = (1-\phi_0)S\,k_{rxn}C_{\mathrm{CO_2}}\nu_i \tag{12}$$

where, ν_i is the stoichiometric coefficient; *S* is the surface area; k_{rxn} is the Arrhenius rate constant i.e., $k_{rxn} = 4364\,\mathrm{e}^{-\frac{29844}{T}}$; *T* is the temperature (K). The surface area of the particle is represented by its initial surface area (S_0) and the char conversion:

$$S = S_0\left(1 - X(r,t)\right) \tag{13}$$

By substituting Eqs. (10)-(13) in Eqs. (7)-(9) and after simplification the following equations are written as:

$$\left((1-\phi_0)X(r,t)+\phi_0\right)\frac{\partial C_{\mathrm{CO}}}{\partial t} = \frac{1}{r^2}\frac{\partial}{\partial r}\left(r^2 D\left((1-\phi_0)X(r,t)+\phi_0\right)^2\frac{\partial C_{\mathrm{CO}}}{\partial r}\right) + C_{\mathrm{CO_2}}k_{rnx}S_0\left(1-X(r,t)\right)(1-\phi_0)\left(\nu_{\mathrm{CO}} + \frac{M_{\mathrm{c}}C_{\mathrm{CO}}}{\rho_{\mathrm{C}}(1-\phi_0)}\nu_{\mathrm{C}}\right) \tag{14}$$

$$\left((1-\phi_0)X(r,t)+\phi_0\right)\frac{\partial C_{\mathrm{CO_2}}}{\partial t} = \frac{1}{r^2}\frac{\partial}{\partial r}\left(r^2 D\left((1-\phi_0)X(r,t)+\phi_0\right)^2\frac{\partial C_{\mathrm{CO_2}}}{\partial r}\right) + C_{\mathrm{CO_2}}k_{rnx}S_0\left(1-X(r,t)\right)(1-\phi_0)\left(\nu_{\mathrm{CO_2}} + \frac{M_{\mathrm{c}}C_{\mathrm{CO_2}}}{\rho_{\mathrm{C}}(1-\phi_0)}\nu_{\mathrm{C}}\right) \tag{15}$$

$$\frac{\mathrm{d}X(r,t)}{\mathrm{d}t} = -\frac{M_{\mathrm{c}}}{\rho_{\mathrm{c}}}\nu_{\mathrm{c}}k_{rxn}S_0\left(1-X(r,t)\right)\mathrm{C}_{\mathrm{CO_2}} \tag{16}$$

where, M_{c} is the molecular weight of carbon and ρ_{C} is its density. The diffusion is calculated using the Reid's formula [14] and is given as:

$$D = \frac{\left(1\times10^{-7}T^{1.75}\right)}{Pressure\times\left(AD_{CO}^{\frac{1}{3}}+AD_{\mathrm{CO_2}}^{\frac{1}{3}}\right)^2}\sqrt{\frac{\left(MW_{\mathrm{CO}}+MW_{\mathrm{CO_2}}\right)}{MW_{\mathrm{CO}}\times MW_{\mathrm{CO_2}}}} \tag{17}$$

where, *AD* is the atomic diffusion for the gases.

The values of the constants used in Eqs. (14)-(17) are given in Table 3.

3. Initial Conditions and Boundary Conditions

Eqs. (14)-(16) give us to represent a system of two coupled partial differential equations and one ordinary differential equation. As the particle is assumed to be perfectly spherical and all physical properties are either constant or changing in the radial direction. To solve the differential equations, a set of initial and boundary conditions are used. Dirichlet/symmetry (zero gradient) boundary condition is used at the center ($r = 0$) while Neumann boundary condition is used at the surface ($r = R$) and are written as:

$$@r = 0 \qquad \frac{\partial C_i(0,\ t)}{\partial r} = 0 \tag{18}$$

$$@r = R,\ C_{\mathrm{CO}}(R,t) = 100\,\frac{\mathrm{mol}}{\mathrm{m^3}} \text{ and } C_{\mathrm{CO_2}} = 50\,\frac{\mathrm{mol}}{\mathrm{m^3}} \tag{19}$$

The boundary condition of Eq. (14) is actually the gasification condition calculated at temperature and pressure mentioned in Table 3. The initial conditions are taken as uniform values of gas species concentration mentioned in Eq. (19). A second order central difference scheme is used to solve the equation in space and backward marching scheme is used for the time.

Table 3 Value of the constants used in Eqs. (7)-(17).

Name	Unit	Value
ϕ_0	-	0.2
S_0	m^2/m^3	2,267E5
M_c	gm/mol	12
ρ_c	kg/m^3	2,267
ν_C	-	1
ν_{CO}	-	2
ν_{CO_2}	-	1
MW_{CO}	gm/mol	28
MW_{CO_2}	gm/mol	44
AD_{CO}	cm^2/s	18.9
AD_{CO_2}	cm^2/s	26.9
T (temperature)	K	1,600
P (pressure)	atm	20
R	μm	100

4. Results and Discussion

The mass conservation of CO and CO_2 is depending upon the diffusion and the source terms due to the Arrhenius base kinetics. As the temperature of the particle is held constant this in turns makes the k_{rxn} a constant in Eqs. (14)-(16). Also, the diffusion calculated from Eq. (17) is constant throughout the simulation. These assumptions make the problem quite simpler and only the concentration of gases and char conversion left as the unknowns.

The result of the concentration of CO is given in Fig. 2. It shows that, initially, the concentration of particle maintain profile having the concentration of around 200 mol/m^3 at the particle center. As the time progress, the concentration of CO decrease and reach to a value of 100 mol/m^3 at the end of the simulation time. This is because the temperature of the particle is maintained at a constant value which makes a constant diffusion flux outside the particle, eventually when all char is converted into CO the bulk value concentration of CO propagate inside the particle.

Fig. 3 shows the CO_2 concentration inside the particle. It shows that, as the simulation starts the concentration of CO_2 suddenly decrease to a minimum value of nearly zero at the center of particle. This is because of the high conversion of CO_2 and char into CO. As the boundary of particle having a fixed concentration of CO_2, therefore, it forces the solution to maintain that value all the time. When almost all the char depleted the concentration of CO_2 inside the particle becomes the bulk concentration.

Fig. 4 shows the char conversion along the radial direction. It clearly shows the increase in conversion

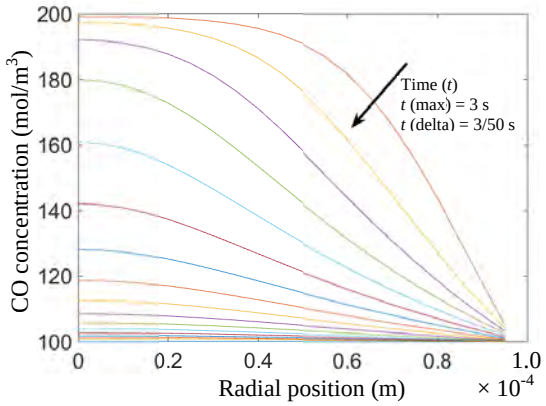

Fig. 2 CO concentration along radial direction as time is progressing.

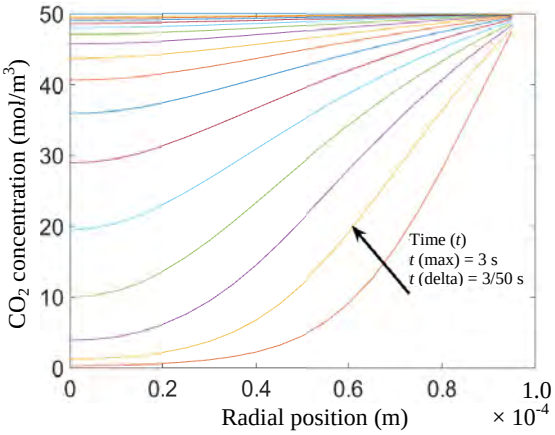

Fig. 3 CO_2 concentration along radial direction as time is progressing.

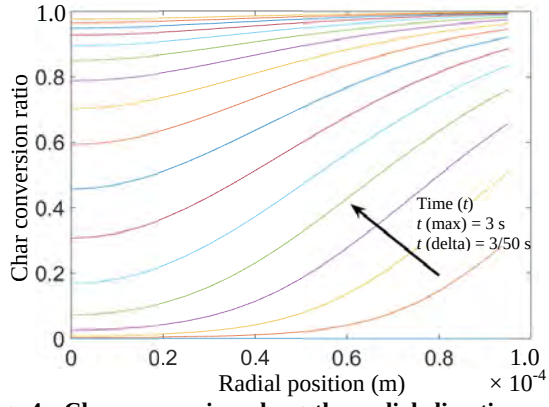

Fig. 4 Char conversion along the radial direction as the time is progressing.

with the simulation time. The total simulation time is 3 s which is sufficiently long, but not enough to ensure all the char present in the particle is fully converted into CO. Also, the steeper curve near the surface of the particle shows that, the conversion of char also depends upon the size of the particle. If the size of the particle is taken smaller complete char conversion can be achieved in a lesser time.

The sensitivity study of temperature is also performed to show the effect of temperature on char conversion. For that purpose, an increasing temperature is applied for the time duration of 3 s and presented in Figs. 5 and 6. The temperature sensitivity is performed using the 10 different jumps starting from 1,000 K to 2,000 K and the end result of the simulation is presented.

Fig. 5 shows the CO concentration along radial direction as function of the temperature increase. It shows that, the temperature is directly proportional to the CO concentration i.e., as the temperature increase, the concentration of CO concentration is also increase. The concentration of CO at the outer surface is constant, due to the fixed boundary condition. Similarly, Fig. 6 shows the CO_2 concentration along the radial direction as temperature increases. It shows that, as the temperature increase, the concentration of CO_2 decrease. It is due to the fact that, the increasing temperature directly affects the Arrhenius rate constant and because only forward reaction is considered therefore the CO_2 concentration decrease.

Fig. 7 shows the char conversion along the radial direction with respect to the temperature. It shows that, temperature has a high effect on the conversion of char particle. As the temperature increase the more char is reacted with the CO_2 in the simulation time of 3 s.

Any decrease in the reaction temperature is associated with substantial decrease in the char conversion.

Fig. 8 shows the CO concentration along the radial direction for the sensitivity analysis of initial porosity. The simulation time and temperature is kept similar to baseline case i.e., 3 s and 1,600 K. The result shows that, the change of porosity has impact on CO concentration. Although the scale of this impact is considerably less those of the temperatures change. It shows that, as the porosity decrease, the CO concentration increase. It is due to the fact that, the decrease porosity increases the amount of char present

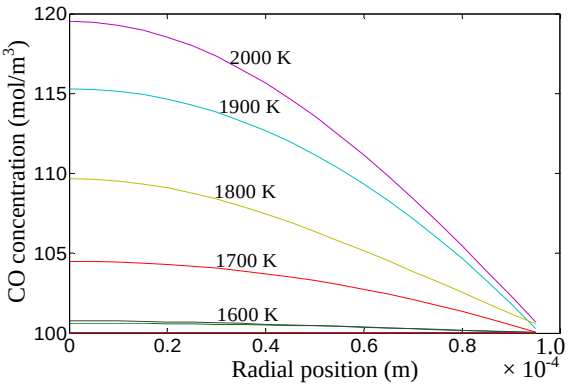

Fig. 5 CO concentration along radial direction as temperature increases.

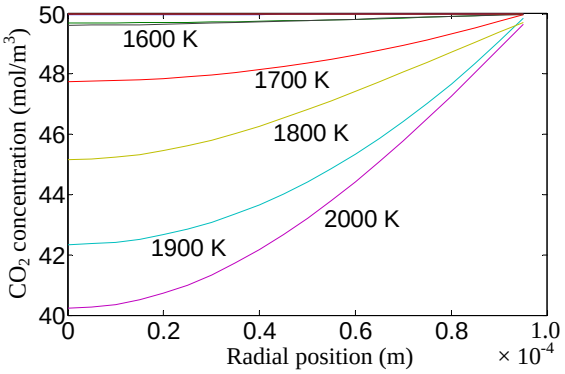

Fig. 6 CO_2 concentration along radial direction as temperature increases.

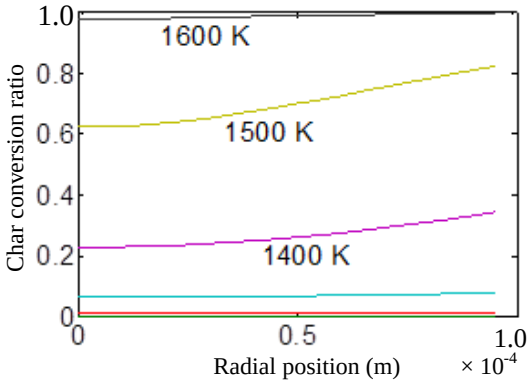

Fig. 7 Char conversion along radial direction as temperature increases.

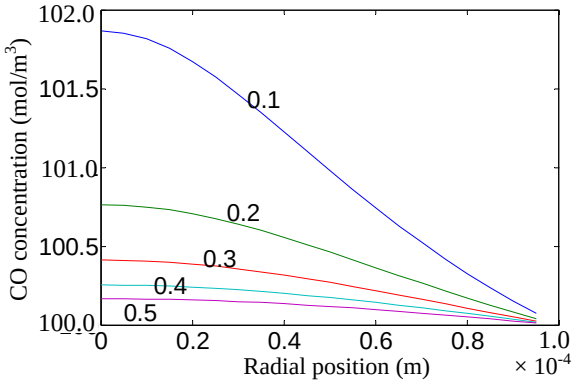

Fig. 8 CO concentration along radial direction for the sensitivity analysis of initial porosity (0.1-0.5).

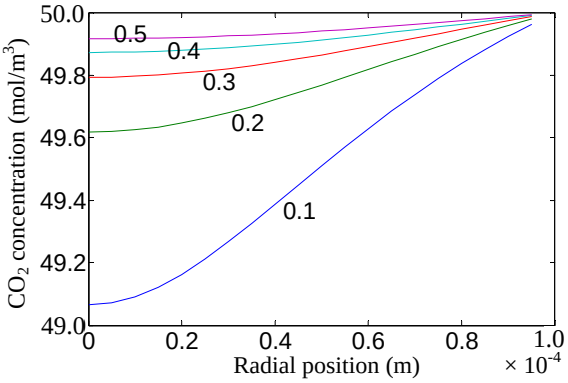

Fig. 9 CO_2 concentration along radial direction for the sensitivity analysis of initial porosity (0.1-0.5).

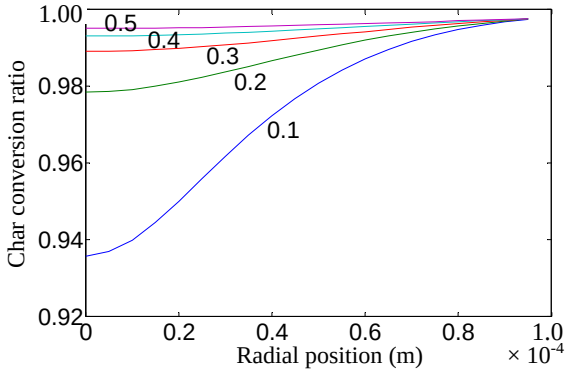

Fig. 10 Char conversion along radial direction for the sensitivity analysis of initial porosity (0.1-0.5).

inside the particle which ultimately increase the amount of CO produce.

Fig. 9 shows the CO_2 concentration for the sensitivity study of initial porosity. It shows that increase in porosity decreases the concentration of CO_2 inside the particle. Although the change in concentration inside the particle is considerably low. Fig. 10 shows the char conversion in the radial direction. It shows the increase in porosity of particle increases the char conversion.

5. Conclusions

Gasification is one of the important energy conversion methods for the energy production. Although the complexity involved in understanding the chemical kinetics make it very difficult to model and simulate. There are number and variety of models are present in the literature that uses different approach to model the gasification process. In this research, a simplified model is used to simulate the gasification of char particle. The basic idea to develop the model is to build a single reaction mechanism in the form of transport equation with coupled diffusion dependent and reaction source term. The model comprise of two coupled partial differential equations and one ordinary differential equation that are solve simultaneously subjected to proper initial and boundary conditions. The results are calculated for the char particle in the radial direction that simulates the gasification process at high temperature and pressure. It shows that, the concentration of CO decrease with time and the maximum concentration always lie at the centre of the particle. On the other hand, the concentration of CO_2 increase with time and eventually that all the char can be gasified into CO. This is contingent upon the availability of sufficient reaction time or a reduction in the particle size. The sensitivity study of temperature shows that, the concentration of CO increase as the temperature increase and the concentration of CO_2 decrease as the temperature increase. The sensitivity study of initial porosity shows that, it has considerably low effect on char conversion by any increase in it directly proportional to the char particle conversion.

Acknowledgments

The financial support of MIST (Masdar Institute) and TRC (Takreer Research Centre) is highly acknowledged.

References

[1] Bae, J. S., Lee, D. W., Park, S. J., Lee, Y. J., Hong, J. C., and Han, C. 2013. "Synthesis Gas and Char Production from Mongolian Coals in the Continuous Devolatilization Process." *Korean Journal of Chemical Engineering* 30 (2): 321-6.

[2] Channiwala, S., and Parikh, P. 2002. "A Unified Correlation for Estimating HHV of Solid, Liquid and Gaseous Fuels." *Fuel* 81 (8): 1051-63.

[3] Syed, I. J. S., and Ghenai, C. 2012. "Thermodynamics Equilibrium Analysis within the Entrained Flow Gasifier Environment." *Int. J. of Thermal & Environmental Engineering* 4 (1): 47-54.

[4] Shabbar, S., and Janajreh, I. 2012. "Thermodynamic Equilibrium Analysis of Coal Gasification Using Gibbs Energy Minimization Method." *Energy Conversion and Management* 65 (January): 755-63.

[5] Janajreh, I., Syed, S., Qudaih, R., and Talab, I. 2010. "Solar Assisted Gasification: Systematic Analysis and Numerical Simulation." *Int. J. of Thermal & Environmental Engineering* 1 (2): 81-90.

[6] Janajreh, I., Raza, S. S., and Valmundsson, A. S. 2012. "Plasma Gasification Process: Modeling, Simulation and Comparison with Conventional Air Gasification." *Energy Conversion and Management* 65 (January): 801-9.

[7] Janajreh, I., and Raza, S. S. 2015. "Numerical Simulation of Waste Tyres Gasification." *Waste Management & Research* 33 (5): 460-8.

[8] Adeyemi, I., and Janajreh, I. 2015. "Modeling of the Entrained Flow Gasification: Kinetics-Based ASPEN Plus Model." *Renewable Energy* 82 (October): 77-84.

[9] Janajreh, I., Raza, S. S., and Elagroudy, S. 2015. "Co-firing of Enteromorpha Prolifera Algae and RTC Coal in a Down Draft Gasifier: Material Characterization and Flow Simulation." *The Journal of Solid Waste Technology and Management* 41 (1): 68-83.

[10] Kim, Y. T., Seo, D. K., and Hwang, J. 2011. "Study of the Effect of Coal Type and Particle Size on Char—CO_2 Gasification via Gas Analysis." *Energy & Fuels* 25 (11): 5044-54.

[11] Singer, S. L., and Ghoniem, A. F. 2011. "An Adaptive Random Pore Model for Multimodal Pore Structure Evolution with Application to Char Gasification." *Energy & Fuels* 25 (4): 1423-37.

[12] Seo, D. K., Lee, S. K., Kang, M. W., Hwang, J., and Yu, T. U. 2010. "Gasification Reactivity of Biomass Chars with CO_2." *Biomass and Bioenergy* 34 (12): 1946-53.

[13] Suresh, K. R. K., Ahmed, A., and Srinivasakannan, C. 2012. "Gasification Kinetics of Date Palm Seed Using Carbon Dioxide." *International Journal of Environmental Research* 7 (1): 97-104.

[14] Reid, R. C., Prausnitz, J. M., and Poling, B. E. 1987. *The Properties of Gases and Liquids.* New York: McGraw-Hill Education.

Journal of Energy and Power Engineering 9 (2015) 687-704
doi: 10.17265/1934-8975/2015.08.002

Temperature Distributions in Single Cell of Polymer Electrolyte Fuel Cell Simulated by an 1D Multi-plate Heat-Transfer Model and a 3D Numerical Simulation Model

Akira Nishimura[1], Masashi Baba[1], Kotaro Osada[1], Takenori Fukuoka[1], Masafumi Hirota[1] and Eric Hu[2]

1. Division of Mechanical Engineering, Graduate School of Engineering, Mie University, Tsu-city, Mie 514-8507, Japan

2. School of Mechanical Engineering, The University of Adelaide, Adelaide, SA 5005, Australia

Received: April 30, 2015 / Accepted: June 01, 2015 / Published: August 31, 2015.

Abstract: The purpose of this study is to verify an 1D multi-plate heat-transfer model estimating the temperature distribution on the interface between polymer electrolyte membrane and catalyst layer at cathode in single cell of polymer electrolyte fuel cell, which is named as reaction surface in this study, with a 3D numerical simulation model solving many governing equations on the coupling phenomena in the cell. The results from both models/simulations agreed well. The effects of initial operation temperature, flow rate, and relative humidity of supply gas on temperature distribution on the reaction surface were also investigated. It was found in both 1D and 3D simulations that, the temperature rise (i.e., $T_{react} - T_{ini}$) of the reaction surface from initial operation temperature at 70 °C was higher than that at 80 °C irrespective of flow rate of supply gas. The effect of relative humidity of supply gas on $T_{react} - T_{ini}$ near the inlet of the cell was small. Compared to the previous studies conducted under the similar operation conditions, the $T_{react} - T_{ini}$ calculated by 1D multi-plate heat-transfer model in this study as well as numerical simulation using 3D model was reasonable.

Key words: Polymer electrolyte fuel cell, 1D multi-plate heat-transfer model, 3D numerical simulation model, temperature distribution.

1. Introduction

PEFC (polymer electrolyte fuel cell) is promising clean power-generation technology. However, there are some barriers preventing PEFC from being used widely among industries and homes worldwide. Some of such barriers are the reduction in power-generation performance and life span caused by the uneven distributions of mass concentration and temperature inside cell of PEFC. Local temperature rise and gas diffusion blocked by condensed water are reasons for the uneven distribution [1-4].

This study investigates temperature distribution inside single cell of PEFC. Uneven temperature distribution causes degradations of PEM (polymer electrolyte membrane) and catalyst layer. Local temperature rise would cause thermal decomposition of PEM. PEM could be broken by thermal stress caused by the uneven temperature distribution [3, 5, 6]. Temperature distribution influences the phase change of water. Water's behavior influences the performance of the PEM and gas flows in GDL (gas diffusion layer) and catalyst layer. Temperature also affects the performance of PEM and catalyst layer. Hence, it is important to clarify the temperature distribution in single cell of PEFC in order to improve the power-generation performance and realize the long life span.

Refs. [7, 8] reported an experimental study on current density and temperature distributions in a cell

Corresponding author: Akira Nishimura, associate professor, research fields: heat transfer, fuel cell, photocatalyst and smart city. E-mail: nisimura@mach.mie-u.ac.jp.

of PEFC under several operation conditions. Refs. [7, 8] measured temperature distributions by 10 very thin thermocouples located between GDL and catalyst layer at cathode. The temperature distribution along gas channel of separator was discussed in these Refs. [7, 8]. However, the width of insulator covering thermocouple was tenth part of the gas channel width and many thermocouples were installed in the cell, resulting that the interference of thermocouples on mass, temperature and current density distributions was inevitable. Reference [9] also measured temperature distributions by the micro temperature sensor with a sensing area of 400 μm × 400 μm. Since this sensor was embedded in the cathode flow channel of separator, the temperature near the reaction surface was not measured.

In another study conducted by Nishimura, et al. [10], the temperature distributions on separator's back of single cell of PEFC were measured by thermograph. Without disturbing heat and mass transfer due to installation of sensor, the temperature distribution under power-generation conditions could be measured accurately. Based on the measuring data, the study tried to build an empirical model to predict the temperature distribution on reaction surface. According to literature survey by the study, there was no previous study on estimating the temperature distribution on reaction surface from measured temperature data at separator's back. If the heat-transfer model to predict the temperature distribution on reaction surface with the measured separator back's temperature would be developed, the temperature distribution on reaction surface could be easily estimated without difficult and complex temperature measurement.

In previous studies conducted by Nishimura, et al. [11, 12], in order to estimate the temperature distribution inside single cell of PEFC, an 1D multi-plate heat-transfer model using the temperature data of separator's back measured by thermograph under power-generation was developed. Since the single cell of PEFC consists of some components having plate shapes such as PEM, catalyst layer, GDL and separator, the previous studies by the authors [11, 12] proposed the heat-transfer model assuming the heat-transfer through multi-plates for these components of the cell. The reaction surface temperature (T_{react}) was calculated using the heat-transfer model. This is a new approach to identify the heat-transfer mechanism in single cell of PEFC by means of the data measured by the thermograph and the model developed.

Comparing the results from the model with the other heat-transfer models proposed in previous studies [13-15], there are differences among them, e.g., heat source. Ref. [13] developed a simplified 1D model, which considered for the heat-transfer from PEM, catalyst layer, anode/cathode diffusion media and backing plate, based on Fourier's thermal conduction equation. This particular model [13] considered various heat sources such as Joule heating from PEM, entropic loss, activation and concentration overpotential, and Joule heating in catalyst layer. According to Ref. [13], the difference between T_{react} and the backing plate (= separator) temperature was approximately 4.5 °C when the current density was 1.0 A/cm^2 and the backing plate end temperature was 80 °C. Ref. [14] proposed another 1D model, which considered the heat-transfer among MEA (membrane electrode assembly), catalyst layer, GDL, and carbon current collector by investigating various types of Nafion PEMs such as NER-212, Nafion 112, Nafion 115, and Nafion 117. In the model [14], the heat-transfer through the in-plane direction of the cell was neglected and that toward the through-plane direction was investigated based on Fourier's thermal conduction equation. In addition, mole enthalpy of anode and cathode supply gas, vaporization enthalpy of water and reaction enthalpy were considered [14]. The difference between T_{react} and the separator's back temperature was about 4 °C under the condition that MEA temperature was 85 °C. Ref. [15] developed a nonisothermal 2D model

that considered the heat-transfer among PEM, catalyst layer, and GDL, in which thermal conduction through the cell components was considered. Additionally, heat capacitance and heat generation/depletion parameters, including thermodynamic irreversibility, heat generation by exothermic reaction, electron and proton transport resistance, and the phase change of water, were considered for Nafion PEMs. According to Ref. [15], the difference between T_{react} and the temperature of current collector contacting the GDL at the cell voltage of 0.40 V was approximately 4 °C when using Nafion 115. Although there were differences in terms of heat-transfer calculations between the model developed by the present study and the other heat-transfer models proposed in previous studies [13-15], the temperature gradients for the targeted regions under the similar operation conditions were almost the same [11]. Thus, it can be believed that, the heat-transfer model proposed in the present study is reasonable.

The present paper focuses on comparing the temperature distribution calculated by 1D multi-plate heat-transfer model with that calculated by the other model considering the complex coupling phenomena in a cell of PEFC. If the result calculated by 1D multi-plate heat-transfer model agreed well with that from the model considering the compound effect such as fluid dynamics, gas diffusion, electrochemical reaction and heat-transfer in PEFC, it could conclude the simple 1D model which could be used to predict the coupling phenomena in PEFC.

The aim of the present paper is to prove that, the temperature distribution on the reaction surface calculated by 1D multi-plate heat-transfer model agrees with that by the numerical simulation using 3D model. For the numerical simulation, this study adopts the commercial CFD (computational fluid dynamics) software CFD-ACE+ (ESI Japan) which solves many governing equations on the coupling phenomena in a cell of PEFC such as fluid dynamics, gas diffusion, electrochemical reaction and heat-transfer at the same time. The effects of initial operation temperature, flow rate, and relative humidity of supply gas on temperature distribution on the reaction surface are investigated by the 1D model as well as the 3D model. The temperature distributions calculated by the 1D model and the 3D model are also compared with those reported by the precious studies.

2. Calculation Procedure of Temperature Distribution

2.1 1D Multi-plate Heat-Transfer Model

Fig. 1 illustrates the multi-plate single cell PEFC module used in this study. In the module, the separator back is the opposite side of surface contacting GDL. The separator's back surface temperatures $T_{surf,\ c}$ and $T_{surf,\ a}$ were measured using thermograph. In the present study, the authors used the single cell consisting of separator and current collector in the power generation experiment in order to obtain the temperature and power-generation data for modeling heat-transfer phenomena in the cell because the precious studies which were referred by the present study used separator as component of single cell, not bipolar plate.

The heat-transfer across the module is assumed to be 1D multi-layer heat-transfer. In the module, the cell is divided into a gas channel part and a rib part. In Fig. 1, the upper and lower parts represent rib part and channel part, respectively. For both parts, the heat-transfer was assumed to be in the through-plane direction. It is assumed that, the thermal convection occurs on the surfaces of gas channel contacting GDL and the opposite surface. The reaction heat generated on the reaction surface is transferred to the cathode and anode sides separately. Although the gas flowing through the gas channel from the inlet to the outlet of the cell carries away some heat, the amount of heat taken is less than 1% of the estimated reaction heat which is approximately 20 W [11]. Therefore, the heat carried away by the gas flowing through the gas channel is neglected in this model.

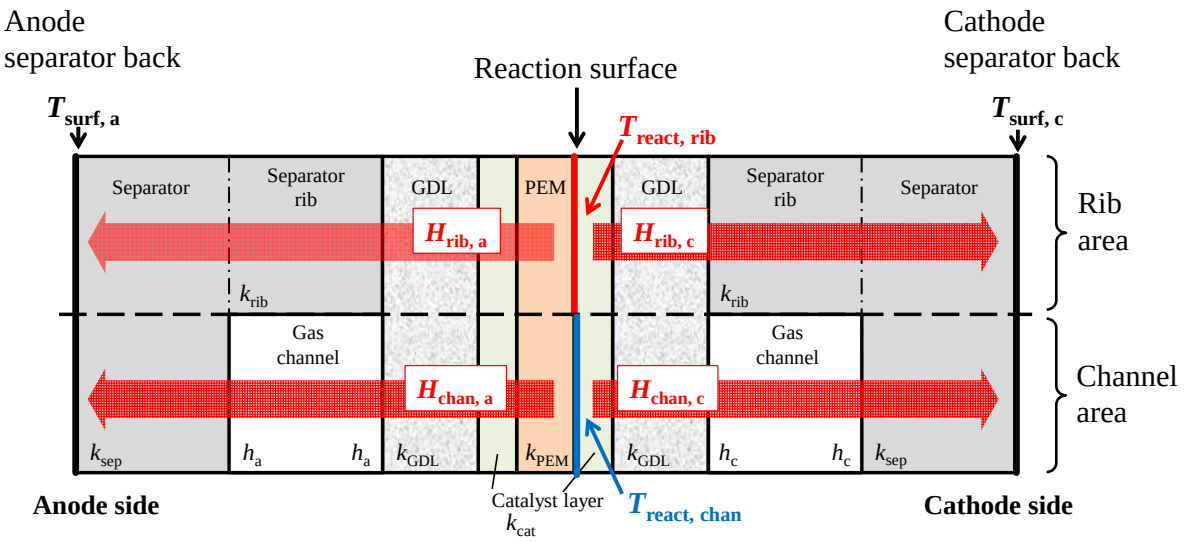

Fig. 1 Multi-plate module.

2.2 Calculation of Heat Generation Rate by Reaction

Heat generation rate H_{react} as a reaction product is calculated as the following:

$$H_{react} = E_i - W_E \quad (1)$$

where, E_i is the ideal (total) energy generation rate by the water formation from H_2 and O_2 based on higher heating value; W_E is the electric work generated by PEFC. E_i and W_E are expressed as follows:

$$E_i = m_{H2} \times q_{HHV} \quad (2)$$

$$W_E = I \times V \quad (3)$$

where, m_{H2} is the molar flow rate of supplied H_2; q_{HHV} is the higher heating value of H_2 (= 285.83×10^3 J·mol^{-1}); I is the load current obtained by the experiment (= 20 A); V is the voltage obtained by the experiment. m_{H2} is equal to the ideal reaction consumption rate of H_2 required for the generation at 20 A, i.e., the stoichiometric ratio of 1.0. The flow rate of the supply gas (H_2) at the stoichiometric ratio of 1.0 is defined from Eq. (4):

$$m_{H2} = I/nF \quad (4)$$

where, n is the valence of ion (= 2 for H_2); F is the Faraday constant (= 96,500 C·mol^{-1}). m_{O2} which is the molar flow rate of supplied O_2 is calculated by Eq. (5):

$$H_2 + 1/2O_2 = H_2O \quad (5)$$

The actual stoichiometric ratio of supply gas was confirmed, using the mass flow controller installed at the inlet of the single cell and the mass flow mater installed at the outlet of the cell in the power-generation experiment [10].

2.3 Heat-Balance Equations for Calculating Temperature of Reaction Surface

The heats transferred in the model proposed are expressed as Eqs. (6)-(10):

$$H_{rib, c} = K_{rib, c}A(T_{react, rib} - T_{surf, c})/2 \quad (6)$$

$$H_{chan, c} = K_{chan, c}A(T_{react, chan} - T_{surf, c})/2 \quad (7)$$

$$H_{rib, a} = K_{rib, a}A(T_{react, rib} - T_{surf, a})/2 \quad (8)$$

$$H_{chan, a} = K_{chan, a}A(T_{react, chan} - T_{surf, a})/2 \quad (9)$$

$$H_{react} = H_{rib, c} + H_{chan, c} + H_{rib, a} + H_{chan, a} \quad (10)$$

where, $H_{rib, c}$ is the heat flux to cathode side under rib; $K_{rib, c}$ is the overall heat-transfer coefficient for cathode side under rib; A is the heat-transfer area which is the active area of MEA, i.e., power-generation area (= 0.0025 m^2); $T_{react, rib}$ is the reaction surface temperature under rib; $T_{surf, c}$ is the cathode separator back temperature; $H_{chan, c}$ is the heat flux to cathode side under channel; $K_{chan, c}$ is the overall heat-transfer coefficient for cathode side under channel; $T_{react, chan}$ is the reaction surface temperature under channel; $H_{rib, a}$ is the heat flux to anode side under rib; $K_{rib, a}$ is the overall heat-transfer coefficient

for anode side under rib; $T_{surf,\,a}$ is the anode separator back temperature; $H_{chan,\,a}$ is the heat flux to anode side under channel; $K_{chan,\,a}$ is the overall heat-transfer coefficient for anode side under channel. $K_{rib,\,c}$, $K_{chan,\,c}$, $K_{rib,\,a}$ and $K_{chan,\,a}$ are defined as follows:

$$1/K_{rib,\,c} = \delta_{cat}/k_{cat} + \delta_{GDL}/k_{GDL} + \delta_{rib}/k_{rib} + \delta_{sep}/k_{sep} \quad (11)$$

$$1/K_{chan,\,c} = \delta_{cat}/k_{cat} + \delta_{GDL}/k_{GDL} + 2/h_c + \delta_{sep}/k_{sep} \quad (12)$$

$$1/K_{rib,\,a} = \delta_{PEM}/k_{PEM} + \delta_{cat}/k_{cat} + \delta_{GDL}/k_{GDL} + \delta_{rib}/k_{rib} + \delta_{sep}/k_{sep} \quad (13)$$

$$1/K_{chan,\,a} = \delta_{PEM}/k_{PEM} + \delta_{cat}/k_{cat} + \delta_{GDL}/k_{GDL} + 2/h_a + \delta_{sep}/k_{sep} \quad (14)$$

where, δ_{cat} is the thickness of the catalyst layer; k_{cat} is the thermal conductivity of the catalyst layer; δ_{GDL} is the thickness of GDL; k_{GDL} is the thermal conductivity of GDL; δ_{rib} is the thickness of the separator rib; k_{rib} is the thermal conductivity of the separator rib; δ_{sep} is the thickness of the separator excluding rib part; k_{sep} is the thermal conductivity of the separator excluding rib part; h_c is the convection heat-transfer coefficient for cathode side; δ_{PEM} is the thickness of PEM; k_{PEM} is the thermal conductivity of PEM; h_a is the convection heat-transfer coefficient for anode side.

Table 1 lists the specification of cell components used in the model. The materials of PEM, catalyst layer, GDL and separator are Nafion 115, compound of platinum and carbon, carbon paper and carbon graphite, respectively. The thickness values listed here are the same as those of the components used by previous studies [10, 16, 17].

In Table 1, the effective thermal conductivities of porous media (k), are the values of the cell components used in the present experiment and in Refs. [10, 13]. Because the effective thermal conductivities given in Table 1 are obtained when the cell component pores are filled with air at room temperature, the corrected effective thermal conductivities are calculated for the cell component pores filled with H_2, or O_2 at 70 °C or 80 °C. Tables 2 and 3 list the corrected effective thermal conductivities of each cell component at 70 °C and 80 °C, respectively. In this calculation, the thermal conductivities of each gas are from the Japan Society of Mechanical Engineers [18].

The convective heat-transfer coefficient h between the gas flows in the gas channel and GDL or separator wall is obtained from the study on heat-transfer in rectangular micro-channels [19]. The mass flow rates of the consumed gas and generated water in the gas channel, and the physical properties of the mixture gas were used for calculating the *Re* and h. The relationship among the Nu, aspect ratio of gas channel and Knudsen number for some *Re* values has been reported [19]. Although the *Re* is changed along the gas channel from the inlet to the outlet as well as with operation conditions, the *Re* was assumed to be 10 under all operation conditions investigated in this study. The Nu was also assumed to be a constant due to the similarity of gas flow under the operation conditions investigated. The Nu was taken as 3.0 in the present study [19]. Convective heat-transfer coefficient h is then calculated by Eq. (15):

$$h = \mathrm{Nu}k_{chan}/D_h \quad (15)$$

where, k_{chan} is the effective thermal conductivity of

Table 1 Specification of cell components.

Parts	Size	Characteristics	Porosity	Effective thermal conductivity ($W \cdot m^{-1} \cdot K^{-1}$)
PEM	50.0 mm × 50.0 mm × 0.13 mm	Nafion 115 (produced by Du Pont Corp.)	0.15	0.195
Catalyst layer	50.0 mm × 50.0 mm × 0.01 mm (attached with PEM)	Pt/C (20 wt.% Pt loading)	0.78	0.27
GDL	50.0 mm × 50.0 mm × 0.17 mm	Carbon paper (TGP-H-060 produced by Toray Corp.)	0.78	1.7
Separator	75.4 mm × 75.4 mm × 2.00 mm (thickness of rib part: 1.00 mm) (gas supply area: 50.0 mm × 50.0 mm)	Carbon graphite, serpentine	0.28	25

Table 2 Corrected effective thermal conductivity of each cell component at 70 °C.

Component	Effective thermal conductivity ($W \cdot m^{-1} \cdot K^{-1}$)	
	Anode (H_2)	Cathode (O_2)
PEM	0.26	-
Catalyst layer	0.42	0.27
GDL	1.9	1.7
Separator	25	25

Table 3 Corrected effective thermal conductivity of each cell component at 80 °C.

Component	Effective thermal conductivity ($W \cdot m^{-1} \cdot K^{-1}$)	
	Anode (H_2)	Cathode (O_2)
PEM	0.26	-
Catalyst layer	0.43	0.27
GDL	1.9	1.7
Separator	25	25

mixture gas in channel; D_h is the hydraulic diameter of channel. In this study, the separator whose gas channel width and depth are 1.0 mm adopted, resulting that D_h is 1.0 mm.

To solve Eqs. (6)-(9), the temperatures measured using the thermograph were substituted into these equations as $T_{surf,\ c}$ and $T_{surf,\ a}$. The operation conditions used for power-generation in order to measure temperatures with thermograph are given in Table 4. Analysis using 1D multi-plate heat-transfer model as well as 3D numerical simulation model is carried out by means of the data obtained under these conditions. The experimental procedure for measuring temperature during power-generation has been explained in Ref. [10].

In order to use the temperature data measured by thermograph in 1D multi-plate heat-transfer model, the image of in-plane temperature distribution is divided into segments of 10 mm × 10 mm each, as shown in Fig. 2. Although the power-generation area is 50 mm × 50 mm, the observation area is set to be 40 mm × 50 mm to prevent gas leak through observation window in experiment. Space resolution and temperature resolution of the measurement by thermograph were 1.2 mm and 0.1 °C, respectively. The gas channel width and the rib width of

Table 4 Operation conditions of power-generation for temperature measurement by thermograph.

Initial temperature of cell (°C)	70, 80	
Load current of cell (A) (Current density of cell (A/cm^2))	20 (0.80)	
Supply gas condition		
	Anode	Cathode
Temperature of supply gas at inlet (°C)	70, 80	70, 80
Relative humidity of supply gas (% RH (relative humidity))	40, 80	40, 80
Pressure of supply gas at inlet (absolute) (MPa)	0.4	0.4
Flow rate of supply gas at inlet (NL/min) (stoichiometric ratio)	0.210 (1.5) 0.280 (2.0) 0.420 (3.0)	0.105 (1.5) 0.140 (2.0) 0.210 (3.0)

investigated separator are 1.0 mm and the number of gas channel is 5. The segment includes the area consisting of five pairs of rib and gas channel. The average temperature in each segment at anode and cathode was used for the separator's back temperature in 1D multi-plate heat-transfer model. The segment is named A to T along the gas-flow direction as shown in Fig. 2. Regarding segments A and T, the insulators covering the gas pipes interfere with the thermograph measurement in some area of the segment as it can be seen in Fig. 2. In this study, the effective temperature of segments A and T were obtained by removing the temperature data that were interfered by the insulator from the total temperature data in each segment. In the heat-transfer analysis, it was assumed that, $T_{surf,\ c}$ on the rib side was equal to $T_{surf,\ c}$ on the channel side as well as $T_{surf,\ a}$ because the difference between them could not be recognized by the measured data.

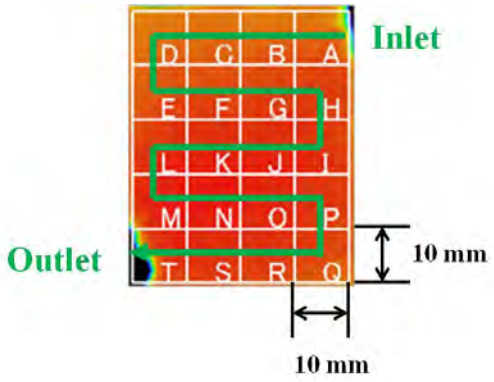

Fig. 2 Segment display of in-plane temperature distribution measured by thermograph.

By the comparison of temperature distribution between in-plane and through-plane, the difference between $T_{\text{react, rib}}$ and $T_{\text{react, chan}}$ was found to be small, i.e., less than 1 °C [14, 15, 20], while the temperature difference between the reaction surface and separator's back was approximately 1-8 °C in the present study. Consequently, it is believed that, the heat flow in the through-plane direction dominates the heat-transfer in the cell.

Considering the above-described assumptions and Eqs. (6)-(14), the reaction surface temperature T_{react} is expressed as follows:

$$T_{\text{react}} = T_{\text{react, rib}} = T_{\text{react, chan}} = \{2H_{\text{react}}/A + (K_{\text{rib, c}} + K_{\text{chan, c}})/T_{\text{surf, c}} + (K_{\text{rib, a}} + K_{\text{chan, a}})T_{\text{surf, a}}\}/(K_{\text{rib, c}} + K_{\text{chan, c}} + K_{\text{rib, a}} + K_{\text{chan, a}}) \quad (16)$$

2.4 3D Numerical Simulation Model and Calculation Conditions

To verify the temperature distribution on the reaction surface calculated by 1D multi-plate heat-transfer model, the numerical simulation using 3D model was conducted by CFD-ACE+. This CFD software has the simulation code for PEFC composed of the equations such as conservation equations of mass, momentum and energy in porous region as well as electrochemical reaction explained by the previous research in detail [21]. Although the detailed explanation for all equations concedes Ref. [21], the conservation equation for energy is written as [22, 23]:

$$\partial\left\{(1-\varepsilon)\rho_s h_s + \varepsilon\rho h\right\}/\partial t + \nabla\cdot(\varepsilon\rho U h) = \nabla\cdot q + \varepsilon\tau\nabla U + \varepsilon(\mathrm{d}p/\mathrm{d}t) - I_T\eta + |i\cdot i|/\sigma + \dot{S}_h \quad (17)$$

where, ε is porosity; ρ_s is mass density of solid; h_s is enthalpy of solid; ρ is mass density of mixture; h is enthalpy of mixture; t is lapse time; U is fluid velocity vector; q is heat flux; τ is shear stress tensor; p is absolute pressure; I_T is net transfer current due to electrochemical reaction; η is electrode overpotential; i is net current density; σ is electrical conductivity; $\dot{S}_h$ is enthalpy source due to phase change. The heat flux q is comprised of thermal conduction and species diffusion, and is written as [24]:

$$q = \lambda\nabla T + \sum_{i=1}^{N_G} J_i h_i \quad (18)$$

where, λ is effective thermal conductivity; T is bulk temperature; N_G is total number of gas species; J_i is diffusion flux of i-th species; h_i is enthalpy of i-th species. The effective thermal conductivity of the fluid and solid region is written as [25]:

$$\lambda = -2\lambda_S + 1/\left\{\varepsilon/(2\lambda_S + \lambda_F) + (1-\varepsilon)/3\lambda_S\right\} \quad (19)$$

where, λ_S is thermal conductivity of solid in porous region; λ_F is thermal conductivity of fluid (or pore) in porous region. Consideration on conservation of enthalpy, heat derived from shear stress and pressure drop of fluid flow, and heat derived from current transfer is the different point in 3D numerical simulation model compared to the 1D multi-plate heat-transfer model.

To solve the conservation equation was performed by using a finite volume scheme on arbitrary mesh topology within the framework of the commercial CFD code CFD-ACE+. The governing equations are derived on the basis of the following assumptions [26, 27]:

(1) The volume of condensed water is ignored and the water moves with gas;

(2) The reduction of the reaction area caused by flooding in electrode is ignored and diffusion prevention caused by water condensation is ignored;

(3) Cell voltage is uniform and constant;

(4) The effective porosity and the permeability of porous media are isotropic;

(5) Heat-transfer between gas and solid phase of porous media is ignored;

(6) Fluid is incompressible Newtonian fluid and ideal gas. Flow condition is a laminar flow;

(7) The distribution of inlet gas flow rate at each side is uniform;

(8) In PEM, ionic conductivity, electro-osmosis coefficient, and water effective diffusion coefficient that depend on humidity are disregarded;

(9) The gas cross over through PEM is disregarded.

The validation of simulation procedure using these equations has been already proved well [26-30].

Fig. 3 and Table 5 show the simulation model and the calculation conditions other than the conditions shown earlier in Table 4, respectively.

As shown in Fig. 3, the model width corresponds to a pair of gas channel and rib, which is the length from the rib center to the next rib center. The structure was assumed to be symmetric about the rib in order to clarify two questions regarding the temperature gradients: (1) How large the through-plane (Y axis direction in Fig. 3) temperature difference between the reaction surface and separator's back at cathode is? (2) How large the in-plane (Z axis direction in Fig. 3) temperature distribution between the gas channel center and the rib center on the reaction surface is? By the 3D numerical simulation, the temperature difference between reaction surface and separator's back was clarified, resulting that the heat-transfer in Y axis direction was investigated. In addition, the temperature distribution in Z axis direction on the reaction surface was also investigated by the 3D numerical simulation. The 1D multi-plate heat-transfer model was verified by the 3D model through these investigations. The thicknesses of cell components are given in Table 1. The temperature data measured by thermograph during power-generation experiment were used as the boundary condition for the separator's back temperature at anode and cathode. This boundary condition was the same as the one used in 1D multi-plate heat-transfer model. As shown in Fig. 3, the counter flow was simulated for gas flow in gas channel of separator, which was followed by the power-generation experiment in the previous study [10].

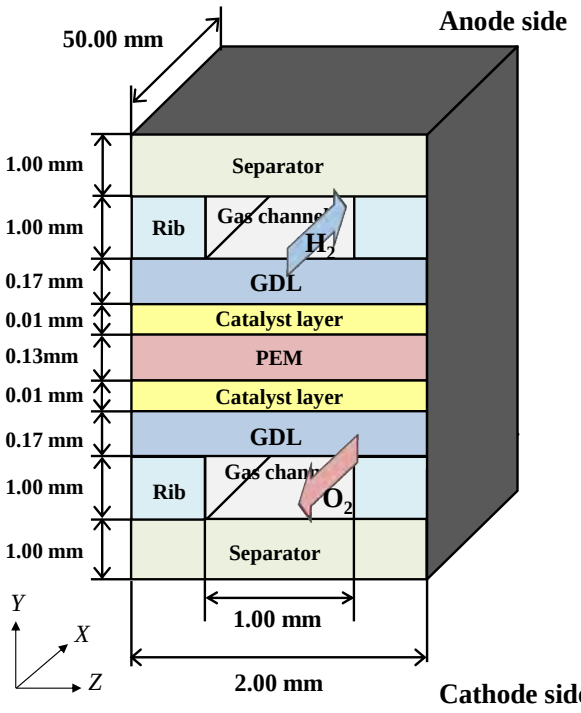

Fig. 3 3D model for numerical simulation by CFD-ACE+.

Table 5 Calculation conditions (A: for porous media; B: for solid media).

A

	GDL	Catalyst layer	PEM
Porosity	0.78	0.78	0.28
Permeability (through-plane) (m^2)	8.69×10^{-12}	8.69×10^{-12}	1.0×10^{-18}
Permeability (in-plane) (m^2)	1.6×10^{-11}	1.6×10^{-11}	
Mean particle size (m)	1.0×10^{-6}	1.0×10^{-6}	1.0×10^{-6}
Effective catalyst area ($1 \cdot m^{-1}$)	-	1,000	-
Thermal conductivity (through-plane) ($W \cdot m^{-1} \cdot K^{-1}$)	1.7	0.27	0.195
Thermal conductivity (in-plane) ($W \cdot m^{-1} \cdot K^{-1}$)	22		
Electric conductivity (isotropy) ($1 \cdot ohm^{-1} \cdot m^{-1}$)	53	53	1.0×10^{-20}

B

	Separator
Density ($kg \cdot m^{-3}$)	1,720
Electric conductivity ($1 \cdot ohm^{-1} \cdot m^{-1}$)	8.3×10^4
Specific heat ($J \cdot kg^{-1} \cdot K^{-1}$)	810
Thermal conductivity ($W \cdot m^{-1} \cdot K^{-1}$)	25

The gas channel length (to X axis direction in Fig. 3) was set at 50 mm which was equal to the one straight path length of the actual separator used for power-generation experiment [10]. Though this length is short compared to the actual total length of separator from the inlet to the outlet, this model assumes the part near the inlet. If wider mass and temperature distributions were occurred near the inlet under the simulation conditions, it would be thought that, the factor causing the distribution influences more strongly for the whole cell. In addition, the main purpose of this study is to verify the temperature distribution on the reaction surface calculated by 1D multi-plate heat-transfer model. Since the initial conditions such as flow rate and temperature of supply gas can be set at the same values accurately for both 1D multi-plate heat-transfer model and 3D numerical simulation model, this 3D model meets the purpose of this study as the first step. It is planned the study will be extended to cover the computational domain to X axis direction as well in the near future.

To investigate the impact of operation condition on mass and temperature distributions, T_{ini}, flow rate and relative humidity of supply gas were varied. Furthermore, the temperature distribution on the reaction surface calculated by the numerical simulation using 3D model was compared to that calculated by 1D multi-plate heat-transfer model as well as the results reported by the previous studies.

3. Results and Discussion

3.1 Temperature Distribution Calculated by 1D Multi-plate Heat-Transfer Model

Fig. 4 shows the effect of T_{ini} on temperature distribution on reaction surface calculated by 1D multi-plate heat-transfer model in each segment in cell at T_{ini} of 70 °C and 80 °C, respectively. The stoichiometric ratio of supply gases are 1.5, 2.0 and 3.0. The relative humidity of supply gas is 80% RH.

It can be seen from Fig. 4 that, the reaction surface temperature rise from T_{ini}, i.e., $T_{react} - T_{ini}$, at T_{ini} of 70 °C is higher than that at T_{ini} of 80 °C irrespective of flow rate of supply gas. The reason was thought to be that O_2 was used as the cathode gas and was sufficient even if the stoichiometric ratio of the supply gas was 1.5.

According to the voltages obtained by power-generation experiments as listed in Table 6, the voltages at T_{ini} of 70 °C are lower than those at T_{ini} of 80 °C irrespective of flow rate of supply gas. At

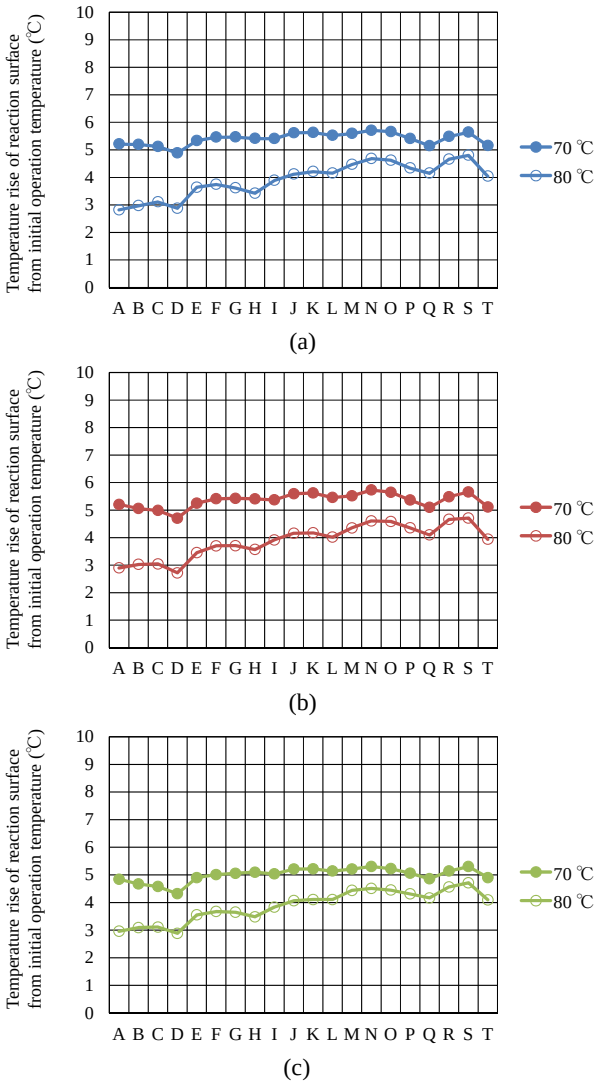

Fig. 4 Effect of initial operation temperature on temperature distribution on reaction surface calculated by 1D multi-plate heat-transfer model: (a) stoichiometric ratio of 1.5; (b) stoichiometric ratio of 2.0; (c) stoichiometric ratio of 3.0.

Table 6 Comparison of voltage obtained by power-generation experiment among different operation conditions.

Initial operation temperature (°C)		70	80
Relative humidity of supply gas (% RH)	80	40	80
Flow rate of supply gas			
Stoichiometric ratio: 1.5	0.52 V	0.40 V	0.54 V
Stoichiometric ratio: 2.0	0.52 V	0.37 V	0.53 V
Stoichiometric ratio: 3.0	0.52 V	0.34 V	0.53 V

higher T_{ini}, the kinetics for both electrode reactions are enhanced [31]. Therefore, it is thought that, the power-generation performance of PEFC is promoted at higher T_{ini}. When the W_E at T_{ini} of 70 °C is lower than that at T_{ini} of 80 °C, H_{react} at T_{ini} of 70 °C is higher than that at T_{ini} of 80 °C as derived from Eqs. (1) and (3). Consequently, T_{react} at T_{ini} of 70 °C is higher than that at T_{ini} of 80 °C.

In addition, it can be seen from Fig. 4 that $T_{react} - T_{ini}$ drops in the segments of D, H, Q and T. This is because, water droplets are easy to resident at the turn-round parts of gas channel and the outlet in the case of serpentine gas channel [32-34] used in the present experiment and the previous study [10]. The gas diffusion toward catalyst layer is disturbed in these segments, resulting that the electrochemical reaction is not carried out well. Thus, T_{react} drops in these segments. Therefore, it is important to remove the water from the turn-round parts of gas channel in order to achieve the even in-plane temperature distribution on reaction surface.

Fig. 5 shows the effect of relative humidity of supply gas on temperature distribution on reaction surface calculated by 1D multi-plate heat-transfer model, when the stoichiometric ratio of supply gases are 1.5, 2.0 and 3.0. T_{ini} is 70 °C.

It can be seen from Fig. 5 that, the $T_{react} - T_{ini}$ for 40% RH is higher than that for 80% RH irrespective of flow rate of supply gas. According to the experimental results, the voltage generated with 40% RH is smaller than that with 80% RH as shown in Table 6. Since the PEM conductivity decreases with decrease in water content in PEM [35], the membrane resistance increases. Therefore, the voltage drops with decrease in the relative humidity of supply gas. As derived from Eqs. (1) and (3), H_{react} for 40% RH is higher than that for 80% RH. Consequently, T_{react} for 40% RH is higher than that for 80% RH.

In addition, it is known from Fig. 5 that, the increase in $T_{react} - T_{ini}$ along gas flow direction for 40% RH is larger compared to that for 80% RH. When the relative humidity of supply gas is 80% RH, the electrochemical reaction is conducted well from the inlet of cell throughout the cell due to the sufficient humidification of PEM. The water produced by electrochemical reaction is accumulated along the gas flow direction through gas channel, resulting that

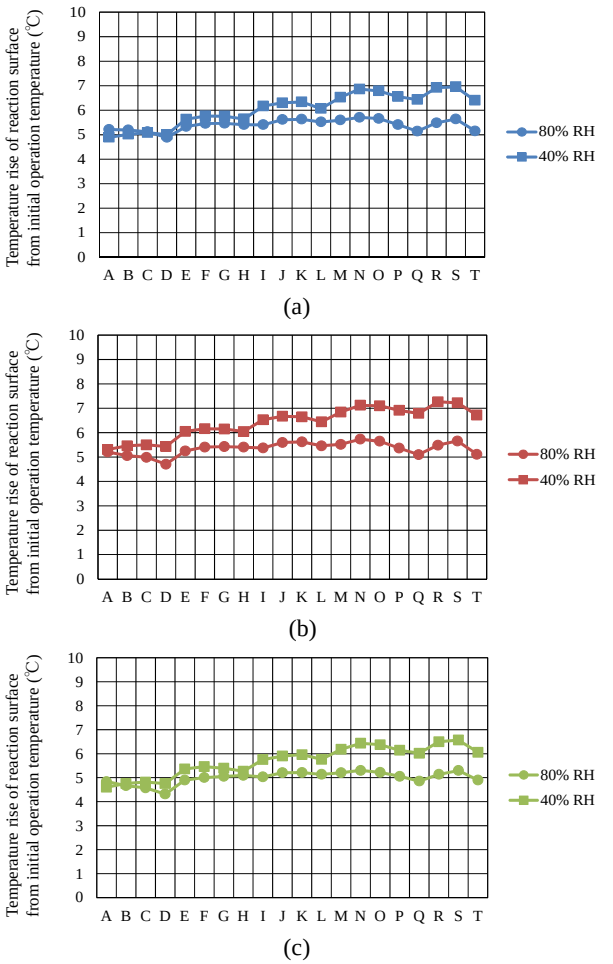

Fig. 5 Effect of relative humidity of supply gas on temperature distribution on reaction surface calculated by 1D multi-plate heat-transfer model: (a) stoichiometric ratio of 1.5; (b) stoichiometric ratio of 2.0; (c) stoichiometric ratio of 3.0.

the gas diffusion inhibition by accumulated water might be occurred toward the outlet of cell. Therefore, the $T_{react} - T_{ini}$ near the outlet does not increase so much. On the other hand, when the relative humidity of supply gas is 40% RH, the humidification of PEM is not good especially near the inlet of cell. However, the water produced by electrochemical reaction humidifies PEM gradually from the segments A to T without gas diffusion inhibition since the excess water does not exist. Therefore, the electrochemical reaction is conducted well through gas channel, resulting in the increase in $T_{react} - T_{ini}$ along gas flow direction. However, the total power-generation performance with 40% RH is worse than that with 80% RH due to the larger membrane resistance even if the electrochemical reaction is conducted better for 40% RH along the gas flow direction in the gas channel.

The total power-generation performance with 80% RH is better than that with 40% RH according to Table 6 and the in-plane temperature distribution for 80% RH is more even than that for 40% RH according to Fig. 5. It can then conclude that, the higher power-generation performance is obtained under the condition leading even in-plane temperature distribution on the reaction surface.

3.2 Mass and Temperature Distribution Calculated by Numerical Simulation Using 3D Model

The characteristics of in-plane mass and temperature distributions in Z axis direction are found to be similar among the investigated conditions. The results obtained under the condition that T_{ini} is 70 °C and the relative humidity of supply gas is 80% RH are shown below.

Fig. 6 shows the molar concentration distribution of H_2 in Z axis direction on the interface between PEM and catalyst layer at anode where the anode electrochemical reaction occurs. Since the molar concentration distribution of H_2 in Z axis direction does not change along the gas channel in X axis direction, the molar concentration distribution of H_2 at

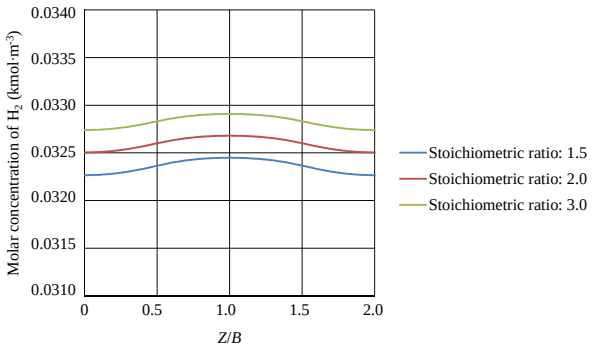

Fig. 6 Molar concentration distribution of H_2 on interface between PEM and catalyst layer at anode calculated by numerical simulation using 3D model (T_{ini}: 70 °C; relative humidity of supply gas: 80% RH).

X = 25 mm which is the gas channel center in X axis direction is given in Fig. 6. In Fig. 6, *B* means the gas channel pitch of separator, which is 1.0 mm. The range from *Z*/*B* = 0.5-1.5 indicates the interface between PEM and catalyst layer at anode under the gas channel, while the range from *Z*/*B* = 0-0.5 and that from *Z*/*B* = 1.5-2.0 indicate the interface between PEM and catalyst layer at anode under the rib.

From Fig. 6, it is clear that, the molar concentration of H_2 under the gas channel is higher than that under the rib. In addition, the highest and the lowest peaks of molar concentration of H_2 are observed at the gas channel center and the rib center, respectively. The gas passing through gas channel diffuses toward through-plane direction and in-plane direction in cell via GDL to catalyst layer. Since there is a large molar concentration difference of H_2 between the gas channel and the rib at the interface between separator and GDL, the molar concentration of H_2 under the gas channel is higher than that under the rib on the interface between PEM and catalyst layer at anode. Furthermore, it is seen that, the amount of molar concentration of H_2 increases with increase in flow rate of supply gas. Since the amount of gas in gas channel increases and the gas diffusion rate is enhanced with increase in flow rate of supply gas, the amount of molar concentration of H_2 on the interface between PEM and catalyst layer at anode increases.

Fig. 7 shows the molar concentration distribution of O_2 in Z axis direction on the reaction surface where the cathode electrochemical reaction occurs. Since the molar concentration distribution of O_2 in Z axis direction does not change along the gas channel in X axis direction, the molar concentration distribution of O_2 at X = 25 mm is given in Fig. 7.

From Fig. 7, it is clear that, the molar concentration of O_2 under the gas channel is higher than that under the rib. In addition, the highest and the lowest peaks of molar concentration of O_2 are observed at the gas channel center and the rib center, respectively. As same as the discussion for Fig. 6, there is a large molar concentration difference of O_2 between the gas channel and the rib at the interface between separator and GDL, the molar concentration of O_2 under the gas channel is higher than that under the rib on the reaction surface. Moreover, it is seen that, the amount of molar concentration of O_2 increases with increase in flow rate of supply gas. As same as the discussion for Fig. 6, the amount of molar concentration of O_2 on the reaction surface increases since the amount of gas in gas channel increases and the gas diffusion rate is enhanced with increase in flow rate of supply gas.

Fig. 8 shows the molar concentration distribution of water in Z axis direction on the reaction surface where the cathode electrochemical reaction occurs. Since the molar concentration distribution of water in Z axis direction does not change along the gas channel in X axis direction, the molar concentration distribution of water at X = 25 mm is given in Fig. 8.

From Fig. 8, it is clear that, the molar concentration of water under the rib is higher than that under the gas channel. In addition, the highest and the lowest peaks of molar concentration of water are observed at the rib center and the gas channel center, respectively. These tendencies are opposed to the molar concentration distribution of O_2 as well as that of H_2. It is thought that, the water under the gas channel is easy to be discharged by O_2 passing toward the outlet of cell. Therefore, the molar concentration of water on the

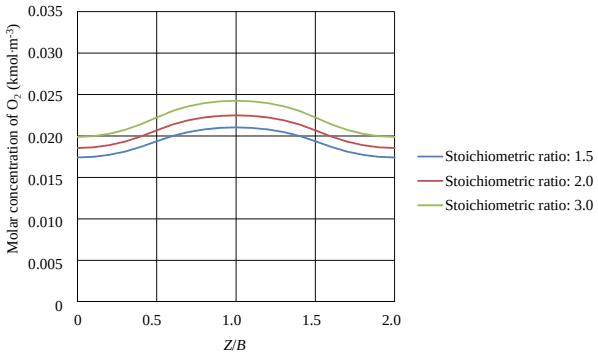

Fig. 7 Molar concentration distribution of O_2 on reaction surface calculated by numerical simulation using 3D model (T_{ini}: 70 °C; relative humidity of supply gas: 80% RH).

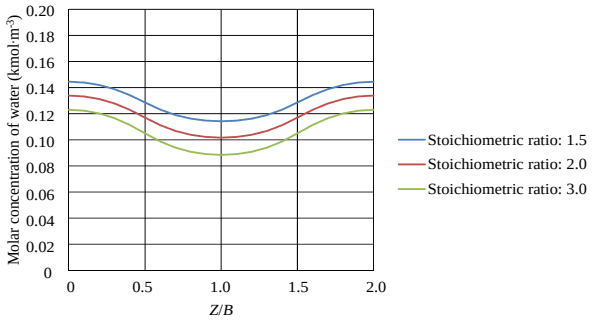

Fig. 8 Molar concentration distribution of water on reaction surface calculated by numerical simulation using 3D model (T_{ini}: 70 °C; relative humidity of supply gas: 80% RH).

reaction surface under the gas channel is lower compared to that under the rib. Furthermore, the amount of molar concentration of water decreases with increase in flow rate of supply gas. As described above, since the water under gas channel is discharged by O_2 passing toward the outlet, the amount of discharged water is larger with increase in flow rate of supply gas. Consequently, the amount of molar concentration of water on the reaction surface decreases with increase in flow rate of supply gas.

Fig. 9 shows the temperature distribution on reaction surface in Z axis direction which is evaluated by $T_{react} - T_{ini}$. Since the T_{react} distribution in Z axis direction does not change along the gas channel in X axis direction, the temperature distribution at X = 25 mm is given in Fig. 9.

From Fig. 9, it is clear that, the $T_{react} - T_{ini}$ under the rib is higher than that under the gas channel. In

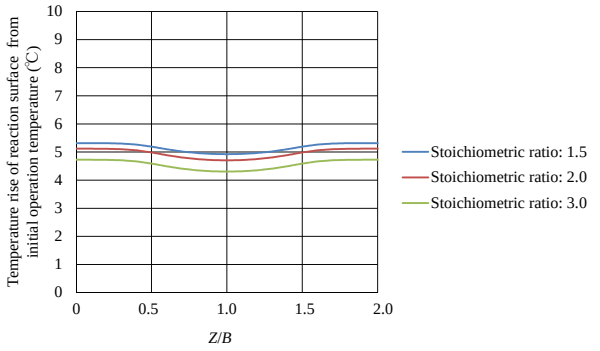

Fig. 9 Temperature distribution on reaction surface calculated by numerical simulation using 3D model (T_{ini}: 70 °C; relative humidity of supply gas: 80% RH).

addition, the highest and the lowest peaks of $T_{react} - T_{ini}$ are observed at the rib center and the gas channel center, respectively. Since the amount of O_2 under the gas channel is larger compared to that under the rib, it is thought that, the convection heat-transfer by O_2 passing toward the outlet of cell is larger. Therefore, the $T_{react} - T_{ini}$ under the gas channel becomes lower than that under the rib. Moreover, $T_{react} - T_{ini}$ decreases with increase in flow rate of supply gas. The convection heat-transfer by O_2 passing toward the outlet is larger with increase in flow rate of supply gas, resulting in the decrease in $T_{react} - T_{ini}$. Although the temperature difference between $T_{react} - T_{ini}$ under the gas channel and that under the rib as well as mass distributions in Z axis direction are confirmed by the numerical simulation using 3D model, the temperature difference is below 1 °C, which is the similar level to the precious studies [14, 15, 20]. Consequently, it is thought that, the assumption of 1D multi-plate heat-transfer model regarding T_{react}, i.e., $T_{react,\ rib} = T_{react,\ chan}$, shown by Eq. (16) is reasonable.

To investigate the effect of T_{ini} on temperature distribution on reaction surface in Z axis direction which is calculated by the numerical simulation using 3D model, Fig. 10 shows the temperature distributions evaluated by $T_{react} - T_{ini}$ at X = 25 mm at T_{ini} of 70 °C and 80 °C, respectively. The temperature distributions at T_{ini} of 70 °C and 80 °C with the relative humidity of supply gas of 80% RH are compared under the same flow rate of supply gas.

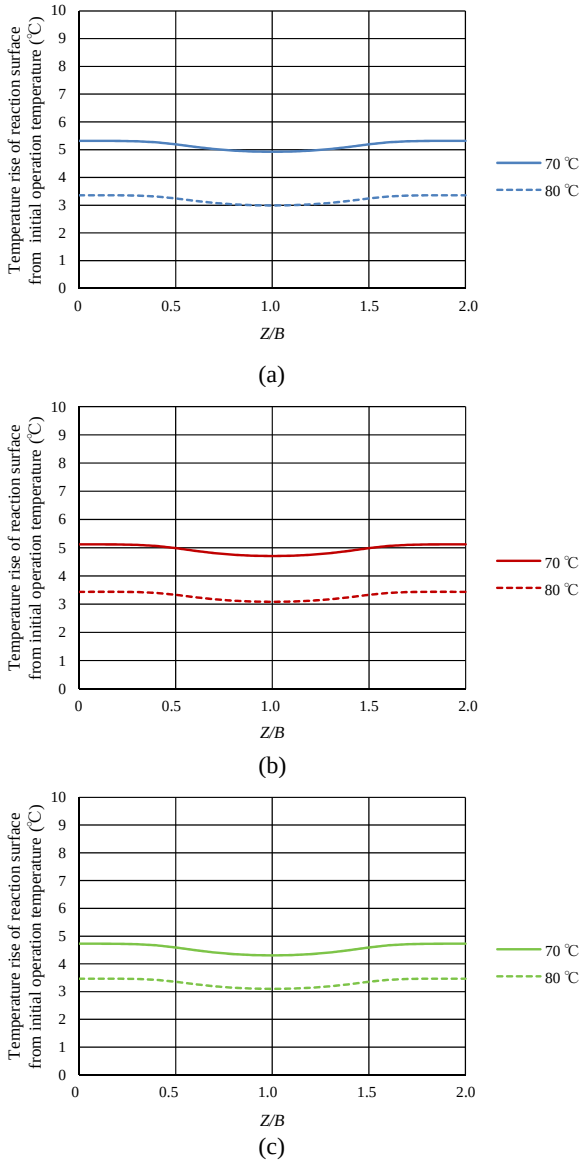

Fig. 10 Effect of initial operation temperature on temperature distribution on reaction surface calculated by numerical simulation using 3D model: (a) stoichiometric ratio of 1.5; (b) stoichiometric ratio of 2.0; (c) stoichiometric ratio of 3.0.

According to Fig. 10, it is known that, the $T_{react} - T_{ini}$ at T_{ini} of 70 °C is higher than that at T_{ini} of 80 °C by approximately 1.5-2.0 °C. Compared to the results obtained by 1D multi-plate heat-transfer model shown in Fig. 4, the temperature difference between T_{ini} of 70 °C and 80 °C in the segments B and C is almost the same, where the position of X = 25 mm corresponds to the interface between the segments B and C. Consequently, the same finding is obtained by both

1D multi-plate heat-transfer model and the numerical simulation using 3D model.

To investigate the effect of relative humidity of supply gas on temperature distribution on reaction surface in Z axis direction which is calculated by the numerical simulation using 3D model, Fig. 11 shows the temperature distributions evaluated by $T_{react} - T_{ini}$ at X = 25 mm at T_{ini} of 70 °C with relative humidity of supply gas of 80% RH and 40% RH, respectively. The

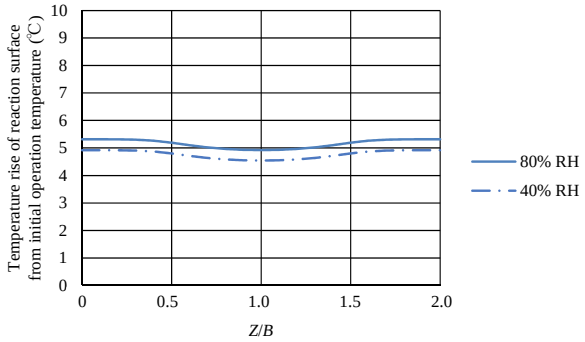

(a)

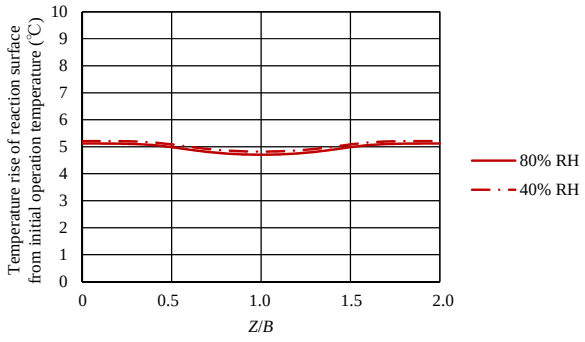

(b)

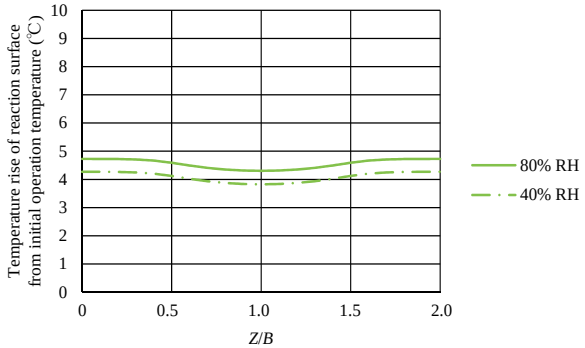

(c)

Fig. 11 Effect of relative humidity of supply gas on temperature distribution on reaction surface calculated by numerical simulation using 3D model: (a) stoichiometric ratio of 1.5; (b) stoichiometric ratio of 2.0; (c) stoichiometric ratio of 3.0.

temperature distributions with 80% RH and 40% RH are compared under the same flow rate of supply gas.

According to Fig. 11, it is known that, the $T_{react} - T_{ini}$ for 40% RH is almost the same as that for 80% RH irrespective of flow rate of supply gas. As shown in Fig. 5, the temperature difference between 40% RH and 80% RH in the segments B and C obtained by 1D multi-plate heat-transfer model is very small. It is believed that, the effect of relative humidity of supply gas on temperature distribution on reaction surface is little, which is led by 1D multi-plate heat-transfer model as well as the numerical simulation using 3D model. Since the impact of water produced by electrochemical reaction on gas diffusion and heat-transfer near the inlet of cell is a little compared to the outlet, the effect of relative humidity of supply gas on temperature distribution on reaction surface calculated by the numerical simulation using 3D model might not be found in this study. As the near future plan, this study will extend the computational domain to X axis direction in order to consider the effect of water accumulation on temperature distribution.

3.3 Comparison of Temperature Distribution on Reaction Surface between the 1D Multi-plate Heat-Transfer Model and the 3D Numerical Simulation Model

Tables 7, 8 and 9 list $T_{react} - T_{ini}$ in the segments A, B, C and D under the condition that T_{ini} is 70 °C and the relative humidity of supply gas is 80% RH, T_{ini} is 80 °C and the relative humidity of supply gas is 80% RH, and T_{ini} is 70 °C and the relative humidity of supply gas is 40% RH, respectively. T_{react} averaged from Z/B = 0 to 2.0 at each center position of X axis direction in the segments A, B, C and D is listed in these tables as the representative temperature obtained by the numerical simulation using 3D model.

According to Tables 7-9, the maximum differences of T_{react} between 1D multi-plate heat-transfer model and 3D numerical simulation model are 0.4 °C (= 8%), 0.3 °C (= 10%) and 0.7 °C (= 17%), respectively.

Table 7 Comparison of temperature distribution on reaction surface between 1D multi-plate heat-transfer model and 3D numerical simulation model (T_{ini}: 70 °C; relative humidity of supply gas: 80% RH).

Initial operation temperature, relative humidity of supply gas	Stoichiometric ratio	Model	Temperature rise of reaction surface from initial operation temperature (°C)			
			Segment A	Segment B	Segment C	Segment D
70 °C, 80% RH	1.5	1D multi-plate heat transfer	5.4	5.3	5.3	5.0
		3D numerical simulation	5.4	5.3	5.3	5.0
	2.0	1D multi-plate heat transfer	5.0	5.1	5.1	4.7
		3D numerical simulation	5.4	5.2	5.1	4.9
	3.0	1D multi-plate heat transfer	4.7	4.7	4.7	4.4
		3D numerical simulation	5.0	4.8	4.7	4.5

Table 8 Comparison of temperature distribution on reaction surface between 1D multi-plate heat-transfer model and 3D numerical simulation model (T_{ini}: 80 °C; relative humidity of supply gas: 80% RH).

Initial operation temperature, relative humidity of supply gas	Stoichiometric ratio	Model	Temperature rise of reaction surface from initial operation temperature (°C)			
			Segment A	Segment B	Segment C	Segment D
80 °C, 80% RH	1.5	1D multi-plate heat transfer	3.2	3.3	3.4	3.0
		3D numerical simulation	3.0	3.1	3.3	3.0
	2.0	1D multi-plate heat transfer	3.3	3.4	3.4	3.0
		3D numerical simulation	3.0	3.2	3.2	2.9
	3.0	1D multi-plate heat transfer	3.3	3.5	3.5	3.2
		3D numerical simulation	3.1	3.2	3.3	3.0

Table 9 Comparison of temperature distribution on reaction surface between 1D multi-plate heat-transfer model and 3D numerical simulation model (T_{ini}: 70 °C; relative humidity of supply gas: 40% RH).

Initial operation temperature, relative humidity of supply gas	Stoichiometric ratio	Model	Temperature of reaction surface from initial operation temperature (°C)			
			Segment A	Segment B	Segment C	Segment D
70 °C, 40% RH	1.5	1D multi-plate heat transfer	4.7	4.9	4.9	4.6
		3D numerical simulation	4.8	5.2	5.2	5.2
	2.0	1D multi-plate heat transfer	4.9	5.2	5.2	4.9
		3D numerical simulation	5.4	5.6	5.7	5.5
	3.0	1D multi-plate heat transfer	4.0	4.2	4.3	4.1
		3D numerical simulation	4.7	4.9	5.0	4.8

Though the 1D multi-plate heat-transfer model proposed by this study treats the heat-transfer phenomena in the cell of PEFC simpler, the model can predict the temperature distribution on the reaction surface on equal terms with the 3D model solving many governing equations on the coupling phenomena in a cell of PEFC.

According to the previous 2D numerical simulation study, considering the heat generation and depletion by reversible/irreversible heat release, ohmic heating and phase change of water [36], $T_{react} - T_{ini}$ ranging from 1 °C to 6 °C was reported under the condition that T_{ini} was 70 °C, the relative humidity of supply gas was 100% RH, and the cell voltage ranged from 0.30 V to 0.70 V. In addition, from the other 3D numerical simulation study accounting for various heat generation mechanisms including irreversible heat due to electrochemical reactions, entropic heat and Joule heating arising from the electrolyte ionic resistance [37], $T_{react} - T_{ini}$ ranging from 2 °C to 11 °C was reported under the condition that T_{ini} was 70 °C, the relative humidity of supply gas at anode was 75% RH, the relative humidity of supply gas at cathode was 0% RH, and the cell voltage was 0.6 V. Moreover, according to the experimental study measuring the PEM temperature by temperature sensor [38], $T_{react} - T_{ini}$

ranging from 2 °C to 3 °C was reported under the condition that T_{ini} was 80 °C, the relative humidity of supply gas was 100% RH, and the cell voltage was 0.2 V. Compared with the above previous studies conducted under the similar operation conditions [36-38], it is obvious that, $T_{react} - T_{ini}$ calculated by the 1D multi-plate heat-transfer model in this study as well as by the 3D model are correct. The temperature gradients from the reaction surface to the separator's back obtained by the 1D multi-plate heat-transfer model range approximately from 1 °C to 8 °C, while those obtained by the previous studies [13-15, 36-38] range approximately from 1 °C to 11 °C. Consequently, the simple 1D multi-plate heat-transfer model proposed by this study is effective for prediction of temperature distribution on the reaction surface.

4. Conclusions

The temperature distribution on the reaction surface calculated by the 1D multi-plate heat-transfer model proposed has been validated by the numerical simulation using a 3D model as well as the previous studies. In addition, the effects of T_{ini}, flow rate and relative humidity of supply gas on the temperature distribution on the reaction surface have been also investigated by the 1D multi-plate heat-transfer model as well as the 3D numerical simulation model. From the investigation of this study, the following conclusions have been obtained:

(1) The $T_{react} - T_{ini}$ at T_{ini} of 70 °C is higher than that at T_{ini} of 80 °C irrespective of flow rate of supply gas. Since the power-generation performance of PEFC is promoted at higher T_{ini}, H_{react} at T_{ini} of 70 °C is higher than that at T_{ini} of 80 °C, which is derived from Eqs. (1) and (3);

(2) The $T_{react} - T_{ini}$ with 40% RH is almost the same as that with 80% RH near the inlet of the cell irrespective of flow rate of supply gas. However, the increase in $T_{react} - T_{ini}$ along gas flow from the segments A to T for 40% RH is larger compared to 80% RH according to the 1D multi-plate heat-transfer model. It is because that, the impact of water produced by electrochemical reaction on gas diffusion and heat-transfer near the inlet of cell is smaller compared to the outlet;

(3) Although the 1D multi-plate heat-transfer model proposed by this study treats the heat-transfer phenomena in the cell of PEFC in a simple way, the model can predict the temperature distribution on the reaction surface on equal terms with the 3D model solving many governing equations on the coupling phenomena in a cell of PEFC;

(4) The $T_{react} - T_{ini}$ calculated by the 1D multi-plate heat-transfer model as well as the numerical simulation using 3D model agrees with that in previous studies conducted under the similar operation conditions;

(5) The simple 1D multi-plate heat-transfer model proposed by this study is effective for prediction of temperature distribution on the reaction surface.

Acknowledgments

This work was supported by Mie prefecture industrial research institute. The authors acknowledge its great contribution.

References

[1] Kubo, N., Fukuyama, Y., Mashio, T., Sakamoto, Y., Kusaka, J., and Daisho, Y. 2004. "Study on Transport Phenomena in Polymer Electrolyte Fuel Cell (First Report)—the Experimental and Numerical Investigation by the Use of Segmented Cell-." *J. Soc. Automot. Eng. Japan Trans.* 35 (4): 65-71.

[2] Weber, A. Z., Darling, R. M., and Newman, J. 2004. "Modeling Two-Phase Behavior in PEFCs." *J. Electrochemical Society* 151 (10): A1715-27.

[3] Wang, M., Guo, H., and Ma, C. 2006. "Temperature Distribution on the MEA Surface of a PEMFC with Serpentine Channel Flow Bed." *J. Power Sources* 157 (1): 181-7.

[4] Ito, K. 2008. "Temperature Distribution Measurement in Through-Plane Direction for PEFC." *Japan Society of Mechanical Engineers* 111 (1079): 42-4.

[5] Tsuji, K. 2008. "Domestic Fuel Cell Co-generation System Entering Real Commercial Stage." *Hydrogen*

Energy System 33 (3): 93-6.

[6] Uchida, H. 2008. "Observation on Polymer Electrolyte Fuel Cell for High Performance and High Durability and Priority Subject on Technology Development in Future." In *Proceedings of the Analysis on Degradation Mechanism of Polymer Electrolyte Fuel Cell, Preprints of the NEDO Symposium*, 35-41.

[7] Zhang, G., Shen, S., Guo, L., and Liu, H. 2012. "Dynamic Characteristics of Local Current Densities and Temperatures in Proton Exchange Membrane Fuel Cells during Reactant Starvations." *Int. J. Hydrogen Energy* 37 (2): 1884-92.

[8] Zhang, G., Guo, L., Ma, L., and Liu, H. 2010. "Simultaneous Measurement of Current and Temperature Distributions in a Proton Exchange Membrane Fuel Cell." *J. Power Sources* 195 (11): 3597-604.

[9] Lee, C. Y., Fan, W. Y., and Chang, C. P. 2011. "A Novel Method for in-situ Monitoring of Local Voltage, Temperature and Humidity Distributions in Fuel Cell Using Flexible Multi-functional Micro Sensors." *Sensors* 11 (2): 1418-32.

[10] Nishimura, A., Shibuya, K., Morimoto, A., Tanaka, S., Hirota, M., Nakamura, Y., Kojima, M., Narita, M., and Hu, E. 2012. "Dominant Factor and Mechanism of Coupling Phenomena in Single Cell of Polymer Electrolyte Fuel Cell." *Applied Energy* 90 (1): 73-9.

[11] Nishimura, A., Iio, K., Baba, M., Yamauchi, T., Hirota, M., and Hu, E. 2014. "Modeling of Heat Transfer in Single Cell of Polymer Electrolyte Fuel Cell by Means of Temperature Data Measured by Thermograph." *J. Chemical Engineering of Japan* 47 (7): 521-9.

[12] Nishimura, A., Fukuoka, T., Baba, M., Hirota, M., and Hu, E. "Clarification on Temperature Distribution in Single Cell of Polymer Electrolyte Fuel Cell under Different Operation Conditions by Means of 1D Multi-plate Heat-Transfer Model." *J. Chemical Engineering of Japan* (in press).

[13] Khandelwal, M., and Mench, M. M. 2006. "Direct Measurement of Through-Plane Thermal Conductivity and Contact Resistance in Fuel Cell Materials." *J. Power Sources* 161 (2): 1106-15.

[14] Kawase, M., Inagaki, T., Kawashima, S., and Miura, K. 2009. "Effective Thermal Conductivity of Gas Diffusion Layer in Through-Plane Direction." *ECS Trans.* 25 (1): 1529-37.

[15] Jung, C. Y., Shim, H. S., Koo, S. M., Lee, S. H., and Yi, S. C. 2012. "Investigation of the Temperature Distribution in Proton Exchange Membrane Fuel Cell." *Applied Energy* 93 (May): 733-41.

[16] Hwang, S. S., Han, S. S., Lee, P. H., and Park, B. I. 2010. "Transient Performance Behavior of Proton Exchange Membrane Fuel Cell by Configuration of Membrane and Gas Diffusion Layer." *J. Thermal Science and Technology* 5 (1): 165-77.

[17] Wu, H., Berg, P., and Li, X. 2010. "Steady and Unsteady 3D Non-isothermal Modeling of PEM Fuel Cells with the Effect of Non-equilibrium Phase Transfer." *Applied Energy* 87 (9): 2778-84.

[18] The Japan Society of Mechanical Engineers. 1993. "JSME Heat Transfer Handbook." The Japan Society of Mechanical Engineers.

[19] Renksizbulut, M., Niazmand, H., and Tercan, G. 2006. "Slip-Flow and Heat Transfer in Rectangular Microchannels with Constant Wall Temperature." *International J. Thermal Science* 45 (9): 870-81.

[20] Oshima, A., Nishimura, A., Morimoto, A., Tanaka, S., Hirota, M., and Narita, M. 2010. "Theoretical Investigation on Influence of Inflow Gas Condition and Gas Channel Structure of Separator on Mass and Temperature Distribution in Single Cell of Polymer Electrolyte Fuel Cell." In *Proceedings of the Mechanical Engineering Congress*, 203-4.

[21] Nishimura, A., Morimoto, A., Tanaka, S., Oshima, A., Hirota, M., Tohma, E., Kimura, Y., and Narita, M. 2012. "Influence of Cell Components Structure on Heat and Mass Transfer Phenomena in Single-Cell PEFC." *J. Energy and Power Engineering* 6 (4): 504-18.

[22] Bird, R. B., Stewart, W. E., and Lightfoot, E. N. 1960. *Transport Phenomena.* Tokyo: Toppan Company Ltd., 81-2.

[23] Kaviany, M. 1999. *Principles of Heat Transfer in Porous Media.* New York: Springer, 145-8, 166-72.

[24] Gurau, V., Liu, H., and Kakac, S. 1998. Two-Dimensional Model for Proton Exchange Membrane Fuel Cells." *AIChE J.* 44 (11): 2410-22.

[25] Dagan, G. 1989. *Flow and Transport in Porous Formations.* Berlin: Splinger-Verlag Berlin Heidelberg, 55-61, 82-3, 89-91.

[26] Mazumdar, S., and Cole, J. V. 2003. "Rigorous 3-D Mathematical Modeling of PEM Fuel Cells, I. Model Predictions without Liquid Water Transport." *J. Electrochemical Society* 150 (11): A1503-9.

[27] Mazumdar, S., and Cole, J. V. 2003. "Rigorous 3-D Mathematical Modeling of PEM Fuel Cells, II. Model Predictions with liquid Water Transport." *J. Electrochemical Society* 150 (11): A1510-7.

[28] Senn, S. M., and Poulikakos, D. 2004. "Polymer Electrolyte Fuel Cells with Porous Materials as Fluid Distributors and Comparisons with Traditional Channeled Systems." *J. Heat Transfer* 126 (3): 410-8.

[29] Wang, Y., and Wang, C. Y. 2006. "A Nonisothermal Two-Phase Model for Polymer Electrolyte Fuel Cells." *J. Electrochemical Society* 153 (6): A1193-200.

[30] Wu, H., Berg, P., and Li, X. 2008. "Steady and Unsteady

3D Non-isothermal Modeling of PEM Fuel Cells with the Effect of Non-equilibrium Phase Transfer." In *Proceedings of the 4th International Green Energy Conference*, 200-11.

[31] Li, Q., He, R., Jensen, J. O., and Bjerrum, N. J. 2003. "Approaches and Recent Development of Polymer Electrolyte Membranes for Fuel Cells Operating above 100 °C." *Chemical Material* 15 (26): 4896-915.

[32] Kramer, D., Zhang. J., Shimoi, R., Lehmann, E., Wokaun, A., Shinohara, K., and Sherer, G. G. 2005. "In situ Diagnostic of Two-Phase Flow Phenomena in Polymer Electrolyte Fuel Cells by Neutron Imaging, Part A. Experimental, Data Treatment, and Quantification." *Electrochimical Acta* 50 (13): 2603-14.

[33] Zhang, F. Y., Yang, X. G., and Wang, C. Y. 2006. "Liquid Water Removal from a Polymer Electrolyte Fuel Cell." *J. Elecrtrochemical Society* 153 (2): A225-32.

[34] Zhang, J., Kramer, D., Shimoi, R., Ono, Y., Lehmann, E., Wokaun, A., Shinohara, K., and Sherer, G. G. 2006. "In situ Diagnostic of Two-Phase Flow Phenomena in Polymer Electrolyte Fuel Cells by Neutron Imaging, Part B. Material Variations." *Electrochimical Acta* 51 (13): 2715-27.

[35] Springer, T. E., Zawodzinski, T. A., and Gottersfeld, S. 1991. "Polymer Electrolyte Fuel Cell Model." *J. Electrochemical Society* 138 (8): 2334-42.

[36] Jung, C. Y., Shim, H. S., Koo, S. M., Lee, S. H., and Yi, S. C. 2012. "Investigation of the Temperature Distribution in Proton Exchange Membrane Fuel Cells." *Applied Energy* 93 (May): 733-41.

[37] Ju, H., Meng, H., and Wang, C. Y. 2005. "A Single-Phase, Non-isothermal Model for PEM Fuel Cells." *International J. Heat and Mass Transfer* 48 (7): 1303-15.

[38] He, S., Mench, M. M., and Tadigadapa, S. 2006. "Thin Film Temperature Sensor for Real-Time Measurement of Electrolyte Temperature in a Polymer Electrolyte Fuel Cell." *Sensors and Actuators A* 125 (2): 170-7.

Journal of Energy and Power Engineering 9 (2015) 705-713
doi: 10.17265/1934-8975/2015.08.003

Microwave-Alkaline Assisted Pretreatment of Banana Trunk for Bioethanol Production

Egwim Evans Chidi, Shittu Kudirat Oluwatisin and Komolafe Deborah
Biochemistry Department, Federal University of Technology, Niger State PMB 65, Nigeria

Received: May 01, 2015 / Accepted: July 01, 2015 / Published: August 31, 2015.

Abstract: Pretreatment is one of the most important steps in the production bioethanol from lignocellulose materials. Alkaline pretreatment is a common mean of pretreatment but microwave oven could assist its efficiency as it can reduce the pretreatment time and improve the enzymatic activity during hydrolysis. The aim of this paper is to determine lignin removal from banana trunk using microwave-assisted alkaline (NaOH and NH_4OH) pretreatments. The best pretreatment conditions were used for mass pretreatment before hydrolysis and fermentation. The result shows that, optimum lignin removal was with microwave-assisted NaOH pretreatment with the removal of up to 98% lignin at 2% (*w*/*v* (weight/volum)) sodium hydroxide, 170 W microwave power at 10 min. Microwave-assisted ammonium hydroxide pretreatment achieved 97% lignin removal at 1% ammonium hydroxide concentration and 680 W microwave power at 5 min. Microwave- alkaline assisted pretreatment increased the yield and quality of fermentable sugar after enzyme hydrolysis with NH_4OH and ammonium hydroxide yielding 40% and 39% of ethanol, respectively. This result reveals that, well controlled microwave- alkaline assisted pretreatment of banana trunk could effectively remove lignin and give high bioethanol yield.

Key words: Microwave, alkali, pretreatment, cellulosic, banana trunk, bioethanol.

1. Introduction

Bioethanol or ethyl alcohol (C_2H_5OH) is a colourless gaseous or liquid fuel derived from hydrolysis and fermentation of glucose from cellulose biomass. It is produced from distillation of ethanolic waste gotten from fermentation of cellulosic biomass [1]. Bioethanol can be produced from biomasses containing cellulose such as agricultural waste, woody materials, by-product of organic materials, forest residues, herbaceous material, municipal waste, etc. [2]. Alternative liquid fuels from various sources have been sought for many years, and since the cost of raw materials which can account up to 50% of the total production, cost is one of the most significant factors to affect the economy of alcohol, nowadays, efforts are more concentrated on using cheap and abundant raw materials [3]. No other sustainable option for production of transportation fuels can match ethanol made from lignocelluloses biomass with respect to its dramatic environmental, economic and infrastructure advantages [4]. The lignocellulosic materials include agricultural residues, MSW (municipal solid wastes), pulp mill refuse, switch grass and lawn, garden wastes [5, 6]. The structures of lignocellulose material are rigid and recalcitrant. These characteristics provide plant it mechanical support and prevent it from chemical degradation and enzymatic hydrolysis for bioethanol production [7]. Pretreatment of lignocellulose biomass for bioethanol production is an important process step done to remove lignin and hemicellulose from biomass so that the residual cellulose can be hydrolyzed to fermentable sugar [8]. Acid pretreatment of biomass result in disruption of covalent bond, hydrogen bond and Vander Waals forces holding the constituent of the biomass together therefore resulting in the solubilisation and

Corresponding author: Egwim Evans Chidi, Ph.D., associate professor, research fields: industrial biochemistry and bioprocess. E-mail: evanschidi@gmail.com, c.egwim@futminna.edu.ng.

decrystallization of biomass [9]. Alkali pretreatment on the other hand causes swelling of biomass through saponification reaction [10]. Alkali pretreatment disrupts the structure of lignin and breaks the bond between lignin and other cellulose component of biomass thereby increasing their susceptibility to enzymatic hydrolysis [8]. Enzymatic hydrolysis involves mixture of enzymes such as cellulose and hemicellulases [11]. These enzymes must be able to break down lignocellulosic materials and convert it to fermentable glucose [12]. Enzymatic hydrolysis has low utility lost compare to acid hydrolysis and environmental friendly [13]. Banana truck is a promising cellulose and lignocellulosic plant which generates a significant amount of waste, approximately 200 t/ha/year [14]. Despite its cellulose (63%-64%) and hemicellulose (19%) content [15], it is not often used as a raw material for bioethanol production probably due to its lignin content (15.07%). The aim of this study is to determine lignin removal of banana trunk using alkaline pretreatment (NaOH and NH_4OH) microwave assisted alkaline pretreatment. The effectiveness of these pretreatments was evaluated by bioethanol yield through fermentation.

2. Materials and Methods

Materials used are of analytical grades unless otherwise stated. Methods followed the stages and steps as outlined.

2.1 Collection of Samples

Banana trunk was collected from Bosso, Minna, and was dried in an oven and grinded to powder. The sample was further sieved into smaller particles and kept for further analysis.

2.2 Chemicals

Sodium hydroxide (NaOH), ammonium hydroxide (NH_4OH) and distilled water.

2.3 Chemical Pretreatment

Banana trunk biomass was subjected to pretreatment with sodium hydroxide (NaOH) of 2%, 4%, 6%, 8% and 10% concentration in the ratio 10:1, and then placed in the water-bath with temperature of 60, 70, 80, 90 and 100 °C for 1 h, banana trunk was also immersed in ammonium hydroxide (NH_4OH) with the concentration of 1%, 2%, 3%, 4%, 5% and also placed in the water-bath for 1 h with the temperature ranging from 60 °C to 100 °C. The mixture was then filtered with muslin cloth and the residue was washed with clean water until the pH was neutral and dried in an oven to remove excess water and moisture and then kept for further analysis.

2.4 MAA (Microwave Assisted Alkaline) Pretreatment

Banana trunk powder was immersed in 2%, 4%, 6%, 8% and 10% NaOH solution in the ratio of 10:1 of liquid to solid (*v*/*w* (volum/weight)). The mixture was then placed in a microwave oven 5, 10, 15, 20 and 25 min at the varying power of 170, 340, 510, 680 and 850 W. After this process, the mixture was then filtered and the residue was washed with clean water until the pH was neutral and the dried in the oven and kept afterwards for further analysis. Also the sample was immersed in ammonium hydroxide (NH_4OH) with the varying concentration of 1%, 2%, 3%, 4% and 5% in the ratio of 10:1 and was then placed in a microwave oven for 5, 10, 15, 20 and 25 min at varying power of microwave oven at 170, 340, 510, 680 and 850 W. The sample was then filtered and the residue was washed with clean water until the pH was neutral and afterwards dried in the oven to remove water and moisture. The dried residue was then kept for further analysis. Optimum condition obtained from both microwave-assisted alkaline pretreatments were used generate bulk pretreated banana trunk biomass. This biomass was thereafter hydrolyzed with cellulose and fermentation to produce bioethanol.

3. Results and Discussion

Lignin removal using ammonium hydroxide (NH_4OH) and sodium hydroxide (NaOH) in water bath

pretreatments are shown in Figs. 1 and 2. The reduction in the weight of the residue is proportional to the lignin removed. The effect of NH_4OH concentration is not significant on lignin removal at 60 °C and 70 °C. The highest removal of legnin was observed with 2% NH_4OH at 100 °C. On the other hand, lowest removal of legnin was found at 100 °C with 4% NH_4OH.

Concentration of NaOH had significant influence on lignin removal as shown in Fig. 2. It was found that, when NaOH concentration increased from 2% to 10%, there was general reduction in the weight of residual sample at some of the experimental temperatures (70, 90 and 100 °C). The highest biomass reduction (lignin removal) was observed with 8% NaOH at 80 °C [16],

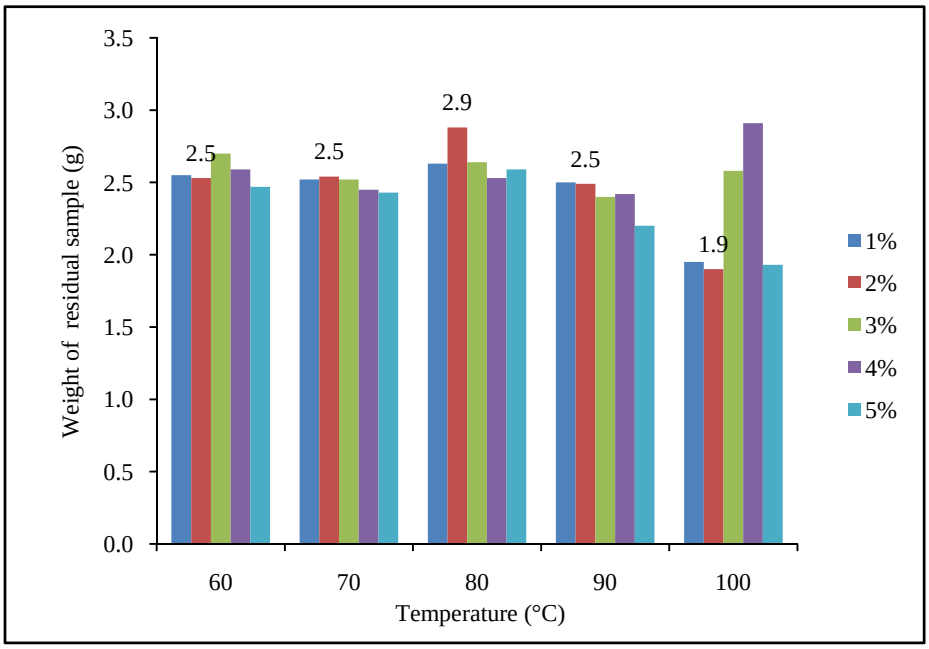

Fig. 1 Mean weight of residual biomass after pretreatment with ammonium hydroxide with the aid of water bath at different temperature.

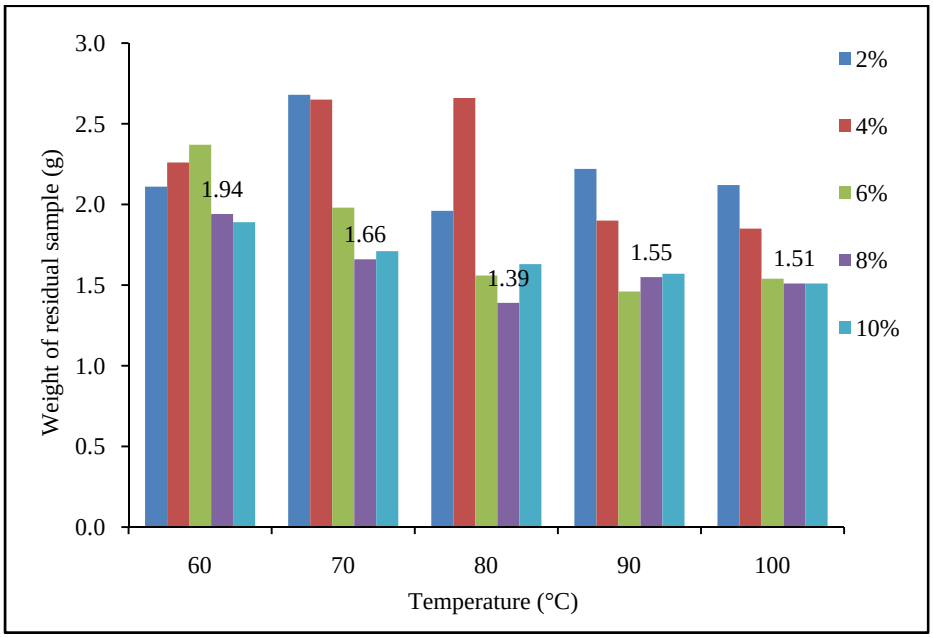

Fig. 2 Mean weight of residual biomass after pretreatment with sodium hydroxide with the aid of water bath at different temperature.

studied the effectiveness of sulfuric acid, sodium hydroxide, hydrogen peroxide and ozone pretreatments for enzymatic conversion of cotton stalks. They found that, 2% sodium hydroxide pretreatment resulted in the highest level of delignification at 121 °C. Earlier studies have shown that, 2% sodium hydroxide, would remove up to 65% lignin in corn stover [17]. Also [18] achieved over 55% reduction in the lignin content within first 0.5 h of pretreatment using 0.5% sodium hydroxide solution at 120 °C. The pretreatment achieved in this study is in correlation with previous studies based on the suggestion of alkaline pretreatment at lower temperature with high alkaline concentration or vice versa [19]. Sodium hydroxide solution has shown to be more effective in deligninfication of banana trunk biomass than aqueous ammonium hydroxide. Sodium hydroxide is one of the most effective alkaline reagents and has been used to treat a variety of lignocellulosic feedstock [20].

3.1 Microwave-Assisted Alkaline Pretreatment

NaOH and NH_4OH are dipolar reagents and the alignment and migration of their charged ions and water molecules in rapidly alternating electromagnetic field results in a friction which generate heat within a short period of time in microwave system. The electromagnetic field of microwave irradiation applies force that changes their direction rapidly at the rate of 2.4×10^9 times per second [21]. These characteristics can increase the process of chemical, biological and physical pretreatment [22].

3.1.1 Graphical Representation of Microwave-Assisted Sodium Hydroxide Pretreatment at Varied Time Using Surfer-11 Model

Generally, microwave assisted pretreatment using different concentrations of ammonium hydroxide yielded the lowest weight delignification at the concentration of 1% and irradiation power of 680 W after time 10 min of pretreatment. This is because extended pretreatment [23] and charring of the sample at very high temperature (850 W) during microwave assisted alkaline pretreatment [24] is likely to result in loss of carbohydrates to the pretreatment liquor. (Figs. 3-12). However, the present study has shown that, microwave-assisted sodium hydroxide pretreatment at 2% (*w*/*v*) concentration, 170 W for 10 min (Fig. 4) was the best conditions for delignification of banana trunk biomass.

The result shows a rise and fall pattern in weight of sample as the power of irradiation and concentration of sodium hydroxide is increased but shows the lowest reduction at concentration of 8% and power of 680 W.

Microwave assisted pretreatment using different concentration of sodium hydroxide at different power shows an increase delignification as the irradiation power and concentration of NaOH increased. The optimum condition of pretreatment was observed at 2% NaOH and 170 W irradiation power. This optimum condition gave the overall highest delignification of banana trunk cellulose.

The pretreatment condition at 15 min shows a rise and fall pattern as the irradiation power and concentration of NaOH was increased, and the lowest weight of residual cellulose was 1.26 and was observed as the concentration and power were increased.

Pretreatment condition at 20 min shows a rise and fall pattern in the weight of residual sample. Increase in the irradiation power and concentration reduces the weight of the residual sample.

Microwave assisted pretreatment using different irradiation power and concentrations of sodium hydroxide shows a rise and fall pattern in the weight of residual cellulose, and the optimum condition was observed at 2% NaOH and 170 W irradiation power.

3.1.2 Graphical Representation of Microwave Assisted Ammonium Hydroxide Pretreatment Using Surfer-11 Model

Microwave assisted pretreatment using ammonium hydroxide of different concentration and irradiation power shows a rise and fall pattern of residual weight but gives a sharp fall at 680 W of irradiation power.

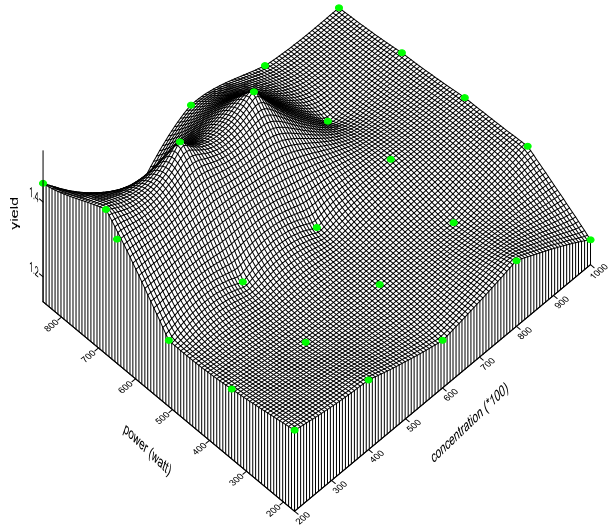

Fig. 3 Microwave assisted pretreatment using sodium hydroxide for 5 min.
Regression coefficient Z (X, Y) = A00 + A01 (Y) + A10 (X);
A00 = 1.3592;
A01 = $7.764705882363 \times 10^{-0.05}$;
A10 = -0.00136;
Coefficient of multiple determination (R^2) = 0.210322865663;
Surface definition = simple planar surface;
X = Concentration, Y = Power, Z = Weight of residual sample after pretreatment for 5 min.

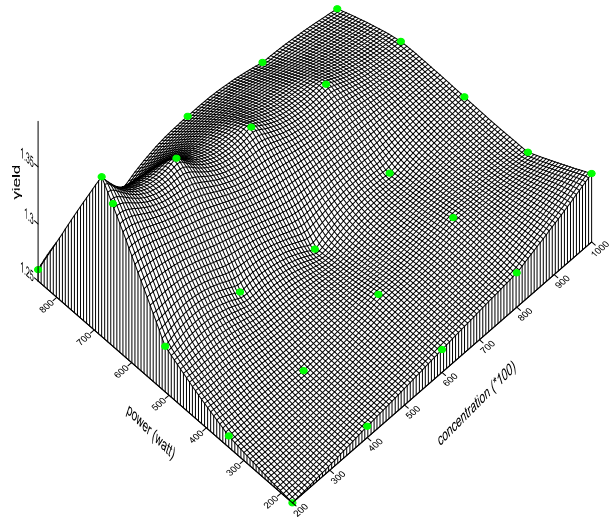

Fig. 4 Microwave assisted pretreatment using sodium hydroxide for 10 min.
Regression coefficient Z (X, Y) = A00 + A01 (Y) + A10 (X);
A00 = 1.2756;
A01 = $2.4706882352943 \times 10^{-0.05}$;
A10 = $-9 \times 10^{-0.05}$;
Coefficient of multiple regression (R^2) = 0.0436746987952;
Surface definition = simple planar surface;
X = Concentration, Y = Power, Z = Weight of residual sample after pretreatment for 10 min.

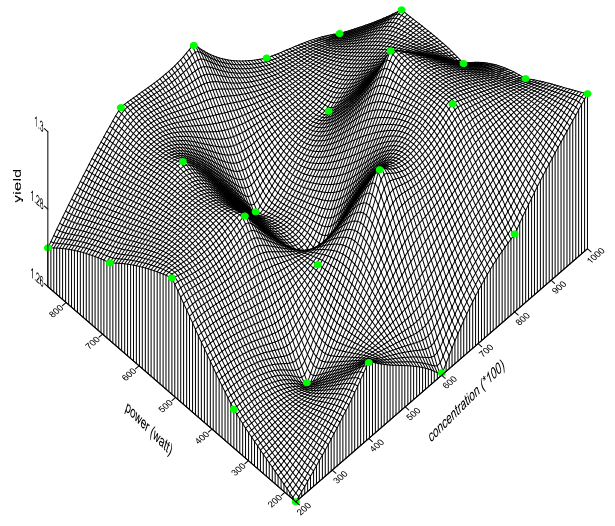

Fig. 5 Microwave assisted pretreatment using sodium hydroxide for 15 min.
Regression coefficient Z (X, Y) = A00 + A01 (Y) + A10 (X);
A00 = 1.2762;
A01 = $-4.7058823529407 \times 10^{-0.06}$;
A10 = $-9 \times 10^{-0.06}$;
Coefficient of multiple regression (R^2) = 0.0389245585875;
Surface definition = simple planar surface;
X = Concentration, Y = Power, Z = weight of residual sample after pretreatment for 15 min.

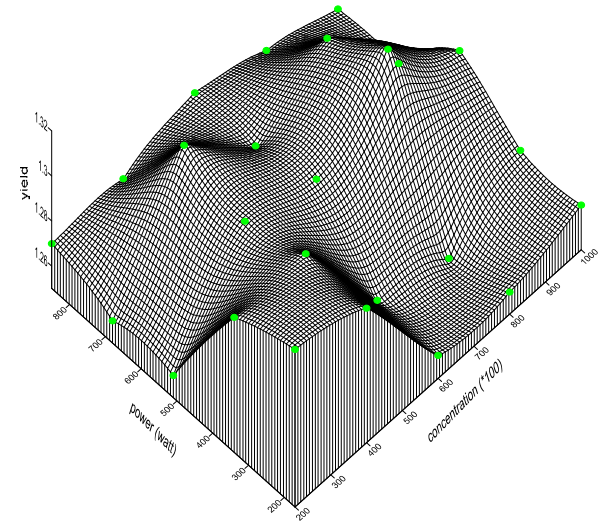

Fig. 6 Microwave assisted pretreatment using sodium hydroxide for 20 min.
Regression coefficient Z (X, Y) = A00 + A01 (Y) + A10 (X);
A00 = 1.3038;
A01 = $-1.5294117647057 \times 10^{-0.05}$;
A10 = $-2.4 \times 10^{-0.05}$;
Coefficient of multiple regression (R^2) = 0.124832439678;
Surface definition = simple planar surface;
X = Concentration, Y = Power, Z = weight of residual sample after pretreatment for 20 min.

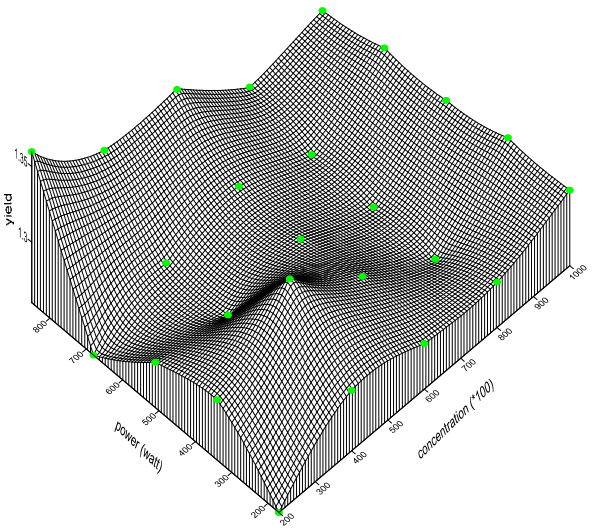

Fig. 7 Microwave assisted pretreatment using sodium hydroxide for 25 min.

Regression coefficient Z (X, Y) = A00 + A01 (Y) + A10 (X);
A00 = 1.2912;
A01 = $1.4117647058825 \times 10^{-0.06}$;
A10 = $-6.0000000000018 \times 10^{-0.06}$;
Coefficient of multiple regression (R^2) = 0.02722323049;
Surface definition = simple planar surface;
X = Concentration, Y = Power, Z = weight of residual sample after pretreatment for 25 min.

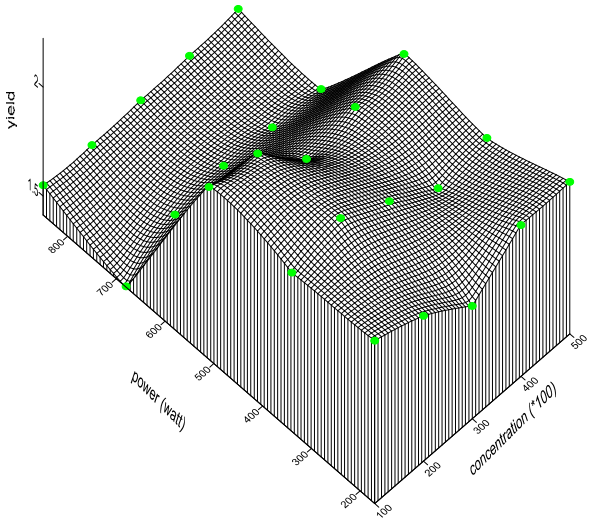

Fig. 8 Microwave assisted pretreatment using ammonium hydroxide for 5 min.

Regression coefficient Z (X, Y) = A00 + A01 (Y) + A10 (X);
A00 = 2.3644;
A01 = -0.00093176470688205;
A10 = -0.000614;
Coefficient of multiple regression (R^2) = 0.68979218801;
Surface definition = simple planar surface;
X = Power, Y = Concentration, Z = weight of residual sample after pretreatment for 5 min.

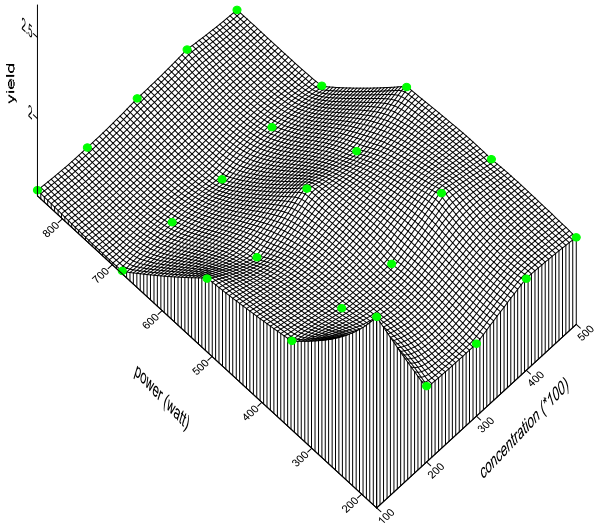

Fig. 9 Microwave assisted pretreatment using ammonium hydroxide for 10 min.

Regression coefficient Z (X, Y) = A00 + A01 (Y) + A10 (X);
A00 = 2.4112;
A01 = 0.001001764705882;
A10 = 0.000162;
Coefficient of multiple regression (R^2) = 0.72741588692;
Surface definition = simple planar surface;
X = Power, Y = Concentration, Z = weight of residual sample after pretreatment for 10 min.

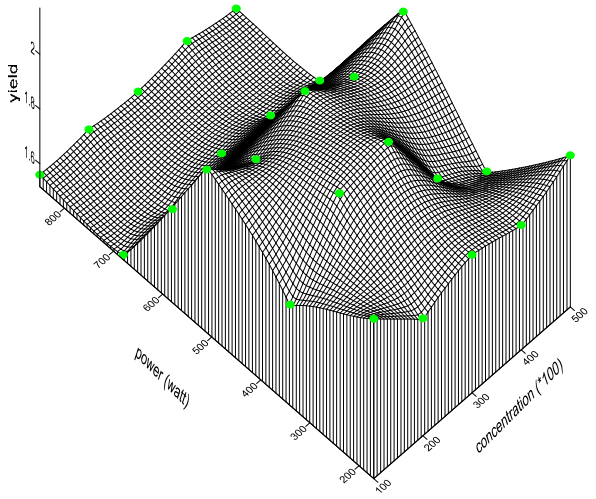

Fig. 10 Microwave assisted pretreatment using ammonium hydroxide for 15 min.

Regression coefficient Z (X, Y) = A00 + A01 (Y) + A10 (X);
A00 = 2.668;
A01 = -0.00078;
A10 = -0.000134;
Coefficient of multiple regression (R^2) = 0.621727953942;
Surface definition = simple planar surface;
X = Power, Y = Concentration, Z = weight of residual sample after pretreatment for 15 min.

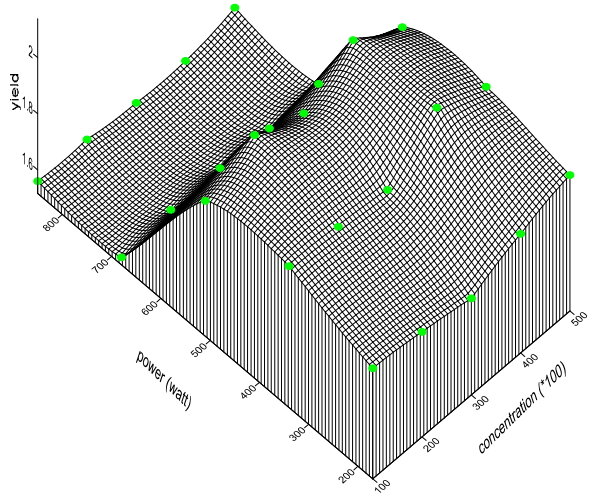

Fig. 11 Microwave assisted pretreatment using ammonium hydroxide for 20 min.

Regression coefficient Z (X, Y) = A00 + A01 (Y) + A10 (X);
A00 = 2.156;
A01 = -0.00071647058823529;
A10 = 0.000114;
Coefficient of multiple regression (R^2) = 0.572491400311;
Surface definition = simple planar surface;
X = Power, Y = Concentration, Z = weight of residual sample after pretreatment for 20 min.

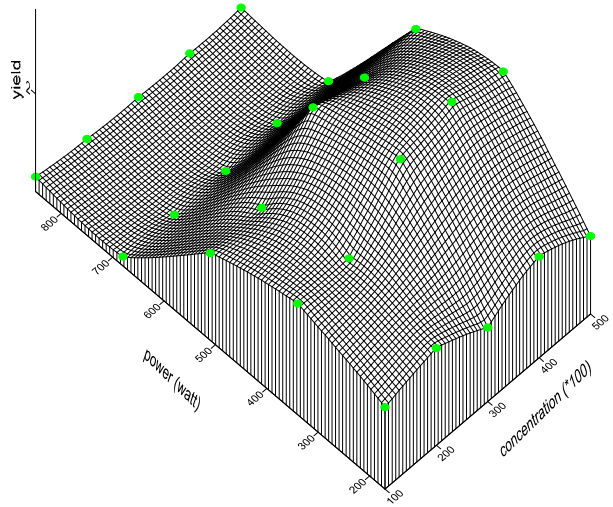

Fig. 12 Microwave assisted pretreatment using ammonium hydroxide for 25 min.

Regression coefficient Z (X, Y) = A00 + A01 (Y) + A10 (X);
A00 = 2.234;
A01 = -0.00087882352941177;
A10 = 0.000318;
Coefficient of multiple regression (R^2) = 0.508299550688;
Surface definition = simple planar surface;
X = Power, Y = Concentration, Z = weight of residual sample after pretreatment for 25 min.

Pretreatment condition for 10 min gives a gradual reduction in weight of residual sample and a sharp decrease when the irradiation power was increased to 680 W. The optimum condition yielding 1.53 g was observed at concentration of 1% NH_4OH at irradiation power 680 W.

Pretreatment condition after 15 min shows a rise and fall pattern in the weight of residual cellulose and a sharp reduction was observed at 680 W. The optimum conditions of pretreatment after 15 min were observed as the concentration and power was increased at 3% and 5% NH_4OH and power irradiation of 680 W and 850 W, respectively.

Pretreatment condition after 20 min of pretreatment with microwave irradiation shows a gradual fall in the weight of residual cellulose and a sharp reduction at 680 W. Increase in concentration of NH_4OH on the other hand produces a rise and fall pattern in the weight of residual cellulose.

Pretreatment condition after 25 min shows a gradual rise and fall in the weight of residual cellulose and a sharp decrease when power was increased to 680 W. The optimum yield was observed at 680 W and 850 W.

This implies that, low power, short time and low concentration of sodium hydroxide were required for high removal of lignin when using microwave radiation. The present observation agrees with that of [25] who observed that, the pretreatment of Bermuda grass with microwave assisted sodium hydroxide pretreatment yielded optimum result at the irradiation power of 250 W, 1% NaOH concentration for 10 min which removed 65% of lignin while retaining 87% of the glucan. Furthermore, the weight of residual sample reduction in microwave-assisted sodium hydroxide pretreatment (Fig. 4) was higher than that of NaOH pretreatment alone (Fig. 2). This observation supports the finding of [26] who reported that, during alkali pretreatment of wheat straw, with microwave assisted heating, lower sugars losses and higher hydrolysis rates were observed than that of conventional alkaline pretreatment alone.

Microwave assisted ammonium hydroxide pretreatment showed lowest delignification at 1% (*w*/*v*) concentration, 680 W under 10 min (Fig. 9) indicating that, high power, short time and low concentration of alkali were required for high removal of lignin. Although microwave-assisted ammonium hydroxide pretreatment yielded better delignification of banana trunk biomass at lower alkaline concentration than microwave-assisted NaOH pretreatment, microwave-assisted ammonium solution was considered as less efficient due to the tendency of reduced sugar yields during hydrolysis when using high power microwave assisted alkaline pretreatment [24]. However, microwave assisted ammonium hydroxide pretreatment was prefer over the convention ammonium hydroxide pretreatment alone (Fig. 1) as a result of the shorter time (10 min) and lower ammonium concentration (1%) required. It is therefore clear from this study that, microwave assisted pretreatment achieves better delignification of banana trunk biomass than pretreatment with sodium hydroxide and ammonium hydroxide alone.

Enzymatic hydrolysis and fermentation of pretreated biomass obtained from the optimum conditions of microwave assisted sodium hydroxide pretreatment yields 300 mL of 40% bioethanol, while microwave-assisted ammonium hydroxide pretreatment yields 150 mL of 39% bioethanol. Many reports have shown that, short pretreatment duration when using microwave radiation enhances the destruction of crystalline arrangement of starch in their hydrolysis to reducing sugar [27].

4. Conclusions

The result obtained from this study shows that, dilute sodium hydroxide (NaOH) of 2% at 170 W with microwave irradiation exposure of 10 min yields the highest amount of reducing sugar for bioethanol production. Therefore, dilute alkaline pretreatment when combined with microwave irradiation is a promising method for lignin removal from lignocellulose biomass, although more researches are still focused on how to improve this method for a better yield. The use of dilute sodium hydroxide at low irradiation power for microwave assisted alkaline pretreatment is an effective way of removing lignin from lignocellulose biomass under short period of time, and hence gives a higher turnover rate of bioethanol production.

Acknowledgments

This research was fully supported by TETFUND Institutional research grant TETFUND-Institutional—Based Research Intervention/Federal University of Tecnology Minna (TETFUND/UTMINNA)/2014/27). The authors also acknowledge the used of faclities in the STEPB (Science Technology and Post Basic) studies laboratory, Federal University of Technology Minna.

References

[1] Graeme, M. W. 2010. *Bioethanol: Science and Technology of Fuel Alcohol.* Copenhagen: Graeme M. Walker & Ventus Publishing Aps, 49-52.

[2] Mustafa, B., and Havva, B. 2009. “Recent Trend in Global Production and Utilization of Bio ethanol Fuel.” *Applied Energy* 86 (11): 2273-82.

[3] Licht, F. O. 2006. *World Ethanol Markets: The Outlook to 2015.* Agra Europe special report: Tunbridge Wells.

[4] Taherzadeh, M. J., and Karimi, K. 2007. “Acid-Based Hydrolysis Processes for Ethanol from Lignocellulosic Materials: A Review.” *Bio Resources* 2 (3): 472-99.

[5] Isa, B., Post, J., and Furedy, C. 2004. *Solid Waste Management and Recycling; Actors, Partnerships and Policies in Hyderabad, India and Nairobi, Kenya.* Dordrecht: Kluwer Academic Publishers.

[6] Ghosh, S., Henry, M. P., Sajjad, A., Mensinger, M. C., and Arora, J. L. 2000. “Pilot-Scale Gasification of Municipal Solid Wastes by High-Rate and Two-Phase Anaerobic Digestion (TPAD).” *Water Sci. Technol.* 41 (3): 101-10.

[7] Himmel, M. E., Ding, S. Y., Johnson, D. K., Adney, W. S., Nimlos, M. R., Brady, J. W., and Foust, T. D. 2007. “Biomass Recalcitrance: Engineering Plants and Enzymes for Biofuels Production.” *Science* 315 (5813): 804-7.

[8] Mosier, N., Wyman, C., Dale, B., Elander, R., Lee, Y. Y., Holtzapple, M., and Ladisch, M. 2005. “Features of Promising Technologies for Pretreatment of Lignocellulosic Biomass.” *Bioresource Technol.* 96 (6): 673-86.

[9] Li, C., Knierim, B., Manisseri, C., Arora, R., Scheller, H. V., Auer, M., Vogel, K. P., Simmons, B. A., and Singh, S. 2010. "Comparison of Dilute Acid and Ionic Liquid Pretreatment of Switchgrass: Biomass Recalcitrance, Delignification and Enzymatic Saccharification." *Bioresource Technology* 101 (13): 4900-6.

[10] Xu, J., Cheng, J. J., Sharma-Shivappa, R. R., and Burns, J. C. 2010. "Sodium Hydroxide Pretreatment of Switch Grass for Ethanol Production." *Energy Fuels* 24 (3): 2113-9.

[11] Puwardi, R. 2006. "Continuous Ethanol Production from Dilute Acid Hydrolysate: Detoxification and Fermentation Strategy." *Dept. Chemical and Biological Engineering, ChalmerTekniska, Goteborg* 114 (1-2): 187-98.

[12] Sun, Y., and Cheng, J. 2012. "Hydrolysis of Lignocellulosic Materials for Ethanol Production: A Review." *Bioresource Technology* 83 (1): 1-11.

[13] Nurhasiken, R. B. 2010. *Production of Glucose from Banana Stem Waste Using Strain A (Thesis Faculty of Chemical and Natural Resources Engineering).* Malaysia: University of Malaysia Pahang.

[14] Soffner, M. L. A. O. 2001. "Pulp Production from Banana Stem." Master thesis, University of Sao Paulo.

[15] Marie-Angel, A., KEtty, B., Holmer, S. J., and Khosrow, G. 2013. "Treatment of Non-wood Plant Fibers Used as Reinforcement in Composite Materials." *Materials Research* 16 (4): 903-23.

[16] Silverstein, R. A., Chen, Y., Sharma-Shivappa, R. R., Boyette, M. D., and Osborne, J. A. 2007. "Comparison of Chemical Pretreatment Methods for Improving Saccharification of Cotton Stalks." *Bioresource Technology* 98 (16): 3000-11.

[17] Macdonald, D. G., Bakhshi, N. N., Mathews, J. F., and Roychowdhury, A. 1983. "Alkaline Pretreatment of Corn Stover to Improve Sugar Production by Enzymatic Hydrolysis." *Biotechno. Bioeng.* 25: 2067-70.

[18] Soto, M. L., Domínguez, N. M. J., and Lema, J. M. 1994. "Enzymatic Saccharification of Alkali-Treated Sunflower Hulls." *Bioresour. Technol.* 49 (1): 53-9.

[19] Curreli, N., Fadda, M. B., Rescigno, A., Rinaldi, A. C., Soddu, G., Sollai, F., Vaccargiu, S., Sanjust, E., and Rinaldi, A. 1997. "Mild Alkaline/Oxidative Pretreatment of Wheat Straw." *Process Biochem.* 32 (8): 665-70.

[20] Sharmas, S. K., Kalar, K. L., and Grewal, H. S. 2002. "Enzymatic Saccharification of Pretreated Sunflower Stalks." *Biomass Bioenergy* 23 (3): 237-43.

[21] Galema, S. A. 1997. "Microwave Chemistry." *Chemical Society Reviews* 26 (3): 233-8.

[22] Sridar, V. 1998. Microwave Radiation as a Catalyst for Chemical Reactions." *Current Science* 74 (5): 446-50.

[23] Saifuddin, M. N., Refal, H., and Kumaran, P. 2013. "Microwave-Assisted Alkaline Pretreatment and Microwave Assisted Enzymatic Saccharification of Oil Palm Empty Fruit Bunch Fiber for Enhanced Fermentable Sugar Yield." *Journal of Sustainable Bioenergy Systems* 3 (2): 7-17.

[24] Deepak, R. K., and Jay, J. C. 2009. "Switchgrass for Bioethanol and Other Value-Added Application: A Review." *Biological System Engineering* 100 (4): 1514-23.

[25] Binod, P., Satyanagalakshimi, K., Sindhu, R., UshaJanu, K., Sukumaran, R. K., and Pandey, A. 2012. "Short Duration Microwave Assisted Pretreatment Enhances the Enzymatic Saccharification and Fermentable Sugar Yield from Sugarcane Bagasse." *Renewable Energy* 37 (4): 109-16.

[26] Zhu, S., Wu, Y., Yu, Z., Chen, Q., Wu, G., Yu, F., Wang, C., and Jin, S. 2006. "Microwave Assisted Alkali Pre-treatment of Wheat Straw and Its Enzymatic Hydrolysis." *Process Biochemistry* 94 (3): 437-42.

[27] Palav, T., and Seetharaman, K. 2007. "Impact of Microwave Heating on the Physico-Chemical Properties of a Starch Water Model System." *Carbohydrate Polymers* 67 (4): 596-604.

Journal of Energy and Power Engineering 9 (2015) 714-720
doi: 10.17265/1934-8975/2015.08.004

Optical Design of a Solar Parabolic Concentrating Collector Based on Trapezoidal Reflective Petals

Saša Pavlović[1], Velimir Stefanović[1], Darko Vasiljević[2] and Emina Petrović[3]

1. Thermal Engineering Department, Faculty of Mechanical Engineering University of Nis, Niš 18000, Serbia

2. Institute of Physics, Photonics Center, Belgrade 11080, Serbia

3. Mechatronic and Control System, Faculty of Mechanical Engineering University of Nis, Niš 18000, Serbia

Received: February 06, 2015 / Accepted: April 01, 2015 / Published: August 31, 2015.

Abstract: In this paper, detailed optical of the solar parabolic dish concentrator is presented. The system has diameter D = 2,800 mm and focal length f = 1,400 mm. The efficient conversion of solar radiation in heat at these temperature levels requires a use of concentrating solar collectors. In this paper, detailed optical design of the solar parabolic dish concentrator is presented. The parabolic dish of the solar system consists from 12 curvilinear trapezoidal reflective petals. This paper presents optical simulations of the parabolic solar concentrator unit using the ray-tracing software TracePro. The total flux on receiver and the distribution of irradiance for absorbed flux on center and periphery receiver are given. The total flux at the focal region is 4,031.3 W. The goal of this paper is to present optical design of a low-tech solar concentrator, that can be used as a potentially low-cost tool for laboratory-scale research on the medium-temperature thermal processes, cooling, industrial processes, solar cooking and polygeneration systems, etc.

Key words: Solar parabolic dish concentrator, optical analysis, solar energy, solar radiation.

1. Introduction

The device which is used to transform solar energy to heat is referred to a solar collector. Solar thermal collectors have been widely used to concentrate solar radiation and convert it into medium-high temperature thermal processes. They can be designed as various devices including solar cooker [1], solar hydrogen production [2, 3] and Dish Stirling system of harvest electricity [4, 5]. The main types of concentrating collectors are: parabolic dish, parabolic trough, power tower, and Fresnel collector with mirror or lens and stationary concentrating collectors. The ideal optical configuration for the solar parabolic thermal concentrator is a parabolic mirror. The parabolic mirror is very expensive to fabricate and it is cost escalating rapidly with increase of aperture area. The parabolic mirror can be designed with large number of elementary components known as reflecting petals or facets. Usually reflecting petals are made from glass and their thickness is from 0.7 mm to 1.0 mm. Traditionally, the optical analysis of radiation concentrators has been carried out by means of computer ray-trace programs. Recently, an interesting analytical solution for the optical performance of parabolic dish reflectors with flat receivers was presented by O'Neill and Hudson [6].

Their method for calculating the optical performance is fast and accurate but assumes that the radiation source is a uniform disk. Imhamed, et al. [7] have presented study that aims to develop a 3-D static solar concentrator that can be used as low cost and low energy substitute. Their goals were to design solar concentrator for production of portable hot water in rural India. They used ray tracing software for evaluation of the optical performance of a static 3-D EHC (elliptical hyperboloid concentrator). Optimization of the concentrator profile and geometry

Corresponding author: Saša Pavlović, research associate, research field: solar energy system. E-mail: saledoca@gmail.com.

is carried out to improve the overall performance of system. Kashika and Reddy [8] used satellite dish of 2.405 m in diameter with aluminium frame as a reflector to reduce the weight of the structure and cost of the solar system. In their solar system, the average temperature of water vapor was 300 °C, when the absorber was placed at the focal point. Cost of their system was US$ 950. Ouederni, et al. [9] was testing parabolic concentrator of 2.2 m in diameter with reflecting coefficient 0.85. Average temperature in their system was 380 °C. Rafeeu and AbKadir [10] have presented simple exercise in designing, building and testing small laboratory scale parabolic concentrators. They made two dishes from acrylonitrile butadiene styrene and one from stainless steel. Three experimental models with various geometrical sizes and diameters were used to analyze the effect of geometry on a solar irradiation. Zhiqiang, et al. [11] presented a procedure to design a facet concentrator for a laboratory-scale research on medium—temperature thermal processes. The facet concentrator approximates a parabolic surface with a number of flat square facets supported by a parabolic frame and having two edges perpendicular to the concentrator axis. A 164—facet concentrator will deliver up to 8.15 kW of radiative power over 15 cm radius disk located in the focal plane. Their system had average concentration ratio exceeding 100. Ahmed and Khan [12] presented two prototype parabolic dishes: the Shenandoah dish and the parabolic dish concentrator, in jet propulsion laboratory. The Shenandoah dish was designed to heat silicone oil in one pass to 400 °C. The Shenandoah dish is 7 m parabolic reflecting dish formed from 21 aluminum petals covered with special reflective layer on one side. The second parabolic dish (JPL parabolic dish concentrator) has parabolic reflector surface with 12 m diameter. Rebecca, et al. [13] investigated experimental evaluation of ammonia receiver geometries with a 9 m^2 dish concentrator. The 20 m^2 dish is mirrored with around 2,000 flat mirror tile facets arranged in concentric rings on a parabolic fiber glass support structure. Size of mirror facets is from 5 cm to 10 cm. Glen, et al. [14] analyzed optical performance of spherical reflecting elements for use with parabolic dish concentrators. This concentrator consists of 54 triangular mirrors. The effective rim angle for the dish is 46°. The 54 units are composed of nine separate panel shapes, each of shapes is duplicated six times. The focal length of system is 13.1 m. They compared the optical performances and manufacturing feasibility of collectors having such a combination of surfaces.

The decision to make solar parabolic concentrator with 12 petals is based on large number of design concepts that are realized in the world. This concept already proved useful in solar techniques, especially in production of heat and electrical energy as well as in trigeneration and polygeneration systems.

The basic idea behind this research is to start with primary concept of solar parabolic concentrator which will generate from 10 kW to 25 kW in polygeneration systems. Only with employment of parabolic concentrating systems, it is possible to obtain high temperatures in range from 200 °C to 800 °C and high thermal efficiency.

2. Optical Design of the Solar Parabolic Thermal Concentrator

The optical design of the solar parabolic thermal concentrator and operation are presented. Optical design is based on parabolic dish with 12 curvilinear trapezoidal petals. Solar dish concentrators are generally concentrators that concentrate solar energy in a small area known as focal point. Dimensions of reflecting surfaces in solar dish concentrator are determined by desired power at maximum levels of insolation and efficiency of collector conversion. Mathematical representation of parabolic concentrator is paraboloid which can be represented as a surface obtained by rotating parabola around axis which is shown in Fig. 1.

Mathematical equations for the parabolic dish solar

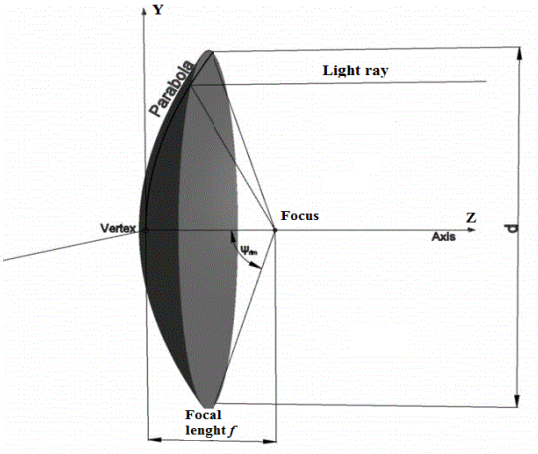

Fig. 1 Ideal shape of parabolic solar concentrator.

concentrator (Fig. 1) in Cartesian and cylindrical coordinate systems are defined as:

$$x^2 + y^2 = 4fz$$
$$z = r^2/4f \quad (1)$$

where, x and y are coordinates in aperture plane; and z is distance from vertex measured along the line parallel with the paraboloid axis of symetry; f is focal length of paraboloid i.e., distance from the vertex to the focus along the aparboloid axis of symmetry. The relationship between the focal length and the diameter of parabolic dish is known as the relative aperture and it defines shape of the paraboloid and position of focal point. The shape of paraboloid can be also defined by rim angle ψ_{rim}. Usually paraboloids that are used in solar collectors have rim angles from 10° up to 90°. The relationship between the relative aperture and the rim angle is given by:

$$f/_D = \frac{1}{4\tan(\psi_{rim}{}^2)} \quad (2)$$

The paraboloid with small rim angles have the focal point and receiver at large distance from the surface of concentrator. The paraboloid with rim angle smaller than 50° is used for cavity receivers while paraboloids with large rim angles are most appropriate for the external volumetric receivers (central receiver solar systems).

The geometric concentration ratio can be defined as the area of the collector aperture A_{app} divided by the surface area of the receiver A_{rec} and can be calculated by Eq. (3):

$$CR_g = \left(\sin^2\theta_a\right)^{-1} = A_c A_r^{-1} = A_{app} / A_{rec} \quad (3)$$

The designed solar parabolic concentrator has geometric concentration ratio CR = 13,615.

Flux concentrating ratio can be defined as ratio of flux concentrated in a point I to incident solar flux $I_{b,n}$:

$$CR_{flux} = \frac{I}{I_{b,n}} \quad (4)$$

2.1 Design Description of Solar Parabolic Concentrator

Mechanical design of the solar parabolic concentrator is done in 3D design software CATIA, Dassault systems, USA. Parabolic shape of solar concentrator is obtained by entering X and Y coordinates for selected points. For calculation of necessary points that define parabola public domain software Parabola Calculator 2.0 is used. The calculated coordinates (X and Y) for designed parabola are shown in Table 1.

Geometrical model of solar parabolic concentrator is parametrically designed from calculated coordinates and it is shown in Fig. 2. Selected model of solar dish concentrator with 12 petals requires very precise definition of parameters during geometrical modelling of system. Results obtained by optical analysis of solar concentration system are very much dependent on the selected method of the geometrical model generation.

A truncated paraboloid of revolution (circular paraboloid) is obtained by rotating the parabola segment about its axis (Fig. 3).

Consider a concentrator consisting of 12 trapezoidal reflective petals of identical non-overlapping trapezoidal segments. 3D model of trapezoidal reflective petal of solar parabolic concentrator is presented in Fig. 4.

Table 1 Coordinates of designed parabola.

X (cm)	-140.0	-116.6	-93.33	-70.00	-46.67	-23.33	0.0
Y (cm)	35	24.31	15.56	8.75	3.89	0.97	0.0
X (cm)	23.33	46.67	70.00	93.33	116.67	140	-
Y (cm)	0.97	3.83	8.75	15.56	24.31	35.00	-

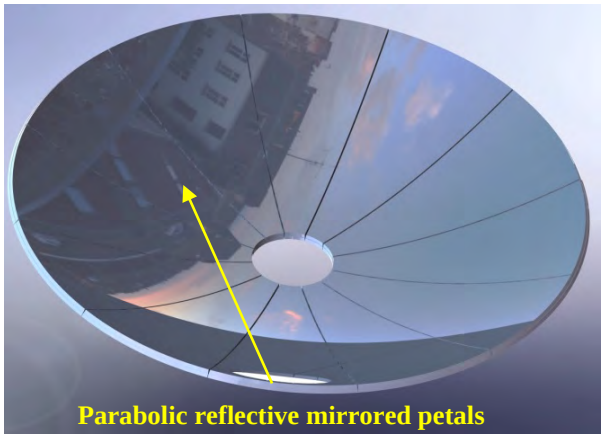

Fig. 2 Computer aided drafting model of solar parabolic dish concentrator.

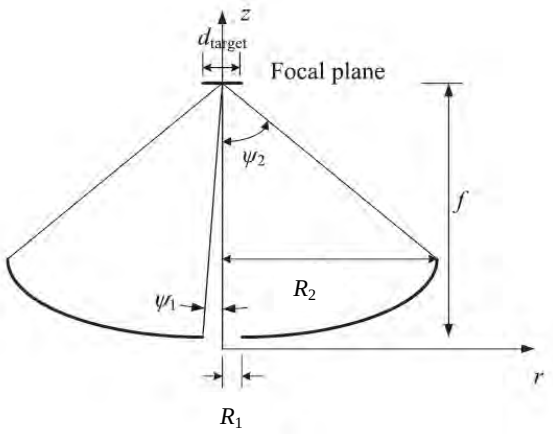

Fig. 3 Schematic of truncated parabola.

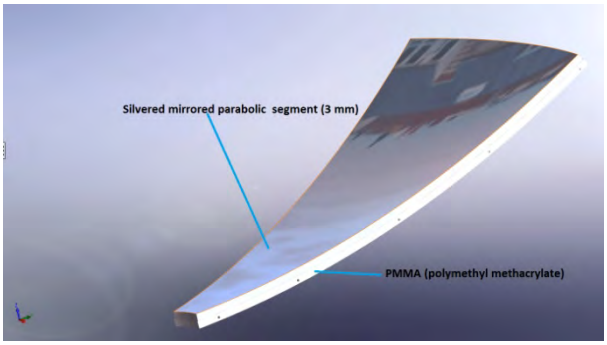

Fig. 4 Trapezoidal reflective petal of solar parabolic dish concentrator.

Detailed design parameters of solar parabolic concentrator are given in Table 2.

Receiver-absorber is placed in focal area where reflected radiation from solar concentrator is collected. In the process of designing, parabolic solar concentrators one always seek for the minimum size of the receiver. With small receiver size, one can reduce heat losses as well as cost of whole system. Also small receiver size provides increase of absorbed flux on the surface of receiver. This is the way of obtaining greater efficiency in conversion of solar radiation to heat. In our system, receiver-absorber is cylindrical disk with diameter of 24 mm. It is shown in Fig. 5. Within the solar absorber is placed spiral corrugated pipe through which water flows.

Fig. 6 shows the modified solar receiver with solar spiral corrugated pipe absorber in the next design of my investigations. This is the next solar receiver design concentrator.

In this paper, only optical properties of receiver are analysed. In our further research, we plan to model all necessary details of receiver's geometry which are important for conversion of solar energy into heat of fluid that is used for transfer energy.

3. Optical Analysis of the Solar Parabolic Dish Thermal Concentrator

For optical analysis of solar parabolic thermal concentrator software TracePro, Lamda Research Corporation, USA is used. First step was importing 3D model designed in CATIA. In TracePro, all material properties are assigned. Twelve trapezoidal reflective petals are defined as standard mirrors with reflective coating. Reflection coefficient was 95%. Receiver was cylinder with diameter 24 mm placed on 1,400 mm from vertex of parabolic dish. Absorbing surface was defined as perfect absorber. After definition of geometry of solar, parabolic concentrator radiation source was defined. Radiation source was circular with diameter same as diameter of parabolic dish (2,800 mm). Radiation source was placed 2,000 mm from vertex of parabolic dish and had circular grid pattern for generating 119,401 rays for Monte Carlo ray tracing. Spatial profile of generated rays was uniform and angular profile was solar radiation. Input parameter for optical analysis is solar irradiance 800 W/m^2. Experiential value for solar irradiation for town of Niš

Table 2 Design parameters of solar parabolic dish concentrator.

Parameters	Numerical value	Unit
Aperture radius R_2	1.4	m
Radius of smaller hole R_1	0.025	m
Ideal area of the concentrator A_{idel}	6.208	m^2
The cross section of the opening parabola A_{proj}	6.154	m^2
A sheltered area of the concentrator A_{shadow}	0.000452	m^2
The effective area of the concentrator $A_{ef} = A_{proj} - A_{shadow}$	6.1535	m^2
Receiver diameter	0.20	m
Shape of receiver	Flat circular disc	-
Depth of the concentrator	0.35	m
Focal lenght	1.4	m
ψ_1	10	°
ψ_2	45	°

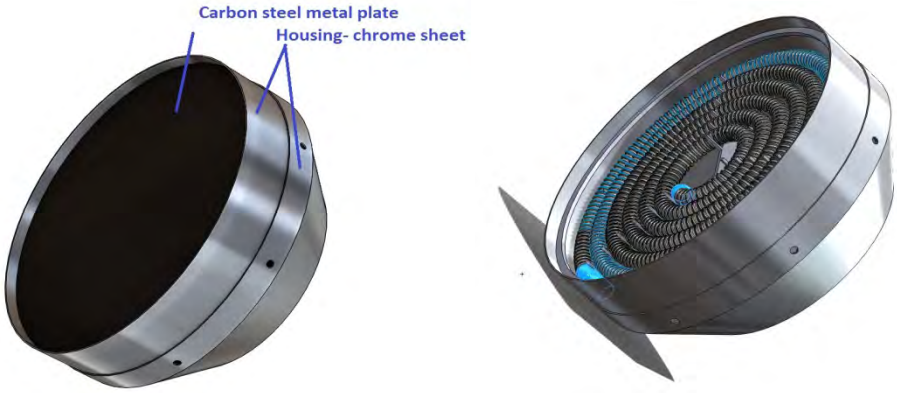

(a) (b)

Fig. 5 Solar thermal receiver—with flat plate circular disc and without (directly irradiated spiral corrugated pipe absorber).

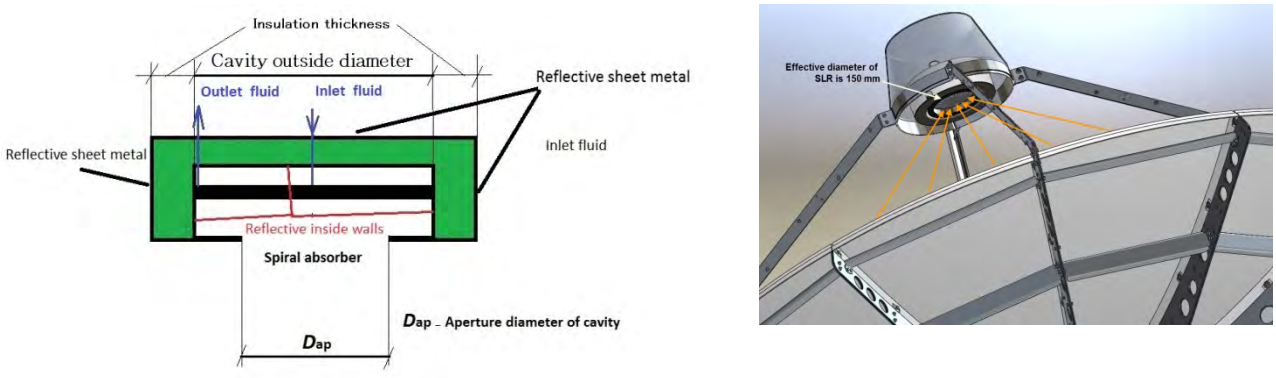

(a) (b)

Fig. 6 (a) Modified solar cavity receiver for solar parabolic dish concentrating collector and (b) concentrated solar radiation at the focus plane.

in Serbia is between 750 W/m^2 and 900 W/m^2. Optical system for solar parabolic concentrator with traced rays is given in Fig. 7. The optical concentration system consists of three objects: solar parabolic dish reflector, radiation source and receptor (solar receiver) in the focus of the parabolic dish concentrator

Optical analysis is done by generating and calculating Monte Carlo ray trace for 119,401 rays. From all emitted rays, only 103,029 rays reached absorber surface which is 82% rays of emitted rays are

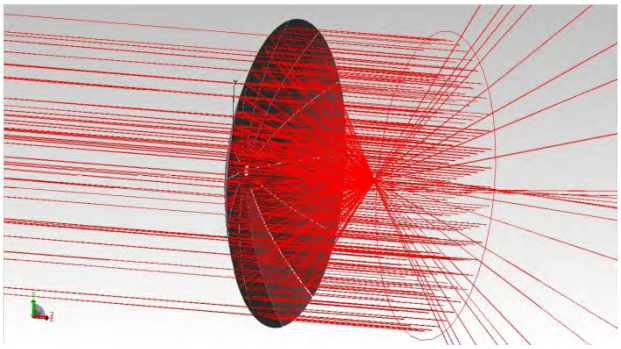

Fig. 7 Optical system of Solar parabolic concentrator with traced rays.

absorbed on receiver. Calculated irradiance for absorbed rays on receiver is from 8.66 × 10^{-6} W/m^2 to 3.45 × 10^7 W/m^2.

Total calculated flux on receiver was 4,031 W. In Fig. 8 is shown total irradiance map for absorbed flux on receiver.

From Fig. 8, one can see that, calculated values for total irradiance are in compliance with theoretically values. In the center of receiver, irradiance is from 3.45 × 10^7 W/m^2 to 2 × 10^7 W/m^2 and at the periphery of receiver irradiance is from 8 × 10^6 W/m^2 to 2 × 10^6 W/m^2.

Irradiance diagram at the center of receiver is given in Fig. 9.

From Fig. 9, one can see that, peak irradiance is in the circle with diameter 8 mm (from -4 mm to 4 mm). Very good irradiance is in the circle with diameter 16 mm. Irradiance diagram at the periphery of receiver is given in Fig. 10.

From Fig. 10, one can see that, irradiance diagram at periphery of receiver is still rather good with peak values of irradiance in the circle diameter 4 mm. Very good values of irradiance is in the circle with diameter 16 mm. From Figs. 9 and 10, one can see that, irradiance has very good values in the circle with diameter 16 mm for center and periphery and that only peak values change from center to periphery.

4. Conclusions

This paper presents optical analysis of the solar parabolic concentrator using the ray—tracing software

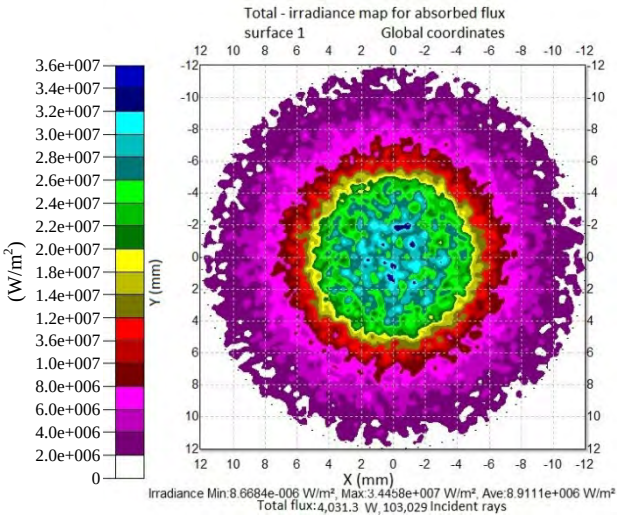

Fig. 8 Irradiance map for absorbed flux on receiver.

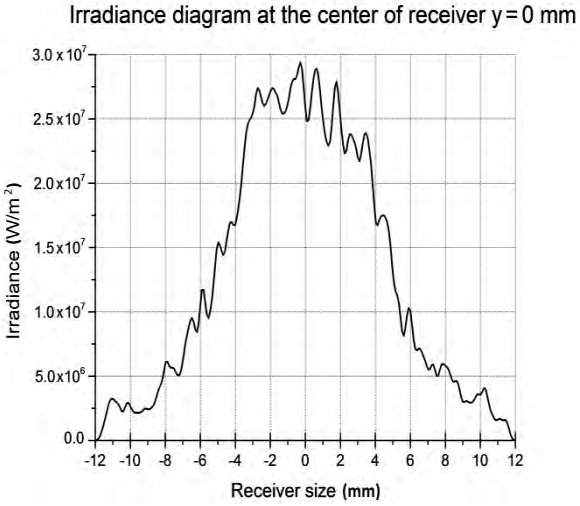

Fig. 9 Irradiance diagram at the center of receiver.

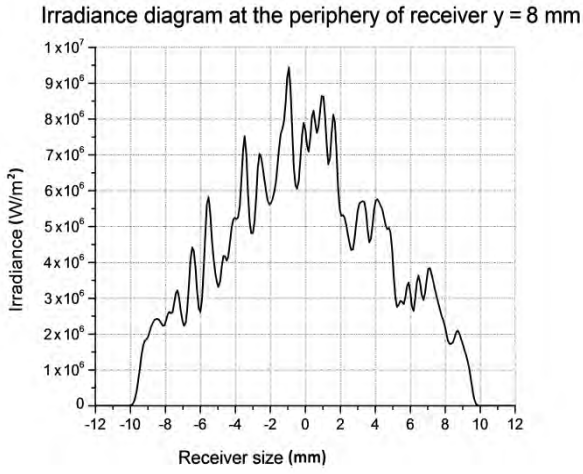

Fig. 10 Irradiance diagram at the periphery of receiver.

TracePro. One can see that, results obtained from optical design of solar parabolic concentrator are satisfactory. Total flux in focal area is good. Irradiance distribution for absorbed flux is relatively uniform for small area for absorber. As a next step, various analysis and simulations of the model are planed. Among others are variation of number of petals, size of petals and shape of petals. In future development of optimization, method is planned. This optimization method will make it possible to find optimal geometrical and optical parameters of the various types of solar parabolic dish concentrators as well as geometrical, optical and thermal parameters of receivers-absorbers.

Acknowledgments

This paper is done within the research framework of research projects: III42006—research and development of energy and environmentally highly effective polygeneration systems based on renewable energy resources and III45016—fabrication and characterization of nano-photonic functional structrues in biomedicine and informatics. Both projects are financed by Ministry of Education, Science and Technological Development of Republic of Serbia. Authors acknowledge to Lambda Research Corporation for allowing to use software TracePro for PhD thesis research of Saša Pavlović.

References

[1] Badran, A. A., and Yousef, I. A. 2010. “Portable Solar Cooker and Water Heater.” *Energy Conversion and Management* 51 (8): 1605-9.

[2] Joshi, A. S., Dincer, I., and Reddy, B. V. 2011. “Solar Hydrogen Production: A Comparative Performance Assessment.” *International Journal of Hydrogen Energy* 36 (17): 11246-57.

[3] Furler, P., Scheffe, J. R., and Steinfeld, A. 2012. “Syngas Production by Simultaneous Splitting of H_2O and CO_2 via Ceria Redox Reactions in a High-Temperature Solar Reactor.” *Energy & Environmental Science* 5 (3): 6098-103.

[4] Mancini, T., Heller, P., Butler, B., Osborn, B., Schiel, W., Goldberg, V., Buck, R., Diver, R., Andraka, C., and Moreno, J. 2003. “Dish-Stirling Systems: An over View of Development and Status.” *Journal of Solar Energy Engineering-Transactions of the ASME* 125 (2): 135-51.

[5] Mills, D. 2004. “Advances in Solar Thermal Electricity Technology.” *Solar Energy* 76 (1-3): 19-31.

[6] O’Neill, M. J., and Hudson, S. L. 1978. “Optical Analysis of Paraboloidal Solar Concentrators.” In *Proceedings of the 1978 Annual Meeting*, 855.

[7] Imhamed, M. S. A., Tadhg, S. O., Reddy, K. S., and Tapas, K. M. 2013. “An Optical Analysis of a Static 3-D Solar Concentrator.” *Solar Energy* 88 (February): 57-70.

[8] Kaushika, N. D., and Reddy, K. S. 2000. “Performance of Low Cost Solar Paraboloidal Dish Steam Generating.” *Energy Conversion & Management* 41 (7): 713-26.

[9] Ouederni, A. R. E., Ben Salah, M., Askri, F., and Aloui, F. 2009. “Experimental Study of a Parabolic Solar Concentrator.” *Revue des Renouvelables* 12 (3): 395-404.

[10] Rafeeu, Y., and AbKadir, M. Z. A. 2012. “Thermal Performance of Parabolic Concentrators under Malysian Environment: A Case Study.” *Renewable and Sustainable Energy Reviews* 16 (6): 3826-35.

[11] Zhiqiang, L., Justin, L., and Wojciech. L. 2012. “Optical Design of a Flat Solar Concentrator.” *Solar Energy* 86 (6): 1962-6.

[12] Hasnat, A., Ahmed, P., and Khan, K. A. 2011. “Numerical Analysis for the Thermal Design of a Paraboloidal Solar Concentratong Collector.” *International Journal of Natural Sciences* 1 (3): 68-74.

[13] Rebecca, D., Keith, L., Greg, B., and John, P. 2012. “An Experimental Study of Ammonia Receiver Geometries for Dish Concentrators.” *Journal of Solar Energy Engineering* 134 (4): 945-55.

[14] Glen, J., Keith, L., and Andreas, L. 2003. “Optical Performance of Spherical Reflecting Elements for Use with Paraboloidal Dish Concentrators.” *Solar Energy* 74 (2): 133-40.

Journal of Energy and Power Engineering 9 (2015) 721-726
doi: 10.17265/1934-8975/2015.08.005

The Research of Complex System Property between Thermosensitive Polymer and Surfactant

Chao Ma[1, 2], Gang Wan[1] and Tang Tang[1]

1. Province Key Laboratory of Oil and Gas Drilling and Production Engineering, College of Petroleum Engineering, Yangtze University, Wuhan 430100, China

2. The State Key Laboratory of Polymer Materials Engineering, Polymer Research Institute of Sichuan University, Chengdu 610065, China

Received: March 20, 2015 / Accepted: May 04, 2015 / Published: August 31, 2015.

Abstract: In this paper, the rigid structural thermosensitive polymer (made in lab) of NBS (N-butyl styrene), N, N-DEAM (diethyl acrylamide) and AM (acrylamide) was prepared. The influence of viscosity for copolymer solution under different reaction conditions such as temperatures and inorganic salt (monovalent salt and divalent salt) was analyzed. The experiment studies the combination of polymer situation and three different types of surfactants under certain conditions of the room temperature (25 °C) and the formation temperature (76 °C). At last, the influence of the surfactant kinds and concentration on the viscosity of the polymer solution are studied. The results show that: The copolymer solution, the apparent viscosity of which decreases with the increasement of temperature, but its viscosity has suddenly increased and thereafter dropped in the transition temperature. So the temperature sensitive effect of copolymer is very significantly. When the concentration of inorganic salt and surfactant can be controlled in certain extent, the copolymer solution, the effect increases with the increasement of the concentration, but the viscosity of which decreases with the increasement of shear rate. Shear rate can be controlled in certain extent, shearing stability properties of the copolymer solution are proved.

Key words: Butyl styrene, hydrophobic monomer, solution properties, thermosensitive polymer, surfactant.

1. Introduction

Research development of polyacrylamide flooding agent with temperature resistance and salt tolerance is adapted to high temperature and salinity formation for this stringent requirement. In recent years, polyacrylamide has been used as its backbone by domestic and international researchers, with the introduction of hydrophobic monomer, the thermal resistant and salt-tolerant monomer into polymer side chain. The thermal resistant and salt-tolerant monomer is not directly grafted onto the main chain.

It is linked by ester linkage or an ester bond. Pyrohydrolysis of ester linkage or an ester bond is very easy [1-3]. Besides, the nature of the polymer situation has mainly the property of the conventional water soluble polymer by modification. The conventional water soluble polymer solution, the apparent viscosity of which decreases with the increasement of temperature, salt concentration and shear rate. But its viscosity is high enough, shortly afterwards, it is a sharp drop. The nature of copolymer is in a difficult position to satisfy request for adapting the high temperature and salinity formation.

The special phenomenon has shown that, the viscosity of the linear poly N-alkyl acrylamide-based polymer solution increases with the increasement of temperature, salt concentration above the phase low critical solution temperature [4-9]. Its rheological properties were studied in this paper. The influence of viscosity for thermosensitive polymer solution under different reaction conditions such as temperatures and inorganic salt (a monovalent salt and divalent salt) was

Corresponding author: Chao Ma, associate professor, research fields: oil-gas chemical teaching and scientific research work. E-mail: mc19790924@126.com.

analyzed. The experiment studies the combination of polymer situation and three differential concentration of surfactants. The influence of the surfactant on the viscosity of the polymer solution was studied. It is used as polyacrylamide flooding agent with temperature resistance and salt tolerance.

2. Experiment

2.1 Equipment and Materials

Thermosensitive polymers (made in lab, code: WM-7), hydrophobically associating polymers: industrial products; Sichuan Guangya Chemical Co, Ltd; sodium chloride. Calcium chloride: analytical pure; Tianjing Fucheng Chemical Regent Factory; sodium dodecyl sulfate; sodium dodecylsulfate. Sodium dodecyl benzene sulfonate: analytical pure; Wuhan Zhongtian Chemical Co, Ltd. Stickness metre: Brookfield DV3T, engineering laboraties, Inc.

2.2 Methods

2.2.1 Temperature Sensitivity of Copolymer

Thermosensitive polymer solution (WM-7) is made up into two kinds of the different concentrations with distilled water, the concentrations of the preparations are 2,000 mg/L (low concentration) and 20,000 mg/L (high concentration). The viscosimeter uses a No. 0 rotor. When the shear rate is 6 r/min (7.34 s^{-1}), in the range of temperature (40-120 °C), it discussed the viscocity of the copolymer solution, mainly about the temperature sensitivity of thermosensitive polymer.

2.2.2 The Effect of Salt Concentration on the Apparent Viscosity of the Copolymer Solution Has Been Studied

Thermosensitive polymer solution (WM-7) is made up into some of the same concentrations with distilled water, their concentrations are 2,000 mg/L. Then add monovalent salt (3,000-100,000 mg/L NaCl) and divalent salt (100-500 mg/L $CaCl_2$) of different concentrations. The viscosimeter uses a No. 0 rotor. At the temperature of 30 °C and different shear rate, the influence of salt concentration on the viscosity of the copolymer solution is studied, the paper analyzes the inorganic salt sensitivity of thermosensitive polymer.

2.2.3 The Effect of Surfactant Concentration on the Apparent Viscosity of the Copolymer Solution Has Been Studied

Under certain conditions of the room temperature (25 °C) and the formation temperature (80 °C), thermosensitive polymer solution (WM-7) is made up into some of the same concentrations with distilled water, their concentrations are 20,000 mg/L. The viscosimeter uses a No. 0 rotor. When the shear rate is 6 r/min (7.34 s^{-1}), the influence of the surfactant kinds and concentration on the viscosity of the polymer solution are studied, including sodium dodecyl sulfate, sodium lauryl sulfonate and sodium dodecyl benzene sulfonate. We compound the surfactant with the copolymer solution, then the influence of which solution on the viscosity of the solution is studied.

3. Results and Discussions

3.1 Temperature Sensitivity of the Copolymer Solution

As you can see from Figs. 1 and 2: The apparent viscosity of thermosensitive polymer solution (2,000 mg/L) decreases with temperature increasing. In the range of temperature (76-80 °C), its viscosity has suddenly increased, the initial viscosity of the solution increases from 19 MPa·s to 39 MPa·s, its viscosity is 20 MPa·s, its phase transition temperature is between 76 °C and 80 °C. The apparent viscosity of thermosensitive polymer solution (20,000 mg/L) decreases as the temperature is increased. In the range of temperature (70-76 °C), its viscosity has increased, but the increase is not larger, its phase transition temperature is between 70 °C and 76 °C. Thus it can be seen. In the range of certain temperature, the increasement of the apparent viscosity of two solutions is a phenomenon. Thermal property of low concentration of thermosensitive polymer solution is more obvious, the viscosity increase of low concentration of thermosensitive polymer solution is larger. The viscosity increase of high concentration of

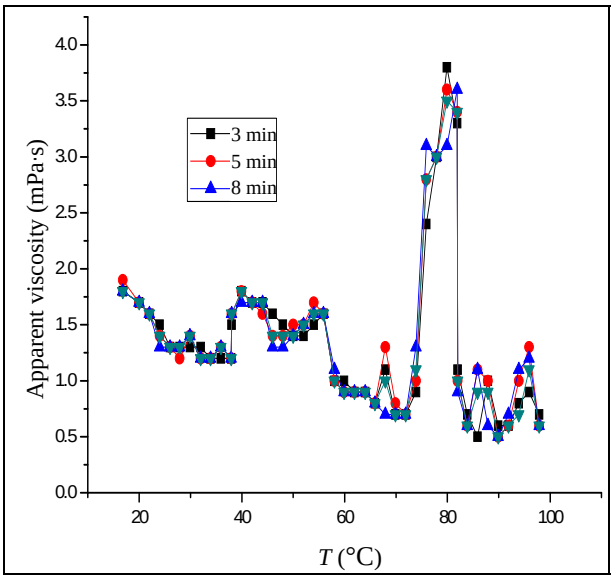

Fig. 1 Effect of temperature on the apparent viscosity of the solution (2,000 mg/L).

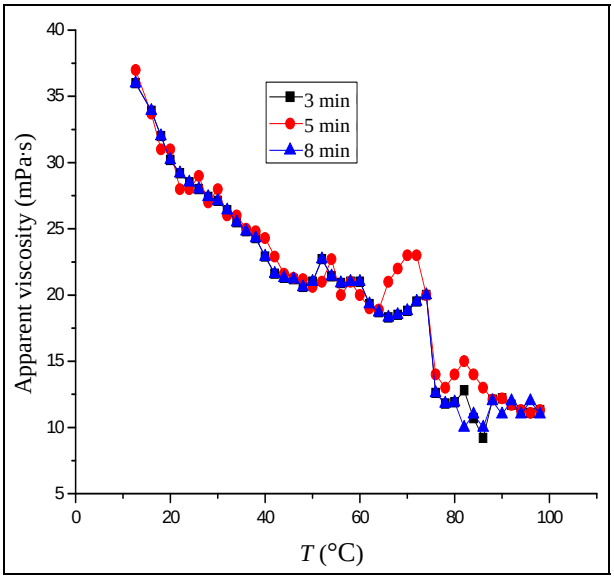

Fig. 2 Effect of temperature on the apparent viscosity of the solution (20,000 mg/L).

thermosensitive polymer solution is slight. When viscosity increases, its phase transition temperature decreases. The reason of the increase of viscosity for this lies in hydrogen bond association. A dilute solution has not enough these hydrogen bonds. When the temperature increases in certain extent, the molecules collide even intense, hydrogen bond association is created by the collision of the molecules [10]. Concentrated solution has a great many molecular chains. Part of hydrogen bonds has been associated, when the temperature increases, the molecules move faster and hydrogen bonds associate easier [11].

3.2 The Effect of Inorganic Salt on the Apparent Viscosity of the Copolymer Solution

As you can see from Fig. 3, the concentration of monovalent salt increases from 1,000 mg/L to 100,000 mg/L. Under the low shear rate (50 rpm, 100 rpm), the viscosity increase of low concentration of thermosensitive polymer solution is slight. Under the high shear rate (150 rpm, 200 rpm, 250 rpm), the viscosity increase of high concentration of thermosensitive polymer solution is larger. As you can see from Fig. 4, at a low or high shear rate, the viscosity of copolymer solution increases with the concentration increases of $CaCl_2$ concentration. The viscosity of the copolymer solution increases with the increasement of the experimental shear rate. On the whole, the viscosity of the thermosensitive polymer increases in high salt condition. Conventional polyacrylamide solution has not the particularities of the thermosensitive polymer. Thus, the viscosity of the thermosensitive polymer increases in high salt condition.

3.3 The Effect of Surfactant Concentration on the Apparent Viscosity of the Polymer Solution

As you can see from Fig. 5, at the temperature of 25 °C, the copolymer solution, the apparent viscosity of which decreases with the increasement of surfactant concentration, but its viscosity has slowly increased. The apparent viscosity reaches a maximum and then drops down. Because of three kinds of the surfactants as anionic surfactants have been widely applied in the field of flooding agent. The hydrophobic group of anionic surfactant interact with the hydrophobic group of the copolymer solution to provide a linkage point of hydrophobic association [12]. Thus the viscosity of copolymer solution increases. The anionic surfactant is negatively charged, what increase the negatively charged group of molecular chains by hydrolysis. Electrostaic repulsion is formed by the interaction, which led to the viscosity increases.

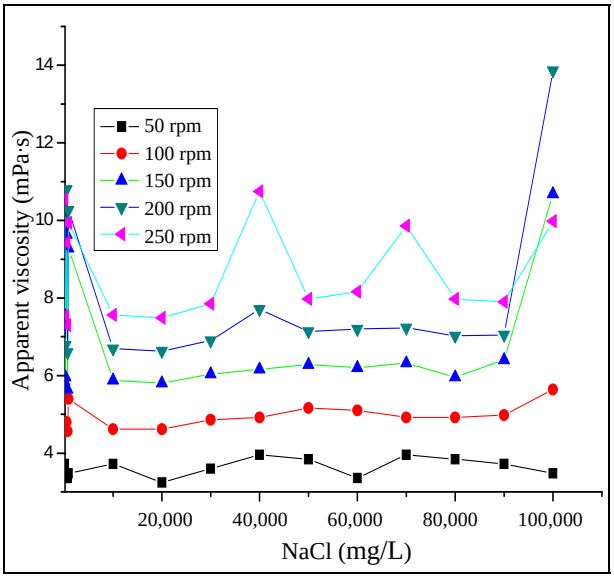

Fig. 3 Effect of NaCl concentration on the apparent viscosity of the solution (2,000 mg/L).

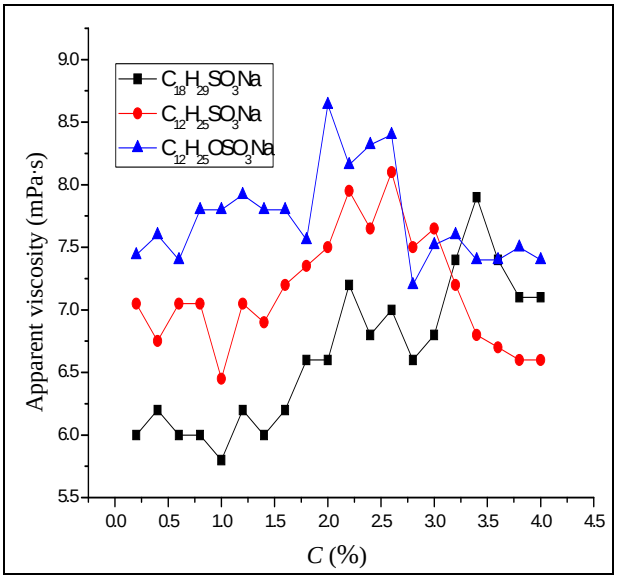

Fig. 5 Effect of surfactant on the apparent viscosity of the solution (25 °C).

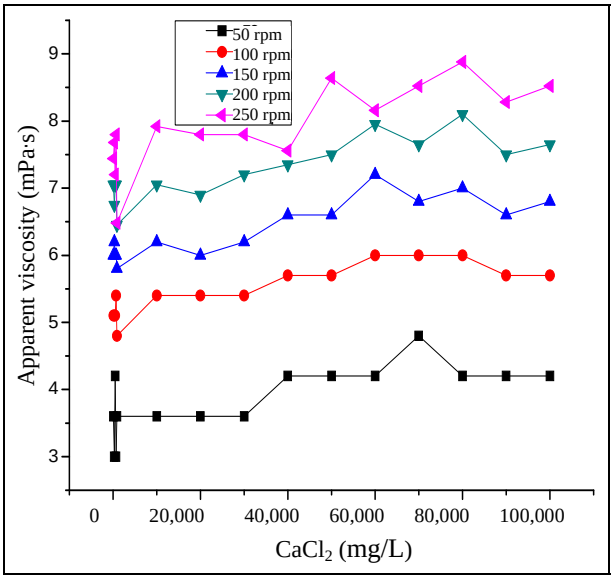

Fig. 4 Effect of $CaCl_2$ concentration on the apparent viscosity of the solution (20,000 mg/L).

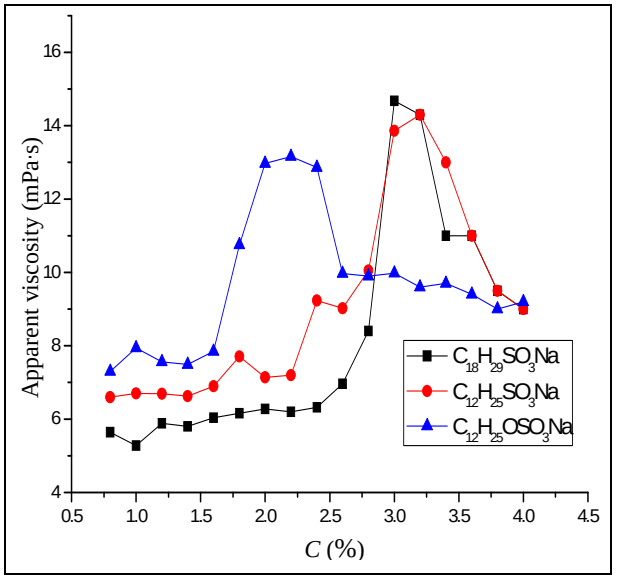

Fig. 6 Effect of surfactant on the apparent viscosity of the solution (76 °C).

The solution begins to form a large number of micelles when the surfactant concentration continues to increase. Hydrophobic groups are wrapped in micelles. Because of associating partial hydrophobic groups decrease, the associating interaction of hydrophobic groups weaken, and the link between the molecules is destroyed [13]. The crosslinking network structure and the viscosity of the solution have suddenly increased. When the concentration of surfactants are the same, the influence sequence of surfactants on the apparent viscosity of the solution is sodium dodecyl sulfate > sodium lauryl sulfonate > sodium dodecyl benzene sulfonate, the viscosity of the copolymer solution is related with the structure of the surfactant. As you can see from Fig. 6, the solution viscosity in the low temperature (25 °C) and the high temperature (76 °C) have similar rules. Apparent viscosity increases more evident with the increment of the low temperature. It is mainly because raising the temperature can enhance the association.

4. Conclusions

At a low or high shear rate, the viscosity of copolymer solution increases. The viscosity of the copolymer solution increases with the increasement of the experimental shear rate. On the whole, the viscosity of the thermosensitive polymer increases in high salt condition.

The apparent viscosity of thermosensitive polymer solution decreases with shear rate increasing. In the range of the shear rate (10-30 s^{-1}), its viscosity has a sharp drop. It has the character of shear thinning. When the shear rate is 40 s^{-1}, the viscosity of the copolymer decrease is not larger, which remains generally stable. In the formation of a shear, rate is 100-170 s^{-1}. Thermosensitive polymer has a good shearing resistant capability.

At the temperature of 30 °C, the copolymer solution, the apparent viscosity of which decreases with the increasement of surfactant concentration, but its viscosity has slowly increase. The apparent viscosity reaches a maximum and then drops down. When the concentration of surfactants are the same, the influence sequence of surfactants on the apparent viscosity of the solution is sodium dodecyl sulfate > sodium lauryl sulfonate > sodium dodecyl benzene sulfonate, the viscosity of the copolymer solution is related with the structure of the surfactant. The solution viscosity in the low temperature (25 °C) and the high temperature (76 °C) have similar rules. Apparent viscosity increases more evident with the increment of the low temperature.

Acknowledgments

Supported by the Natural Science Foundation of China, salt/thermo induces synthesizing polymer and thickening of the solution with the rigid hydrophobic group (No. 51404036).

Supported by PetroChina Innovation Foundation, temperature/salt sensitivity of the copolymer solution and thermo induce synthesizing the thermal resistant and salt-tolerant polymer (No. 2013D-5006-0207).

References

[1] Fevola, M. J., Bridges, J. K., Kellum, M. G., Hester, R. D., and McCormick, C. L. 2004. “pH-Responsive Polyzwitterions: Acomparative Study of Acrylamide-Based Polyampholyte Terpolymers and Polybetaine Copolymers.” *Journal of Applied Polymer Science* 94 (1): 24-39.

[2] Xiangjun, L., Kun, L., Shaohua, G., Zhongbin, Y., Lixi, L., and Jing, H. 2013. “Synthesis and Evaluation of Temperature-Resistance and Salt-Tolerant Copolymer (AM-AMPS-DMDAAC-NEA) as Clay Stabilizer.” *Chemical Research and Application* 25 (6): 857-61.

[3] Gao, B. Y., Guo, H. P., Wang, J., and Zhang, Y. 2008. “Preparation of Hydrophobic Association Polyacrylamide in a New Micellar Copolymerization System and Its Hydrophobically Associative Property.” *Macromolecules* 41 (8): 2890-7.

[4] Yang, X. W., Shen, Y. D., and Li, P. Z. 2010. “Intrinsic Viscosity, Surface Activity, and Flocculation of Cationic Polyacrylamide Modified with Fluorinated Acrylate.” *Polym Bull* 65 (2): 111-22.

[5] Wensheng, C., Qingquan, Z., and Xi, X. 1996. “A Study on Synthesis and Properties of AM-DEAM-AA Copolymer.” *Polymer Materials Science and Engineering* 12 (5): 47-52.

[6] Xiaofei, Z., Li, Z., Li, Z., Xi, Z., and Hua, D. 2007. “Study on the Aqueous Solution Properties of Temperature-Sensitive Water-Soluble Polymer P(NIPAM-HEMA-AM) and P(NIPAM-HEMA-AM-AA).” *Polymer Materials Science & Engineering* 23 (3): 85-91.

[7] Huahua, M., Yinyan, G., Zaiqian, S., Shuhua, S., and Xiao, C. 2008. “Thermo-Sensitivity of N-Isopropylacrylamide Copolymers Containing Hydrophobic Units.” *Journal of Functional Polymers* 21 (4): 432- 6.

[8] Jinqiang, L., Fang, Z., Jianzhong, S., Yongqiang, L., and Qinguo, F. 2009. “Preparation of PNIPAm Grafited Cotton and Its Thermal Sensitivity.” *Acta Polymerica Sinica* 9 (12): 1226-72.

[9] Yanyun, C., and Zhiyi, Z. 2010. “Preparation and Properties of Linear PNIPAM.” *Insulating Materials* 43 (3): 24-8.

[10] Mingzhu, Y., Guangsu, H., and Yong, Z. 2010. “Property Study on Novel Thermo-Sensitive Polyacrylamide Derivatives.” *China Plastics Industry* 40 (4): 35-8.

[11] Xiaofei, Z. 2007. “Study on the Synthesis and Properties

of Thermo-Sensitive Water-Soluble Polymer Based on 3-Isopropenyl-a,a-Dimethylbenzyl Urethane." Master thesis, Polymer Research Institute of Sichuan University.

[12] Huanxia, W., Shouxin, L., Yu, F., Xiaoyu, H., and Feng, Z. 2006. "Study on the Synthesis and Properties of Temperature-Sensitive N-Isopropylacrylamide Copolymer." Master thesis, Polymer Research Institute of Sichuan University.

[13] Huanxia, W., Shouxin, L., Yu, F., Xiaoyu, H., and Sa, Z. 2009. "Synthesis of Poly (N,N-Diethylacrylamide) and the Effect of Salts on the Thermosensitivity of Its Aqueous Solutions." *Acta Physico-Chimica Sinica* 25 (9): 1911-5.

Journal of Energy and Power Engineering 9 (2015) 727-730
doi: 10.17265/1934-8975/2015.08.006

Use of Fractals Channels to Improve a Proton Exchange Membrane Fuel Cell Performance

Pablo Martin Belchor[1, 2], Paloma Barbieri[2], Gabriel Benetti[2], Evandro Mathias[2], Mayra Klein[2], João Bottin[2], Deyse Suman Carpenter[3] and Maria Madalena Camargo Forte[1]

1. Department of Materials, School of Engineering, UFRGS (Federal University of Rio Grande doSul)/PPG3M (Postgraduate Program in Mining, Metallurgy and Materials), Porto Alegre 91501-970, Brazil

2. Exact and Technological Sciences, UNOESC (University of Oeste de Santa Catarina), Campus II, Joaçaba 89600-000, Brazil

3. Department of Materials, the FURB (Foundation Regional University of Blumenau), Campus II, Blumenau 89030-000, Brazil

Received: April 27, 2015 / Accepted: June 11, 2015 / Published: August 31, 2015.

Abstract: One of the most important and effective hardware elements for improvement of efficiency and power density of proton exchange membrane fuel cells is the flow field plate. The design and the pattern of the flow field plate have a considerable effect on the effectiveness of mass transport as well as on the electrochemical reactions inside the cell. The configuration of the flow field plate aims at ensuring a low pressure-drop over all channels in the stack. In this work, a FPFFP (fractal parallel flow field plate), with bio-inspired configuration by insertion of fractals in a classic PFFP (parallel flow field plate), is proposed, increasing the flow area of the hydrogen at anode side without increasing the section's area of the flow field plate. By simulating was observed that, the use of channels in fractal shape can increase the hydrogen flow area without occuring pressure loss in the cell. The fluid dynamic behavior in the FPFFP at smaller scales was replicated in the same plate, with better advantage of the active area of the electrode. Increasing the hydrogen flow area without causing pressure loss could be a good tactic to increase the power density of fuel cells, and consequently improving the cell performance.

Key words: Fuel cells, flow field design, fractals, power, simulation.

1. Introduction

The main driving force for the fuel cell research, development and commercialization is due the global concern with the pollutant emissions, especially from the transport and industries sectors [1, 2]. Fuel cells, in particular the PEMFC (proton exchange membrane fuel cell) are lately extensively being studied due to its potential as alternate source for energy generation for mobile applications, mainly in the transport sector [3-5]. Fuel cells have technological unique attributes such as high-energy efficiency, low or no emissions of pollutants and absence of moving parts [3].

A hydrogen fuel cell is an electrochemical device that converts chemical energy stored by hydrogen fuel into electricity. The heart of a PEM (proton exchange membrane) fuel cell is the MEA (membrane electrode assembly), which includes the membrane, the catalyst layers and GDLs (gas diffusion layers). The catalytic reaction of hydrogen with oxygen from air, used as oxidant, produces more electricity per fuel mass than any other non-nuclear method of power production [4]. The most important hardware components and effective for improvement of efficiency and power density in a PEMFC are the bipolar plates. The surfaces of the plates contain a flow field, which is a set of channels to direct the hydrogen to the anode, and the oxygen to the cathode on the MEA. The bipolar plates are used to assemble individual PEM fuel cells into a fuel cell stack, collect the electronic current and remove generated water [5]. The design of the flow field plate and its pattern have great effect on the effectiveness of

Corresponding author: Pablo Martin Belchor, professor, research fields: modelling and simulation, and fuel cell system. E-mail: rafrstv@hotmail.com.

mass transport as well as electrochemical reactions inside the cell. The channels' design (dimension, shape, pattern and configuration) is very important for better bipolar plate. One of the goals of the flow field plate configuration is to ensure a low pressure drop over all the channels in all the stack cells [6].

Types of channel configurations with fractal branching patterns occurs in nature, found in crystals formation, landscapes shaped by water drainage, lightning bolts, in certain plants and in the human body. Fig. 1 [7] shows some examples of fractal anatomical systems. Fractals are not just stunning visual effects, but inspiration source to model more complex patterns [8]. More generally, building something is typically flat, round or follows other shapes of very simple geometry. By contrast, shapes found in nature as ones in the mountains, clouds, broken stones and trees are highly complex [9].

In this work, a FPFFP (fractal parallel flow field plate), with bio-inspired configuration in fractals, and a classical PFFP (parallel flow field plate), the most popular plate, were comparatively modeled and evaluated by computer simulation.

2. Objectives

The aim of this work is to propose a plate with a bio-inspired flow field configuration to improve the flow area of the hydrogen at anode side of the MEA, with no pressure loss in the channels of the plate.

3. Methodology

3.1 Designing the FPFFP

An exploded view of a fuel cell stack in Fig. 2 shows one side bipolar plate with flow field used as pattern, facing the gas diffusion layer, used in both side of MEA. The classic and fractal parallel flow field were designed using SolidWorks software.

Fig. 3 shows SolidWorks images of the modeled structures, the new FPFFP and classic PFFP, for using CFD (computational fluid dynamics) to study the dynamic behavior of continuous fluid. The structures

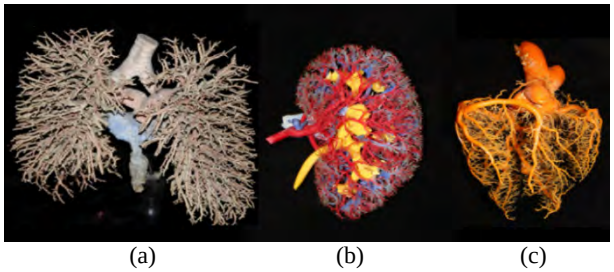

(a) (b) (c)

Fig. 1 Examples of "tree-like" fractal anatomic systems (from left to right: (a) bronchial tree; (b) renal vascular and urinary systems; (c) heart coronary system).

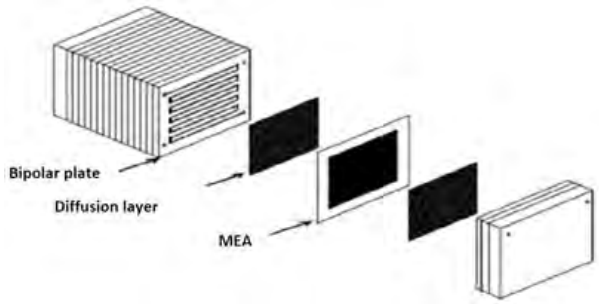

Fig. 2 Exploded view of a PEMFC stack.

of the channels were characterized by repeating a self-similarity at different size scales inspired in a biological branching pattern [10]. To insert various fractals channels in the classic PFFP was created connections between every channels of the flow field. Each new channel attached successively of smaller size maintaining the same similarity increases considerably the active surface area of the flow field.

3.2 Simulation Tests Using CFD

The tests were performed using SolidWorks software 2013 with flow simulation tool, and a computer Alienware Aurora Desktop BRH3171 equipped with Intel® Core™ i7-960 (3.2 GHz, 8 MB L3 cache; 24 GB DDR3 1,333 MHz memory/6 × 4 GB) and an liquid cooler high-performance (Alienware®). The tests performed for each CFD using the plates classical PFFP and the fractals have ranged from a few minutes to over 3 h, respectively.

In the simulation tests, the temperature of both flow field plates was controlled at 100 °C. At the cell anode side, in channel inlet, the hydrogen flow at 25 °C was of 1 L/min, and in the channel outlet, the hydrogen

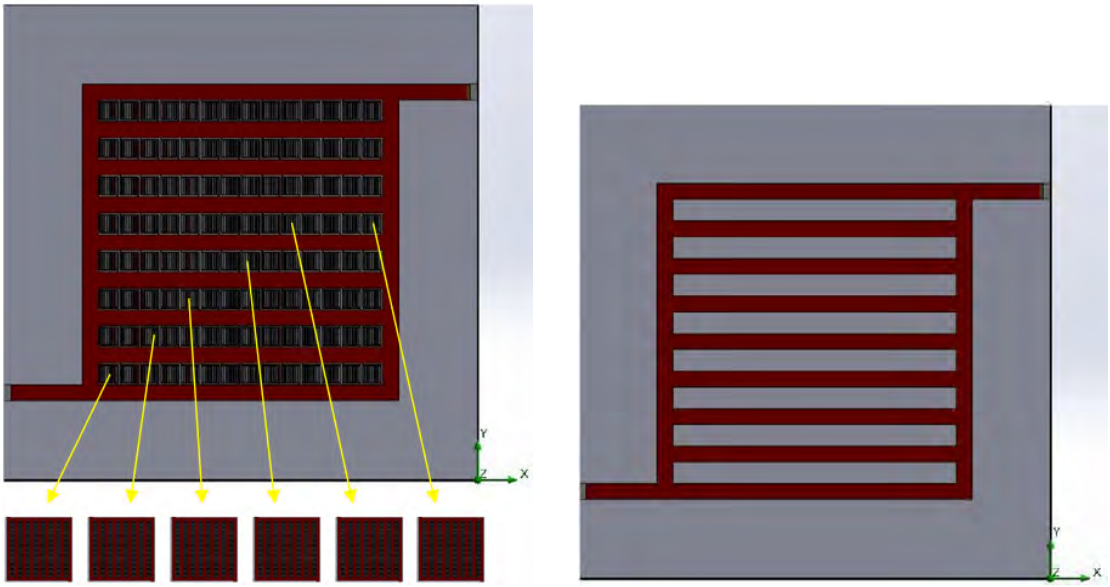

(a) (b)

Fig. 3 SolidWorks images of (a) FPFFP; (b) PFFP.

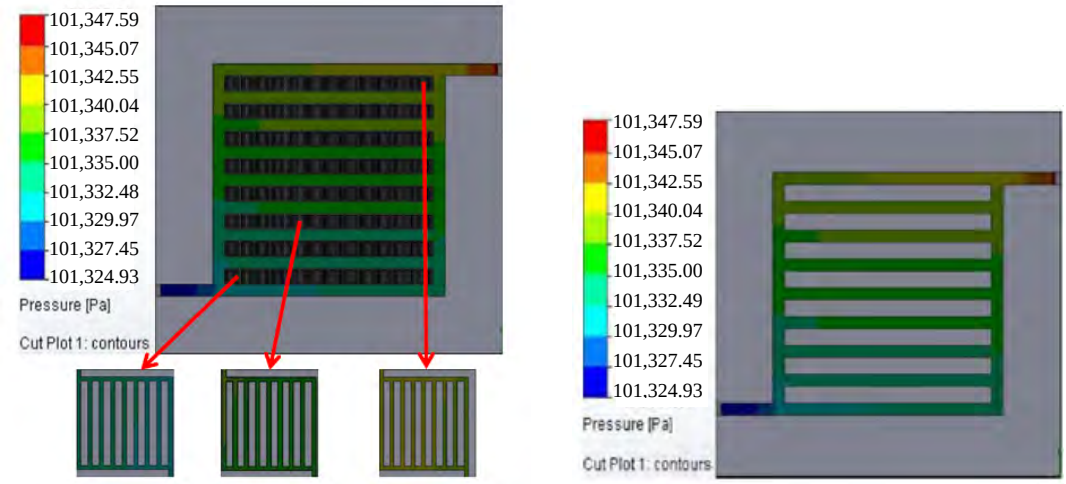

(a) (b)

Fig. 4 Figured images of the CFD simulation with the (a) FPFFP and (b) PFFP.

pressure was equal environmental-pressure.

4. Results and Discussion

Figured images of the CFD simulation using FPFFP and the PFFP are shown in Fig. 4. The fluid dynamic test results had shown pressure variation in the hydrogen flow similar for both FPFFP and PFFP. The hydrogen pressure decreased as the reagent approaches the flow field outlet. In the fractals channels of the FPFFP, the fluid dynamic behavior of the hydrogen has been repeated at smaller scales in the same plate. In both flow field plates, the minimum pressure was of 101,324.93 Pa, and the maximum pressure of 101,347.59 Pa, occurring pressure-loss of 22.66 Pa. Although the pressure loss has been equal in both kind of flow field channel, the hydrogen flow occurred in a larger volume in the channels with fractals.

Tables 1 and 2 show the parameters minimum and maximum values, respectively, for the FPFFP and PFFP flow field channels.

Table 1 Min/max parameters of the FPFFP CFD.

	Minimum	Maximum
Pressure (Pa)	101,324.93	101,347.59
Temperature (K)	298.15	373.15
Density (kg/m^3)	0.07	0.08
Velocity (m/s)	0	10.739
Temperature (fluid) (K)	298.15	373.15
Mach number	0	7.32e-003
Vorticity (1/s)	0	51,040.651
Shear stress (Pa)	0	1.62
Heat transfer coefficient (W/(m^2·K))	7.284e-014	2,367.446
Surface heat flux (W/m^2)	-56.488	188,677.647
Heat flux (W/m^2)	0	146,972.979

Table 2 Min/max parameters of the PFFP CFD.

Name	Minimum	Maximum
Pressure (Pa)	101,324.93	101,347.59
Temperature (K)	298.15	373.15
Density (kg/m^3)	0.07	0.08
Velocity (m/s)	0	10.739
Temperature (fluid) (K)	298.15	373.15
Mach number	0	7.32e-003
Vorticity (1/s)	2.198	51,038.952
Shear stress (Pa)	1.83e-005	1.62
Heat transfer coefficient (W/(m^2·K))	7.405e-013	2,367.448
Surface heat flux (W/m^2)	-0.234	188,678.372
Heat flux (W/m^2)	0	146,974.586

4. Conclusions

The results showed that, in the anode of a PEMFC equipped with PFFP, fractals could increase the anode hydrogen flow area without increase the pressure loss and repeat the PFFP fluid dynamic behavior at smaller scales in the same plate. As a result, the MEA active area was bigger, improving the current density and consequently the fuel cell power density.

Acknowledgments

The Agencies CAPES (Coordenação de Aperfeiçoamento de Pessoal de Nível Superior) and CNPq (Conselho Nacional de Desenvolvimento Científico e Tecnológico) are gratefully acknowledged. Pablo Martin Belchor thanks to the University UNOESC (University of Oeste de Santa Catarina) and UFRGS (Federal University of Rio Grande do Sul), and the companies Werjen Equipamentos, Future (Science and Technology) and Baterias Pioneiro for their financial support.

References

[1] Pierre, J. S., and Wilkinson, D. P. 2001. "Efficient and Cleaner Power Sorce." *AlChe Journal* 47 (7): 1482-6.

[2] Trimm, D. L., and Önsan, Z. I. 2001. "On-Board Fuel Conversion for Hydrogen Fuel Cell Driven Vehicles." *Catalysis Reviews-Science and Engineering* 43 (1-2): 31-84.

[3] Falcão, D. S., Gomes, P. J., Oliveira, V. B., Pinho, C., and Pinto, A. M. F. R. 2011. "1D and 3D Numerical Simulations in PEM Fuel Cells." *International Journal of Hydrogen Energy* 36 (19): 12486-98.

[4] Tseng, C. J., Tsai, B. T., Liu, Z. S., Cheng, T. C., and Chang, W. C. 2012. "A PEM Fuel Cell with Metal Foam as Flow Distributor." *Energy Conversion and Management* 62 (October): 14-21.

[5] Roshandel, R., Arbabi, F., and Karimi, M. G. 2012. "Simulation of an Innovative Flow-Field Design Based on a Bio Inspired Pattern for PEM Fuel Cells." *Renewable Energy* 41 (May): 86-95.

[6] Wang, J., and Wang, H. 2012. "Discrete Approach for Flow Field Design of Parallel Channel Configurations in Fuel Cells." *International Journal of Hydrogen Energy* 37 (14): 10881-97.

[7] Mandelbrot, B. 1983. *The Fractal Geometry of Nature.* New York: W. H. Freeman and Company, 113.

[8] Stewart, I. 2010. *The Colours of Infinity.* New York: Springer, 2-23.

[9] Mandelbrot, B. 2010. *The Colours of Infinity.* New York: Springer, 38-57.

[10] Arvay, A., French, J., Wang, J. C., Peng, X. H., and Kannan, A. M. 2013. "Nature Inspired Flow Field Designs for Proton Exchange Membrane Fuel Cell." *International Journal of Hydrogen Energy* 38 (9): 3717-26.

Journal of Energy and Power Engineering 9 (2015) 731-740
doi: 10.17265/1934-8975/2015.08.007

Impact Analysis of EV Charging with Mixed Control Strategy

Di Wu[1], Haibo Zeng[2] and Benoit Boulet[1]

1. Department of Electric and Computer Engineering, McGill University, Montreal, QC H3A 0G4, Canada

2. Department of Electric and Computer Engineering, Virginia Tech, Blacksburg, VA 24061, USA

Received: May 20, 2015 / Accepted: June 15, 2015 / Published: August 31, 2015.

Abstract: EVs (electric vehicles) have been widely accepted as a promising solution for reducing oil consumption, air pollution and greenhouse gas emission. The number of EVs is growing very fast over the years. However, the high adoption of EVs will impose a burden on the power system, especially for neighborhood level network. In this paper, we propose a mixed control framework for EV charging scheduling to mitigate its impact on the power network. A metric for modeling customer's satisfaction is also proposed to compare the user satisfaction for different algorithms. The impacts of the proposed algorithms on EV charging cost, EV penetration and peak power reduction are evaluated with real data for a neighborhood level network. The simulation results demonstrate the effectiveness of the proposed algorithms.

Key words: Neighborhood level network, electric vehicle, penetration level, mixed control, charging management, user satisfaction.

1. Introduction

With the growing concerns on environmental protection and energy security, more and more countries and regions are promoting the usages of electric vehicles. EV (electric vehicle) is globally treated as a promising alternative to conventional vehicles to reduce greenhouse gas emission, and is expected to see a fast development in the near future [1]. This growing trend of transportation electrification has been reported in a few works [2, 3]. For example, it is estimated that, 23% of all the vehicles will have an alternative powertrain in 2020 [3].

On the other hand, the high adoption of EVs will also impose great challenges on the power system. EV charging power consumption is estimated to be comparable to typical base load for neighborhood level customers [4]. If the EV charging is left uncontrolled, the peak power consumption will be greatly increased, which accelerates the grid ageing. This issue has drawn attention in the research community [5-8]. It will be even worse for neighborhood level networks, where EV adopters often charge at similar times imposing clustering load to the network [9, 10].

EV charging can be treated as a kind of flexible load consumption [11], as we only need to get the EVs charged with enough energy before the departure time. Several control strategies have been proposed for EV charging scheduling. There are mainly two groups of control strategies: centralized control and decentralized control strategies [12]. For the centralized control strategies, usually there is a central controller which can access all information and control all the charge decisions for all the EVs. In Ref. [8], the authors propose a centralized EV charging control method which can help minimize the total charging cost while considering the negative impacts on the grid network. In Ref. [13], charging fairness for customers is discussed in a centralized control framework.

Centralized control could make full use of the

Corresponding author: Di Wu, Ph.D. student, research fields: stochastic optimization and optimal scheduling. E-mail: di.wu5@mail.mcgill.ca.

charging flexibilities of all the EVs to reduce the charging cost and mitigate the adverse effects on power system. However, there will be a heavy communication burden for the centralized control strategies. Besides, the owner of the EV may not necessarily be willing to give up the control to the central controller, partly due to privacy issues. Because of these concerns, not all the people adopt the centralized control strategy [14]. To overcome these shortcomings, Refs. [15-20] discuss the decentralized control strategies for EV charging which only require no or little information exchange between electric vehicles and the system controller. In Ref. [15], the charging price is used as a signal to realize the decentralized control for EVs. In Ref. [20], the authors proposed a decentralized control strategy with genetic algorithm.

Centralized control would be easier to get the global optimum as it can control the charging for all the EVs. However, decentralized control could provide the customers with more flexibility. For some specific neighborhood level networks, it could be possible that, only some of the customers are willing to accept the centralized control. To address this problem, we propose a mixed EV charging control framework which can recognize the need of decentralized control while maximizing the benefit of centralized control for both the grid companies and the customers.

Within the proposed control framework, the system operator is responsible for the charging control and price signal design. We consider two types of customers in the neighborhood level network. For the customers who are willing to give out the charging control, the charging for these EVs will be controlled by system controller. For those customers who are not willing to give out the charging control, the charging for these EVs will be influenced by time-of-use price signal. To describe the user satisfaction, a new user satisfaction model is proposed. The impacts of the proposed mixed control algorithm on the charging cost, EV penetration, and peak power reduction will be studied with simulation using real data.

The organization of this paper is organized as follows: In Section 2, the system models are described; in Section 3, the proposed mixed control framework is presented; in Section 4, the simulation results are presented with real data for a neighborhood level network; finally, the paper is concluded in Section 5.

2. System Models

In this Section, we describe the proposed charging control framework, including the models for EV customers, base load power consumption, electric vehicle charging power consumption and user satisfaction.

2.1 EV Customers and Base Load Power Consumption

Fig. 1 shows the prototype for neighborhood level network. In the neighborhood level network, there could be one or more EVs in every home. We consider that, there are two groups of customers for a given neighborhood level network: contractual and non-contractual customers. The contractual customers would like to sign the contract with the utility companies and give out the charging control of their EVs. The other group of customers would prefer to having the charging freedom and are unwilling to give out the charging control.

For the neighborhood level network integrated with EVs, we classify the power consumptions into two categories: base load power consumption and EV charging power consumption. The base load power consumption includes all the other power consumptions except the EV charging power consumption, for

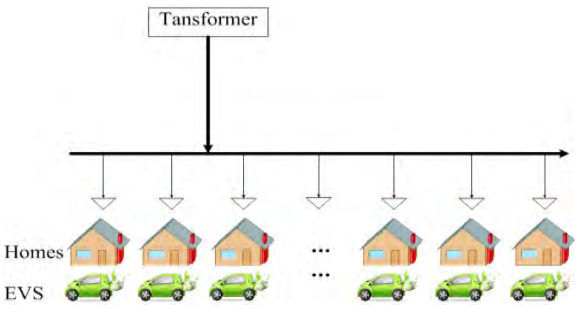

Fig. 1 Neighborhood network integrated with EVs.

example, heating, cooling, lighting and other facility power consumptions. The base load power consumptions of a neighborhood level network with seven homes for two representative days, one in summer and the other in winter, are demonstrated in Fig. 2.

In Fig. 2, it can be seen that, the peak hours are usually around noon in summer (due to the need for cooling) and the evening in winter (for heating). For uncontrolled charging, people would start charging their EVs when they arrive home in the evening, which may overlap with the base load consumption peak hours. This will further increase the peak power consumption and accelerate the grid ageing.

Fig. 3 shows the total power for the neighborhood level network integrated with four electric vehicles. In Fig. 3, the line "total load 1" represents the total power consumption of the network integrated with four Honda Fit EVs, and the line "total load 2" gives the total power consumption integrated with four Tesla Model S EVs. These EVs are assumed to be charged continuously with their rated charging power. From Fig. 3, it is clear that, even for the network integrated with four EVs (a penetration level of 4/7), the total power consumption will be very close to the power limit for the neighborhood level network.

2.2 Electric Vehicle Charging Load

In this paper, we consider two kinds of EVs: Honda Fit EV and Tesla Model S EV. The specifications for these EVs are listed in Table 1 [21, 22]. Honda Fit is relatively economic and can get fully charged around 3 h with its maximum charging power. Tesla Model S has a much larger battery pack, and can get fully charged in about 6 h. We consider continuous charging, which means that the EVs can be charged with any power from zero to maximal rated charging power.

We use the survey results conducted in City of Ottawa [23] to study the customers' driving behaviors. The results are described in Fig. 4, Tables 2 and 3.

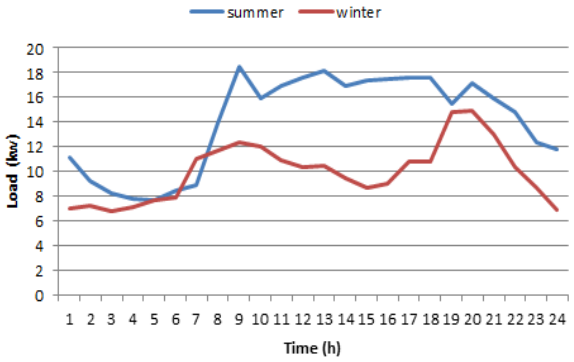

Fig. 2 Base load consumption for a neighborhood network with seven homes in two representative days.

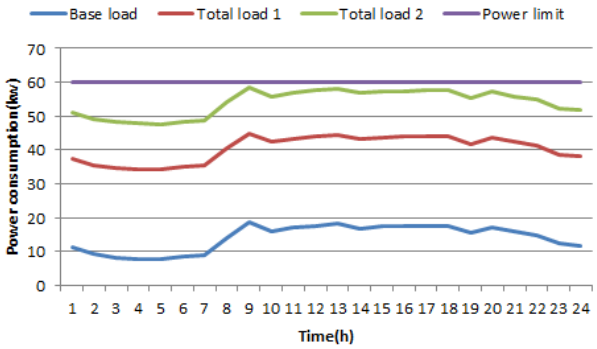

Fig. 3 Total power consumption for the network.

Table 1 EV specification.

Model	Battery capacity (kWh)	Rated charging power (kW)
Tesla Model S EV	60	10
Honda Fit EV	20	6.6

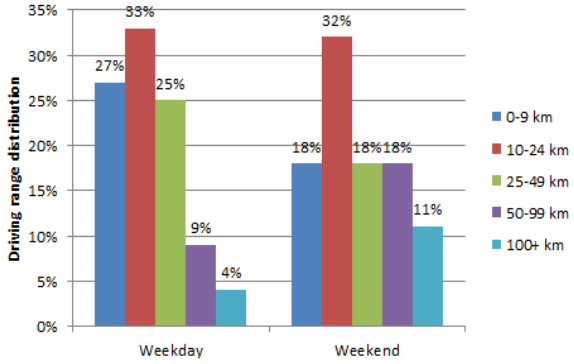

Fig. 4 Driving range distributions.

Fig. 4 demonstrates the customers driving range distributions. We can see that most people will commute within 50 km. There will be a higher probability for longer range driving in the weekend.

Table 2 Customers' departure time distribution.

Hours	< 7 a.m.	7 a.m.-9 a.m.	9 a.m.-12 p.m.	> 12 p.m.
Percentage (%)	18	70	3	5

Table 3 Customers' arrival time distribution.

Hours	< 12 p.m.	12 p.m.-2 p.m.	2 p.m.-5 p.m.	5 p.m.-7 p.m.	7 p.m.-9 p.m.	> 9 p.m.
Percentage (%)	3	2	31	53	7	2

This is probably for shopping and pleasant during the weekend. The departure and arrival time for the EV owners are shown in Tables 2 and 3, respectively. Seventy percent of all the drivers will leave home between 7 a.m. and 9 a.m. More than half of the people will arrive between 5 p.m. and 7 p.m.

For charging pricing, some utility companies adopt the TOU (time-of-use) electricity pricing structure to encourage customers to shift their power consumption to valley hours. In this pricing structure, the electricity price will be high for the peak hours of power consumption and low for valley hours. We also utilize the TOU pricing structure in our control framework.

2.3 Customer Satisfaction Model

Most of previous papers discuss the EV charging control strategies to minimize the aggregated charging cost or mitigate the negative impacts on power system, with little work discussing the user satisfactions. In order to compare user satisfaction for different charging control algorithms, we propose a new user satisfaction model. We observe three determining factors: the user controllability of the charging, the normalized final BSOC (battery state of charge) after the charging and the relative total charging cost.

$$S = SI(\mathrm{BSOC}_{final} / \mathrm{BSOC}_{target})(\mathrm{C}_{un} / \mathrm{C}_{real}) \quad (1)$$

Eq. (1) shows our proposed model for the calculation of user satisfaction *S*, which is the product of the three factors; *SI* denotes the satisfaction index. For those people who can control the EV charging, *SI* is set as 1; otherwise it is a constant positive fractional number; BSOC_{final} denotes the final BSOC after the charging; BSOC_{target} is the required BSOC predefined by the customer. The ratio of these two gives the indication of the battery charging status. Finally, C_{un} is the charging cost for EV charging without any control methods; and C_{real} shows the charging cost with certain EV charging control algorithm.

The user satisfaction for a specific network is defined in Eq. (2), which is the average among all the customers. In the equation, *n* means the number of EV customers in the neighborhood level network. S_i shows the customer satisfaction value for *i*-th customer.

$$S_{average} = \sum_{i=1}^{n} S_i / n \quad (2)$$

3. Methodology

As mentioned in Section 2, we consider that, there are two groups of customers in a neighborhood level network: contractual customers and non-contractual customers. It is assumed that, the EV charging control and communication devices have been installed for all the houses in the given neighborhood level network for contractual customers. The system operator can access full information of the contractual EVs: the real time BSOC, arrival time, predefined departure time and final BSOC requirement for their EVs. The charging behaviors of all the contractual EVs will be controlled by the system operator. For those non-contractual EVs, there is less information exchange between the EVs and the system operator. But the system operator can access the charging histories of these EVs. The non-contractual customers are assumed to be rational and would follow the electricity price signal to arrange the EV charging.

3.1 Mixed Control Algorithm

Fig. 5 shows the overview of the proposed energy management system. It is assumed that, there is a system operator who is responsible for controlling the charging for all the contractual EVs and deciding the time-of-use price structure for the neighborhood level network.

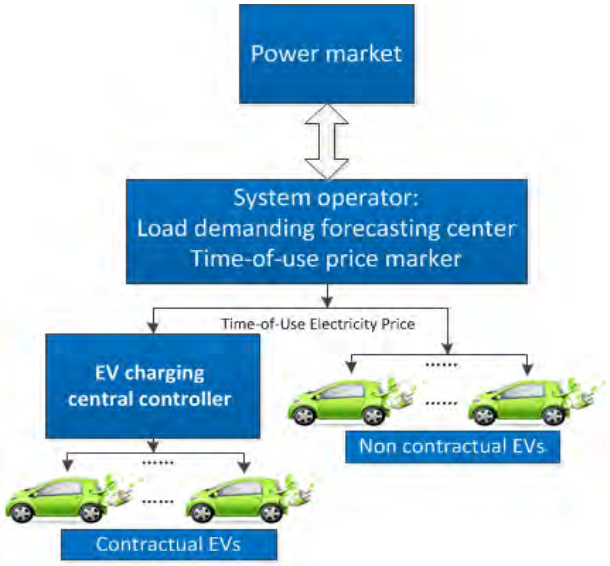

Fig. 5 Energy management system with mixed control strategy.

There are mainly three steps for the proposed mixed control algorithm. The first step is the load forecasting for base load power consumption. Different from Ref. [24], in this paper, we focus on the forecasting for base load power consumption. Load forecasting has been discussed in several previous Refs. [25-28]. In this paper, the time slot is chosen as 1 h. Weather information, weekday/weekend classification and hourly power consumptions for the previous day are used for load forecasting. Neural network is used for load forecasting for every hour in the next 24 h.

The second step is to determine the time-of-use price structure based on the forecasted load consumption. The pricing model proposed in Ref. [19] is adopted to determine the TOU structure. Fig. 6 shows an example the TOU price structure. We first find the maximal and minimal load consumption based on the forecasted result. The obtained timing region will be partitioned into three zones: valley, medium and peak hours. We assign 0.112$/kWh, 0.135$/kWh and 0.072$/kWh for the medium hours, peak hours and valley hours. The TOU price signal will be informed to all the non-contractual customers in the third step. TOU price acts as an incentive to realize the decentralized control for those non-contractual customers.

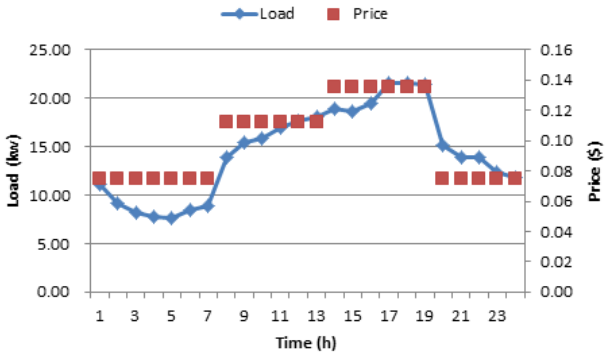

Fig. 6 Identification of zones for pricing.

3.2 Objective Function

The objective for our proposed optimization framework is to minimize the total charging cost for the contractual customers. The objective function F is shown in Eq. (3):

$$F = \min \sum_{i=1}^{m} \sum_{t} c_t \cdot P_{i,t} \tag{3}$$

In total, we assume there are n customers and m of all the customers are willing to give out the EV charging control. Without loss of generality, we assume that each customer owns one electric vehicle. Then there are m electric vehicles owned by contractual customers in the neighborhood level network, and $n-m$ EVs owned by non-contractual customers. $P_{i,t}$ means the charging power for the i-th EV in time interval t and c_t is the electricity price for that time interval.

3.3 Constraints

For the stability of the power system, all the following constraints should be satisfied in all time slots.

Total power constraint is shown in Eq. (4). It means that, for every time interval, the total charging power including the base load power consumption and the EV charging power consumption should be less than a certain value predefined by the transformer specification. As mentioned in Eq. (4), $PB_{i,t}$ means the base load consumption in i-th home for t-th time interval, $PC_{i,t}$ describes the charging power

consumption, and $PT_{\max}$ means the upper limit for the total power consumption.

$$0 \le \sum_{i=1}^{n} (PB_{i,t} + PC_{i,t}) \le PT_{\max} \quad (4)$$

EV charging power consumption is shown in Eq. (5). Continuous EV charging is adopted in this paper, which means that, the EV can be charged with power from zero to $PC_{\max}$, the maximal rated EV charging power.

$$0 \le PC_{i,t} \le PC_{\max} \quad (5)$$

BSOC constraints are shown in Eqs. (6) and (7). Eq. (6) shows that in all time slots the EV BSOC should be smaller than a predefined value ($BSOC_{max}$). Eq. (7) means that after the charging period, the final EV BSOC ($BSOC_{final}$) should satisfy the user predefined BSOC ($BSOC_{predefined}$) requirement.

$$0 \le \mathrm{BSOC}_{i,t} \le \mathrm{BSOC}_{\max} \quad (6)$$

$$BSOC_{predefined} \le BSOC_{final} \le BSOC_{\max} \quad (7)$$

Eq. (8) shows the BSOC updating constraint. Cap in this equation means the battery capacity. C is determined by the length of time interval, if time interval is 1 h, C will be 1. δ shows the conversion efficiency for EV charging.

$$\mathrm{BSOC}_{t+1} = \mathrm{BSOC}_{t} + C \cdot (\delta \cdot PC_i / \mathrm{Cap}) \times 100 \quad (8)$$

4. Simulation Results

4.1 Simulation Setup

The proposed EV charging control framework is tested with real data for a neighborhood level network from a local utility company. There are in total seven homes in the network as shown in Fig. 1. Uncontrolled charging and centralized control EV charging are used as comparisons for the proposed mixed EV charging control framework. For uncontrolled EV charging, we assume that, the customers will start charging their EVs once they arrive home with rated charging power. For centralized charging control, we assume that, the system controller can control the EV charging directly for all the EVs in the network. Simulation results for charging cost, user satisfaction, maximal EV penetration and peak power reduction are analyzed.

As shown in Table. 4, we consider three cases for the mixed charging control strategy according to the number of contractual customers. For example, in Case 2, four homes out of all the homes are contractual customers. This is also defined as the basic case for mixed control strategy.

Two kinds of electric vehicles: Honda Fit and Tesla model S are considered. The specifications for these two EVs are shown in Table. 1. The arrival BSOC, arrival time and departure time for all these EVs will be set according to the probability distribution of the survey mentioned in Section 2. For the total power constraints, $PT_{\max}$ is set as 60, the $BSOC_{max}$ is set as 95, $BSOC_{pre}$ is set as 80. The average initial BSOC for all EVs is 45%. For non-contractual customers, the user satisfaction index SI is set to be 0.8. The conversion efficiency for EV charging is set as 0.95. The optimization problem is solved with CPLEX (simplex method as implemented in the C Programming Language) 12.0.

4.2 Charging Cost and User Satisfaction Result

As described in Section 3, we assume that, the total operation cost and user satisfaction are two major factors for neighborhood level customers. The charging costs and user satisfactions for three representative charging control strategies are shown in Figs. 7 and 8.

The charging cost for three control strategies are shown in Fig. 7. We can see that, the charging cost for the mixed charging control strategy is significantly less than the uncontrolled strategy and close to the centralized control strategies. With mixed control strategy the charging cost will be reduced 16.2% and 19.5% for Honda Fit and Tesla Model S compared to uncontrolled EV charging.

Table 4 Mixed control strategy cases.

Cases	Case 1	Case 2	Case 3
#Contractual customers	3	4	5

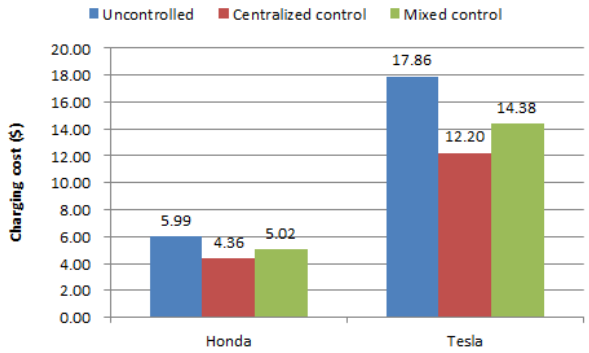

Fig. 7 Charging cost for different control strategies.

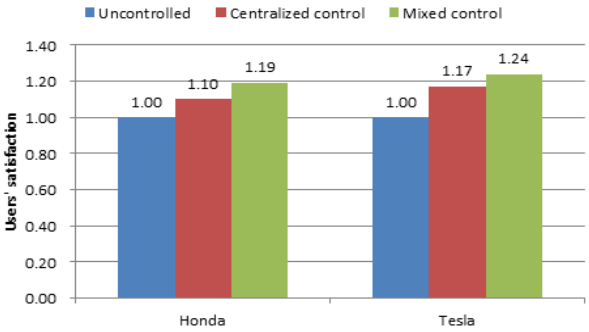

Fig. 8 User satisfaction for different control strategies.

User satisfaction for three representative charging control strategies is illustrated in Fig. 8. It can be seen that, for the mixed strategy, customers can have the highest overall user satisfactions. This is because the non-contractual customers can get full control of the EV charging and the overall charging cost is reduced. We can see that with the proposed criteria, user satisfaction can be well analyzed for different control algorithms.

The charging costs for the three cases for mixed control strategy are listed in Table. 5. We can see that, with the increasing of the number of contractual customers, we will have a lower charging cost.

4.3 Peak Power Consumption

Peak power consumption is another important factor for utility companies, as the overloaded power consumption will accelerate the grid ageing [29]. As mentioned in Ref. [30], a higher peak demand will require a larger generation capacity and cause the power system to be unstable. Fig. 9 shows the peak power consumptions for different control strategies. As the centralized control strategy could control the charging of all the EVs, this control algorithm provides the lowest peak power consumption. It can also be seen that, with the proposed mixed control strategy, the peak power consumption could be reduced significantly. Compared with uncontrolled EV charging, the peak power consumptions are reduced 37.6% for Honda Fit and 33.22% for Tesla Model S.

4.3 EV Penetration Result

The adoption of the EVs will increase the burden on the power system which may require related infrastructure upgrade. It would be an interesting question for the utility companies to know the potential EV penetration for a given neighborhood level network. The possible EV penetration for a given network is discussed in Refs. [5, 31]. However, most of them focused on pure centralized or decentralized control strategy. This may not be ideal or realistic as discussed in previous sections.

The proposed mixed control framework can also be adopted to find a more realistic EV penetration for a

Table 5 Contractual Customer number.

# Contractual customers	3	4	5
Charging cost Honda ($)	5.33	5.02	4.9
Charging cost Tesla ($)	15.41	14.38	13.7

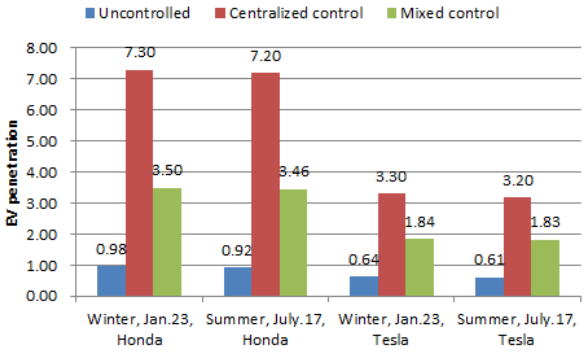

Fig. 9 Peak power consumption.

given network. To find the EV penetration, we can set the objective function in Section 4 as the number of EVs in every home. With the proposed framework, the simulation result will be more practical.

The EV penetration for three representative charging control strategies is analyzed on the two specific days. Simulation results are shown in Fig. 10. As the base load consumption is higher in summer than in winter, the EV penetration in winter is a little higher than that in summer. In all three strategies, we can get the highest EV penetration with the centralized control strategy.

For typical summer day, EV penetration can only be 0.92 for Honda Fit and 0.61 for Tesla Model S if the EV charging is left uncontrolled. With mixed charging control strategy, the EV penetration could be 3.46 for Honda Fit EV and 1.83 for Tesla Model S. We can also see that as the Tesla Model S require high EV charging rate which limits its penetration potential.

EV penetrations for mixed control strategy with different contractual customer numbers are shown in Fig. 11. We can see that, with an increase of contractual customers, the EV penetration will increase accordingly.

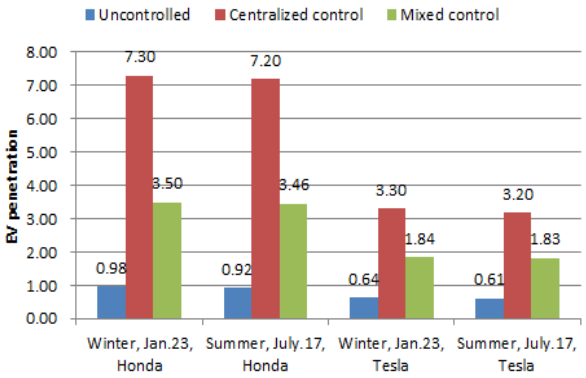

Fig. 10 EV penetration for different control strategies.

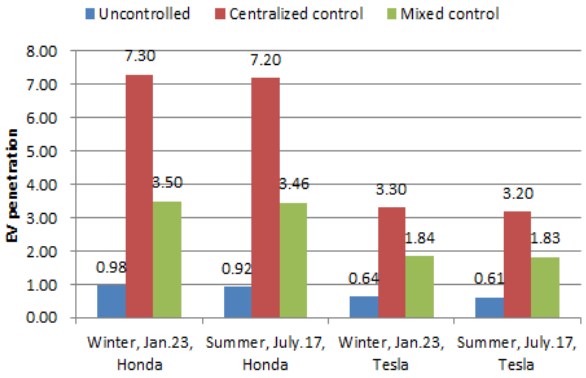

Fig. 11 EV penetration for mixed control strategies.

5. Conclusions

The fast development of EVs will induce negative impacts for power system and accelerate grid ageing if the EV charging is left uncontrolled. In this paper, the charging control for the EVs has been analyzed. A mixed control strategy and its optimization framework are proposed to mitigate the EV charging problem while considering the willingness of the customers. Compared with previous charging control strategies, in the proposed framework we consider that in the actual neighborhood level network, not all the customers would like to sign related contract with the utility companies and give out the charging control for their EVs.

A new user satisfaction model is also described in this paper, which will help study the user satisfactions for different control strategies. The EV penetration, charging cost and user satisfactions for the proposed control framework, as well as the centralized control strategy and uncontrolled charging are studied. Simulation results show the efficiency of the proposed smart charging control framework. With the proposed method, we can get a higher EV penetration and lower charging cost. We can see that, the proposed strategy is beneficial for both the utility companies and the customers.

References

[1] DOE (US Department of Energy). 2011. *One Million Electric Vehicles by 2015.* Virginia: US Department of Energy.

[2] Shireen, M. K., and Das, D. 2008. “Biohydrogen as a Renewable Energy Resource—Prospects and Potentials.” *International Journal of Hydrogen Energy* 33 (1): 258-63.

[3] Green, A. R. C., Wang, II, L., and Alam, M. 2011. “The

Impact of Plug-in Hybrid Electric Vehicles on Neighborhood Networks: A Review and Outlook." *Renew. Sustain. Energy Rev.* 15 (1): 544-53.

[4] Azad, A. P., Olivier, B., and Pfeiffer, L. 2013. "An Optimal Control Approach for EV Charging with Distribution Grid Ageing." In *Proceedings of the 2013 First International Black Sea Conference on Communications and Networking (BlackSeaCom), IEEE,* 206-10.

[5] Peter, R., Damian, F., and Andrew, K. 2012. "Optimal Charging of Electric Vehicles in Low-Voltage Distribution Systems." *IEEE Transactions on Power Systems* 27 (1): 268-79.

[6] Rotering, N., and Ilic, M. 2011. "Optimal Charge Control of Plug-in Hybrid Electric Vehicles in Deregulated Electricity Markets." *IEEE Trans. Power Systems* 26 (3): 1021-9.

[7] Ahn, C., Li, C. T., and Peng, H. 2011. "Decentralized Charging Algorithm for Electrified Vehicles Connected to Smart Grid." In *Proceedings of the ACC (American Control Conference),* 3924-9.

[8] Li, N., Chen, L., and Low, S. H. 2011. "Optimal Demand Response Based on Utility Maximization in Power Networks." In *Proceedings of the IEEE Power and Energy Society General Meeting,* 1-8.

[9] Kahn, M. E. 2008. "Green Market Geography: The Spatial Clustering of Hybrid Vehicle and LEED Registered Buildings." Working Paper 2008-19, UCLA (University of California Los Angeles) Ziman Center for Real Estate.

[10] Aultman-Hall, L., Sears, J., Dowds, J., and Hines, P. 2012. "Travel Demand and Charging Capacity for Electric Vehicles in Rural States: A Vermont Case Study." Presented at the Transport Research Board 92nd Annual Meeting, Washington, USA.

[11] Kempton, W., and Letendre, S. E. 1997. "Electric Vehicles as a New Power Source for Electric Utilities." Transportation Research Part D: Transport and Environment 2 (3): 157-75.

[12] Chagngsun, C. H. 2011. "Dencentralized Charging Alogorithm for Electricfied Vehicles Connected to Smart Grid." In *Proceedings of the ACC (American Control Conference),* 3924-9.

[13] Komang A. I., and Kab, S. 2013. "A Centralized Scheme Based on User Satisfaction Fairness and Cost." In *Proceedings of the IEEE ISGT Asia (Innovative Smart Grid Technologies—Asia),* 1-4.

[14] Papadaskalopoulos, D., and Strbac, G. 2012. "Decentralized Participation of Electric Vehicles in Network-Constrained Market Operation." In *Proceedings of the 3rd IEEE PES International Conference and Exhibition on ISGT (Innovative Smart Grid Technologies) Europe,* 1-8.

[15] Xiaomin, X., and Sioshansi, R. 2014. "Using Price-Based Signals to Control Plug-in Electric Vehicle Fleet Charging." *IEEE Transaction on Smart Grid* 5 (3): 1451-64.

[16] Hong, L., and Shaoyun, G. 2013. "Optimization of TOU Price of Electricity Based on Electric Vehicle Orderly Charge." In *Proceedings of the IEEE PES (Power and Energy Society) General Meeting,* 1-5.

[17] Vaya, M. G., and Anderson, G. 2012. "Centralized and Decentralized Approaches to Smart Charging of Plug-in Vehicles." In *Proceedings of the IEEE Power and Energy Society General Meetings,* 1-8.

[18] Ruoyang, L., Qiuwei, W., and Oren, S. S. 2014. "Distributional Locational Marginal Pricing for Optimal Electric Vehicle Charging Management." *IEEE Trans. Power Systems* 29 (1): 203-11.

[19] Yan, Q. 2014. "A Multi-tied Real-Time Pricing Algorithm for Electric Vehicle Charging Station." In *Proceedings of the ITEC (IEEE Transportation Electrification Conference) and Expo,* 1-6.

[20] Grunewald, A., Hardt, S., and Mielke, M. 2012. "A Decentralized Charge Management for Electric Vehicles Using a Genetic Algorithm: Case Study and Proof-of-Concept in Java and FPGA." In *Proceedings of the IEEE CEC (Congress on Evolutionary Computation),* 1-7.

[21] TESLA. 2014. "85 kWh Battery." Tesla Motors. Accessed May 20, 2015. http://www.teslamotors.com/en_CA/charging#/basics.

[22] HONDA. 2014. "2014 Accord Plug-in." American Honda Motor Co., Inc. Accessed May 20, 2015. http://automobiles.honda.com/accord-plug-in/charging-an-electric-vehicle.aspx.

[23] Oliver, B., Probe, P., and Flores, M. 2013. "EMAP: Informing the Development of an EV Deployment Strategy in the City of Ottawa." Presented at Evve Conference and Trade Show, Gatineau, Canada. Accessed May 20, 2015. http://emc-mec.ca/evve2013/pdfs/22OCT/TS8/3_Oliver_Flores.pdf.

[24] Wu, D., Haibo, Z., and Benoit, B. 2014. "Neighborhood Level Network Aware Electric Vehicle Charging Management with Mixed Control Strategy." In *Proceedings of the 2014 IEEE IEVC (International Electric Vehicle Conference),* 1-7.

[25] Dongxiao, N., Yongli, W., and Desheng, D. W. 2010. "Power Load Forecasting Using Support Vector Machine and ant Colony Optimization." *Expert Systems with Applications* 37 (3): 2531-9.

[26] Bakirtzis, A. G. 1996. "A Neural Network Short Term Load Forecasting Model for the Greek Power System." *IEEE Transactions on Power Systems* 11 (2): 858-63.

[27] Senjyu, T. 2002. “One-Hour-Ahead Load Forecasting Using Neural Network.” *IEEE Transactions on Power Systems* 17 (1): 113-8.

[28] Lu, C. N., Wu, H. T., and Vemuri, S. 1993. “Neural Network Based Short Term Load Forecasting.” *IEEE Transactions on Power Systems* 8 (1): 336-42.

[29] Rutherford, M. J., and Yousefzadeh, V. 2011. “The Impact of Electric Vehicle Battery Charging on Distribution Transformers.” In *Proceedings of the 26th IEEE APEC (Applied Power Electronics Conference) and Exposition*, 396-400.

[30] Shizhen, Z., Xiaojun, L., and Minghua, C. 2013. “Peak-Minimizing Online EV Charging.” Allerton.

[31] Rocha, A. P. M., Peças, L. J. A., and Soares, F. J. 2011. “Electric Vehicles Participating in Frequency Control: Operating Islanded Systems with Large Penetration of Renewable Power Sources.” In *Proceedings of the IEEE Power Tech.*, 1-6.

Journal of Energy and Power Engineering 9 (2015) 741-752
doi: 10.17265/1934-8975/2015.08.008

Fuzzy Logic Controlled Dual Active Bridge Series Resonant Converter for DC Smart Grid Application

Thabit Salim Nassor, Atsushi Yona and Tomonobu Senjyu

Graduate School of Engineering and Science, University of the Ryukyus, Okinawa 903-0213, Japan

Received: May 25, 2015 / Accepted: July 01, 2015 / Published: August 31, 2015.

Abstract: Over the last few years, smart grids have become a topic of intensive research, development and deployment across the world. This is due to the fact that, through the smart grid, stable and reliable power systems can be achieved. This paper presents a fuzzy logic control for dual active bridge series resonant converters for DC smart grid application. The DC smart grid consists of wind turbine and photovoltaic generators, controllable and DC loads, and power converters. The proposed control method has been applied to the controllable load's and the grid side's dual active bridge series resonant converters for attaining control of the power system. It has been used for management of controllable load's state of charge, DC feeder's voltage stability during the loads and power variations from wind energy and photovoltaic generation and power flow management between the grid side and the DC smart grid. The effectiveness of the proposed DC smart grid operation has been verified by simulation results obtained by using MATLAB® and PLECS® cards.

Key words: DC smart grid, dual active bridge series resonant converter, wind turbine, controllable loads, photovoltaic.

1. Introduction

For more than five decades, the power system has heavily depended on fossil fuels, including oil, coal and natural gas, as energy sources. These fossil fuels are nonrenewable and the reserves on the earth are being consumed rapidly. Also exhaust generated from these resources is associated with the environmental destruction such as global warming and pollution [1]. Therefore, in response to these challenges, global attention has been focused on finding alternative energy resources that can sustain long-term industry development. Currently, the identified and implemented RES (renewable energy sources) include wind, hydro, solar, tidal, geothermal and waste energy. These resources are also called green energy because they do not release carbon dioxide (CO_2) into the atmosphere during electric energy generation and are abundant in nature. These RES are important substitutes of fossil fuels for their exploitation durability and environmental friendliness. In fact, this situation has brought about many research studies and deployment across the world for effective methods to harness the RES.

The SG (smart grid) is a re-working of electricity infrastructures-encompassing technology, policy, and business models, which is under way globally [2]. The smart grid architecture would encompass but is not limited to distribution automation/management systems, an advanced metering infrastructure, data communication, and intelligent devices and tools for monitoring, control and optimization. By engaging in the smart grid, several challenges associated with current power and energy systems can be addressed. These include: greenhouse gas emissions and climate change, reliability, economic and energy security as explained in Ref. [2].

For better operation of electrical power systems which incorporate diversified RES, the smart grid is a critical system that determines the effectiveness and efficiency of these systems. It offers a variety of

Corresponding author: Thabit Salim Nassor, Ph.D. student, research fields: smart grid, power system control, intelligent energy management, power electronics and renewable energy. E-mail: nassor2@hotmail.com.

advantages over the current systems in terms of digitalization, flexibility, intelligence, resilience, sustainability and customization [3].

The DC grid has the following advantages compared to an AC power distribution system: (1) Each power generator connected to the DC grid can easily be used cooperatively because the DC grid controls only the DC bus voltage; (2) when the AC grid experiences abnormal or fault conditions, the DC grid is disconnected from the AC grid, and it is then switched to stand-alone operation, in which the generated and stored power are supplied to the loads connected to the DC grid, hence, loads can be operated continuously without instantaneous interruption; (3) the cost and losses involved with the DC system can be reduced because only a single AC grid connected inverter unit is needed; (4) distributed generators usually supply DC power. Therefore, the phase detection associated with the AC grid is not needed. Thus, the cost and loss of the system can be reduced; and (5) although a DC distribution line is required, the cost performance of DC houses, hospitals, and information centers are satisfactory [4].

At present, only AC smart grids are used in practical applications, whereby the DCSG (DC smart grid) has been proposed by the authors [5-8]. In Refs. [5, 6], the authors have proposed the operation of a DC MSG (DC micro smart grid) and the multi DC smart grid in isolated mode. However, there was no discussion on how the DC MSG will operate in insolation mode, especially if there is less power generation in comparison to load demand. Moreover, the operation in deficit or surplus power in the system was not considered.

In Refs. [7, 8], the authors covered the earlier mentioned cases and proposed protection of the DC transmission line in multi DC smart grid operation, respectively. Nevertheless, neither of the papers considered controllable load and power flow management during the grid connected mode of operation.

In this paper, the fuzzy logic control has been used for controlling PWM (pulse width modulation) delay angle of the DABSRCs (dual active bridge series resonant converters) for different operation conditions. These includes: controllable load's SOC (state of charge) management, DC feeder's voltage stability and power flow management between the grid side and the DCSG. The fuzzy logic control is used due to its benefits compare to other controls which includes: design simplicity, robustness and minimal requirement for accurate mathematical model [9], can be well implemented to low-resolution analogue to digital converters and low-cost systems based on cheap sensors [10].

The proposed DCSG consists of a PMSG (permanent magnet synchronous generator) WT (wind turbine) and PV generation, a WT generator inverter, a PV boost converter, a GS (grid-side) and CL (controllable load) DABSRCs, controllable loads, and normal DC loads. During the DCSG operation, the DC distribution line voltage fluctuations due to power supplied by the renewable energy plants (WT and PV) and loads are suppressed by applying the power consumption control to the CL. In the case where the CL cannot stabilize the system, the GS converter will participate in power stabilization and CL management by power transfer operation between DCSG and grid.

This paper has been organized as follows: Section 2 describes the modeling of all components of the power system including WT and PV generators, converters and loads with their control system. Section 3 discusses the results, which are obtained in different operation cases. The paper is finalized with Section 4 which will present conclusions from this work.

2. Power System Modeling and Control

The proposed DCSG power system as shown in Fig. 1 contains a WT and PV generators, variable DC loads, controllable loads, a generator-side converter, C_{WT}, PV boost converter, C_{PV}, and bidirectional DC/DC converters, DABSRCs, for connecting the controllable

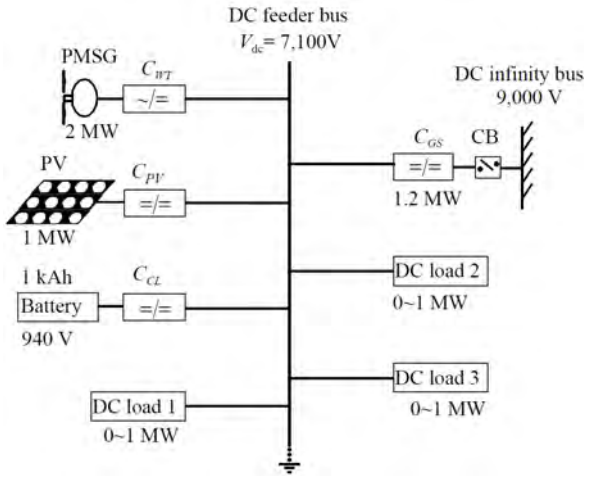

Fig. 1 The system configuration block diagram of the DC smart grid.

loads, C_B, as well as the grid, C_{GS}, which is connected to DC infinity bus though DC CB (circuit breaker). The PMSG's and PV's output power are supplied to the DC loads through the DC feeder (DC distribution line). When excess power in PMSG and PVs is generated relative to the loads demand, it is supplied to the grid through the grid connected converter. The grid connected and controllable load DABSRCs control their output power to maintain: (1) feeder's voltage, V_{dc} within a range of ± 5%, and (2) operation management of controllable load power's SOC within the acceptable range of 80%-20% for upper and lower limits [11]. The operations of the converters are controlled using fuzzy logic control.

2.1 Wind Energy Conversion System

The WTG (wind turbine generator) is a gearless 2 MW PMSG as modeled in Refs. [12-14]. The PMSG has a simple structure and high efficiency; it is expected to be installed in the next generation of WTG systems. Wind power energy obtained from the windmill is sent to the PMSG. In order to generate maximum power, the rotational speed of the PMSG is controlled by the PWM converter. The generator-side converter controls the rotational speed of the PMSG in order to achieve variable speed operation with MPPT (maximum power point tracking) control and implements the maximum torque control [15, 16]. Optimum rotational speed of the PMSG used in this paper is approximated as in Eq. (1) for MPPT [5]:

$$\omega_{e\_opt} = 2.0615 V_w \tag{1}$$

where, ω_{e_opt} is optimum rotational speed of the PMSG in rad/s and V_w is wind speed in m/s.

Generally, the MPPT control is applied when V_w is smaller than the rated wind speed, V_{rw}. If the V_w is greater than V_{rw}, then the output power of the PMSG is controlled by the pitch angle (β) control system. When V_w ranges between cut-in V_w (5 m/s) to rated V_w (12 m/s), the β is set to 0°, since wind windmill energy is maximum at 0° [14], when V_w is between V_{rw} and the cut-out V_w (24 m/s), the pitch angle is controlled to deliver windmill output (P_g = *1*), when the V_w is above the cut-out V_w the β is set to 90° because the energy of a windmill is the smallest at 90°. The control diagram is shown in Fig. 2. The detailed pitch angle control was described in Ref. [17].

The speed control of the PMSG is realized on a rotating frame, where the rotational speed error from optimum rotational speed, ω_{e_opt} and measured rotational speed, ω_e are used as the input of the speed controller (PI_1), which produces, q axis stator current command, i_{1q}^* as shown in Fig. 3. Generally, the salient pole type synchronous machine is desirable to control the *d*-axis stator current, i_{1d} and the reference i_{1d}^* as expressed in Eq. (2).

$$i_{1d}^* = \frac{\phi_f}{2(L_d - L_q)} - \sqrt{\frac{\phi_f^2}{4(L_q - L_d)^2} + i_{1q}^2} \tag{2}$$

where, ϕ_f is the permanent magnetic flux, L_d and L_q are the *dq*-axis inductance, and i_{1q} is the *q*-axis current. The parameters of the PMSG and windmill are shown in Table 1 [5].

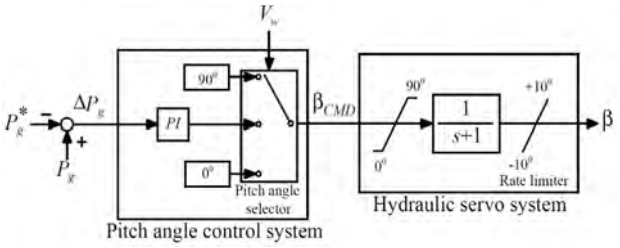

Fig. 2 Pitch angle control system.

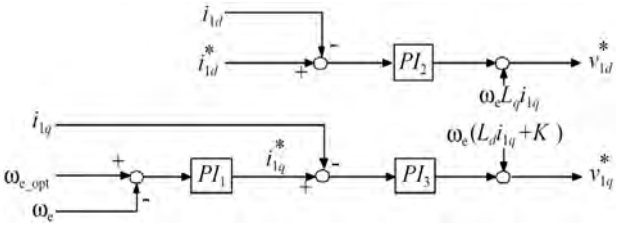

Fig. 3 Generator-side converter control system.

2.2 PV System

PV generation is very important for the utilization of renewable energy provided by the sun. A PV generator converts solar or artificial light to electric energy due to the movement of positive and negative charge carriers when the light strikes its surface. Normally, the PV generation systems suffer low energy conversion efficiency due to non-linear variations of output voltage and current, which is caused by environmental and operational conditions [18]. These include: ambient temperature, operating temperature, insulation, dirt, sunlight characteristics and load current technologies [18, 19]. Different methods have been used and proposed for solving this problem, such as: (1) sun tracking; (2) MPPT; and (3) a combination of both [19].

Single diode PV model as in Refs. [20, 21] has been used for modeling the PV generation system in this research. Eq. (3) describes the output current (I) of the PV from the model.

$$I = I_L - I_D \tag{3}$$

where,

$$I_D = I_0\left(e^{\frac{q(V+IR_S)}{nkT}} - 1\right)$$

$$I_L = I_L(T_1)(1 + K_0(T - T_1))$$

$$I_{L(T_1)} = \frac{GI_{SC(T_{1,\,nom})}}{G_{(nom)}}$$

$$K_0 = \frac{I_{SC(T_2)} - I_{SC(T_1)}}{T_2 - T_1}$$

where, I_L is the current source which is equal to the short circuit current, I_{SC} and directly proportional to solar irradiance, G (W·m^2), R_s is the series resistance, I_0 is the reverse saturation current of the diode, q is the electron charge (1.60 × 10^{-19} C), V_d is the voltage across the diode, k is Boltzmann constant (1.38 × 10^{-23} J/K), T is the junction temperature (K), T_1 is the standard PV designed temperature (25 °C), T_2 is the ambient temperature (°C) and n is the diode ideality factor.

Table 1 Parameters of wind turbine generator.

Rated power	P_{ref}	2	MW
Rated wind speed	V_{w_ref}	12	m/s
Stator resistance	R_a	0.01	pu
Leakage inductance	L_{ls}	0.1	pu
Stator d/q axis inductance	L_d, L_q	1/0.65	pu
Number of pole pairs	p	11	
Field flux	K	136.25	Wb
Radius of wind turbine rotor	R	38	m
Equivalent inertia	J_{eq}	8,000	kg·m^2
Rotational damping	D	0	

In this paper, in order to generate maximum and optimum power from the PV system as the temperature, insolation and load varies, a maximum power point tracker has been implemented to DC/DC boost converter connected between the PV system and distribution line as shown in Fig. 4. The PV modules have been modeled and arranged in parallel and series to give out power of 1 MW. The PV module has been modeled as of BP365 65 W with the specifications shown in Table 2.

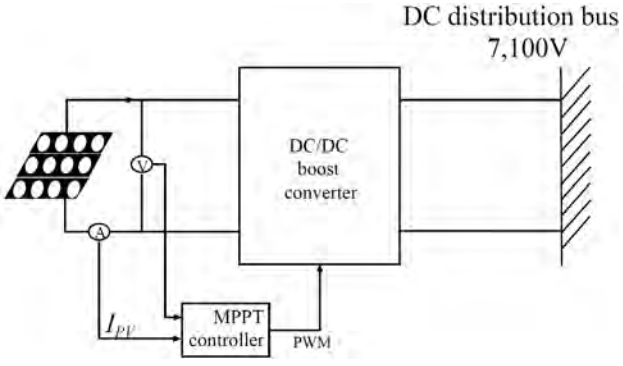

Fig. 4 PV system model.

Table 2 Specifications of the BP365 65 W PV module.

Maximum power	P_m	65	W
Voltage, max power	V_m	17.6	V
Current, max power	I_m	3.69	A
Open circuit voltage	V_{OC}	22.1	V
Short circuit current	I_{sc}	3.99	A

2.3 Controllable Loads

In this paper, the DC feeder voltage is maintained by the voltage control of the DC/DC converter connected to the controllable loads. Batteries are used as controllable loads. Although the battery is installed in DC houses, the EV (electric vehicle) will be also used as a battery in the future. The EV is important due to the depletion of energy sources and its availability as a backup power in the residential houses.

The battery is modeled as from Refs. [22, 23]. Terminal voltage, E_b and state of charge, SOC are calculated by Eqs. (4) and (5), respectively. A 940 V/1 kAh battery was modeled and used in the power system. In order to show all simulation condition results with high and low battery capacity, the charging and discharging time constant of 14 s was used instead of actual time of 1 h (3,600 s).

$$E_b = E_0 - R_b i_b - K\frac{Q}{Q+\int i_b \mathrm{d}t} + Ae^{(-B\int i_b \mathrm{d}t)} \quad (4)$$

$$SOC = 100(1-\frac{\int i_b \mathrm{d}t}{Q}) \quad (5)$$

where, E_0 is the battery constant voltage (V), R_b is internal resistance of the battery (Ω), i_b is the battery charging current (A), Q is the battery capacity (Ah), K is the polarization voltage (V), A is exponential voltage (V) and B is the exponential capacity (1/Ah).

2.4 Bidirectional Converter

The bidirectional converters chosen in this study to connect the controllable loads and grid bus to the DC distribution line are DABSRC as shown in Fig. 5. DABSRC has been chosen due to its numerous advantages such as, small size, low cost, simple control and high power density [24, 25]. Ref. [26] mentioned different modulation methods for these converters. In this paper, phase shift modulation was used. Among the advantages of this method are low complexity of computations for the phase shift method, simplicity of the circuit, and a reduction of power loss due to ZVS (zero voltage switching) [27].

The detailed AC analysis of this converter was described in Refs. [24, 25]. The output active power, P_0 which is the average value of instantaneous power, tank parameters, inductor, L_s and capacitor, C_s are given by Eqs. (6)-(8), respectively.

$$P_{0,\,pu} = \frac{1}{2\pi}\int_0^{2\pi} P_{pu}(t)\mathrm{d}(\omega_s t) = \frac{8M}{\pi^2 Q(F-\frac{1}{F})}\sin\varphi \quad (6)$$

$$Q = \frac{\omega_r L_s}{R_L^{'}} \quad (7)$$

$$F = \frac{\omega_s}{\omega_r} = \frac{f_s}{2\pi\sqrt{L_s C_s}} \quad (8)$$

where,

$$M = V_0^{'}/V_i = n_t\frac{E_2}{E_1}$$

$R_L^{'}$ is the load resistance transferred to the primary side, ω_r is angular resonant frequency, f_s is switching frequency, n_t:1 is transformer turns ratio, $V_0^{'}$ is output voltage transferred to the primary side, V_i is primary input voltage and φ is phase shift angle.

Eq. (6) can be used to determine φ for the amount of power delivered to either side of the converter, whereas the net power flow is positive with $\varphi > 0$ and negative with $\varphi < 0$. In Refs. [24, 25], the design curves were used to obtain the optimized values of voltage gain, (M = 0.95), normalized frequency, (F = 1.1), and value of Q which is equal to 1 for achieving soft switching, lower resonant current, high efficiency and small tank size. Table 3 shows the design parameters for controllable load and grid side bidirectional converters.

2.4.1 Fuzzy Logic Control Strategy for DABSRCs

Fuzzy logic is used in this paper for controlling the phase shift angle of the PWM of bidirectional converters. In controllable load's DABSRC, the fuzzy

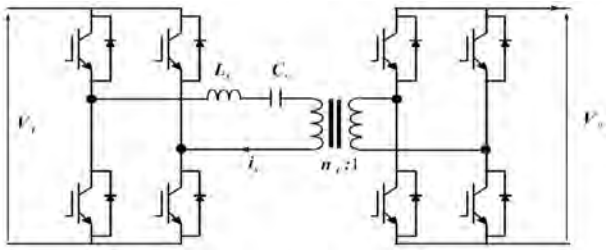

Fig. 5 Dual active bridge series resonant converter.

logic control strategy used for controlling phase shifting angle of PWM resulted from V_{dc} voltage fluctuations. This control has three inputs, error in V_{dc}, e, Δe and $\Delta^2 e$ as shown in Fig. 6, where their membership functions and fuzzy rules are shown in Fig. 7 and Table 4, respectively.

Cascaded fuzzy logic controller was used in the grid side converter as presented in Fig. 8. The first part determines the amount of power, ΔP to be delivered to either side due to the SOC, power flow from the battery (i.e., battery current), and V_{dc}. Their membership functions and fuzzy rule are as shown in Fig. 9 and Table 5, respectively. The second part is the same in operation as that of controllable load converter (fuzzy 1 controller) but with different input limits of e, Δe and $\Delta^2 e$.

2.4.2 Controllable Load DABSRC Control

In this paper, the DC distribution voltage is controlled by both DABSRC converters connected to the controllable load and the infinite supply (grid). During power system operation, the main targets are to minimize the energy flow from the infinite supply to the DCSG, to maximize the power delivered to the infinite supply, yet maintain a stable DC distribution voltage and SOC management. The proposed control system for the DABSRC connected to the controllable load has the role of ensuring a stable DC distribution voltage, as illustrated in Fig. 7. In this control system, the DC feeder voltage fluctuations in the DCSG due to RES and load variation is suppressed by the phase shift angle command of the DABSRC connected to the controllable load. The phase shift angle for the amount of delivered power is determined by the fuzzy controller based on the amount of voltage fluctuation. The error between the V_{dc}^* and V_{dc} is used to determine the angle for active power flow in the DABSRC. If V_{dc} is less than the V_{dc}^*, the fuzzy controller will determine and give positive PWM phase shift angle for power flow from the controllable load to the distribution line. If V_{dc} is greater than V_{dc}^*, negative PWM phase shift angle will be given by the controller for power flow from the distribution line to the controllable load.

Table 3 DABSRCs design parameters.

Parameter	Abbreviation	Cload DABSRC	GS DABSRC
Rated active power (MW)	P_0	1.00	1.20
Voltage (V)	E_1/E_2	7,100/940	7,100/9,000
Turns ratio	n:1	7.18	0.75
Switching Frequency (kHz)	f_s	100	100
Capacitor (μF)	C_s	38.48	46.18
Inductor (mH)	L_s	79.65	66.37

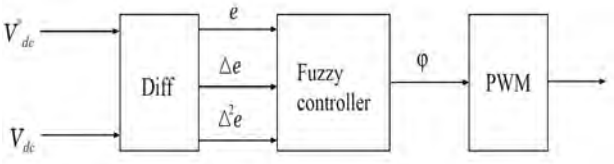

Fig. 6 Controllable load control system.

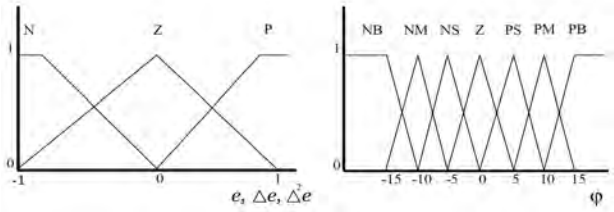

Fig. 7 Fuzzy 1 membership functions.

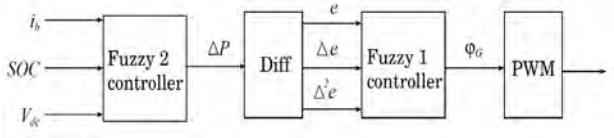

Fig. 8 Grid side converter control system.

Table 4 Fuzzy 1 rules for φ.

		e								
		N			Z			P		
Δe		N	Z	P	N	Z	P	N	Z	P
	N	NB	NB	NM	NM	NS	Z	Z	PS	PM
$\Delta^2 e$	Z	NB	NM	NS	NS	Z	PS	PS	PM	PB
	P	NM	NS	Z	Z	PS	PM	PM	PB	PB

N = negative, NB = negative big, NM = negative medium, Z = zero, P = positive, PM = positive medium, PB = positive big.

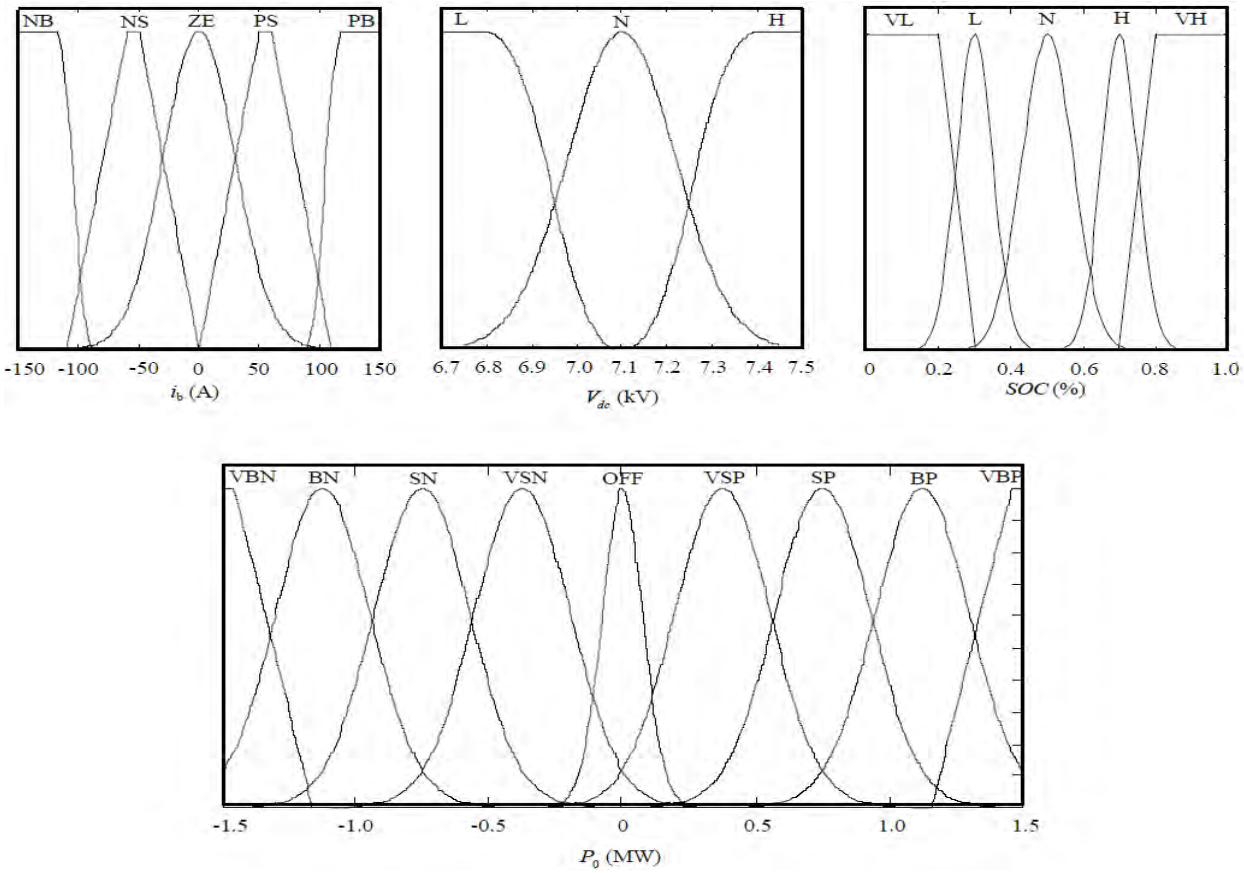

Fig. 9 Fuzzy 2 membership functions.

Table 5 Fuzzy 2 rules for ΔP_0.

		V_{dc}						
		H			N			L
i_b		BN	BN	SN	Z	SP	BP	BP
	VL	VSN	VSP	SP	BP	VBP	VBP	VBP
	L	SN	Z	Z	Z	Z	Z	LP
SOC	N	SN	Z	Z	Z	Z	Z	SP
	H	BN	Z	Z	Z	Z	Z	SP
	VH	VBN	VBN	VBN	BN	SN	VSN	VSP

VBN = very big negative, BN = big negative, SN = small negative, Z = zero, SP = small positive, BP = big positive, VBP = very big positive, VL = very low, L = low, N = normal, H = high, VH = very high.

2.4.3 Grid Side DABSRC Control

With a surfeit or deficit of power generation over the load demand, or when the SOC management of the controllable load is needed, the grid connected DABSRC is controlled to stabilize the power system. By power transfer operation between the DCSG and the grid, distribution line voltage stabilization and SOC management are guaranteed. In the case of power transfer, when excess power is generated or a deficiency of power occurs in a DCSG, the amount of the power to be transferred to either side is determined by the fuzzy controller shown in Fig. 8. The first part determines the amount of power, ΔP to be delivered to either side and thesecond part is fixing PWM shift angle corresponding to the calculated ΔP. Therefore, V_{dc} of the DCSG is also controlled according to the energy transfer between DCSG and grid side when the grid side converter is in operation.

3. Simulation Results

The simulation of the power system model in Fig. 1 has been carried out for different operation cases of the DCSG. Figs. 10 and 11 present the wind speed and solar insolation for WT and PV power generation. The generated active power from WT (P_{WT}), PV (P_{PV}) and their summation (P_{TG}) are presented in Figs. 12-14, respectively.

Furthermore, Fig. 15 shows three DC loads (P_L) with a maximum consumption of 1 MW each switched in different capacities to show the effectiveness of the power system, while Fig. 16 describes the total combined DC load (P_{TL}) as seen by the control system during operation. For power stabilization in the DCSG, due to power generation and load variation during simulation, the controllable load converter phase shift angle (φ_{CL}) is shown in Fig. 17 and its corresponding active power output (P_{CL}) is shown in Fig. 18. Whereas, a phase shift angle of grid converter (φ_G) is shown in Fig. 19 with its active output power (P_G) in Fig. 20.

Moreover, despite the power generation and load variations, Fig. 21 shows that, the SOC of the battery is well maintained within acceptable operating boundaries and also the distribution line voltage, V_{dc} always stays within acceptable limits of $\pm 5\%$ of V_{dc} as shown in Fig. 22.

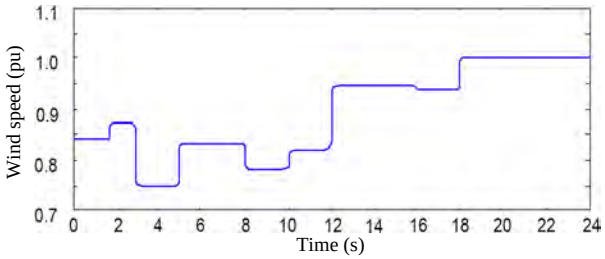

Fig. 10 Wind turbine speed.

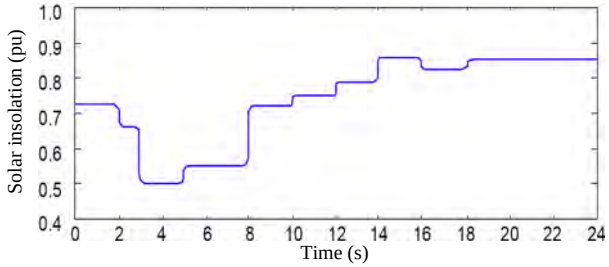

Fig. 11 Solar insolation.

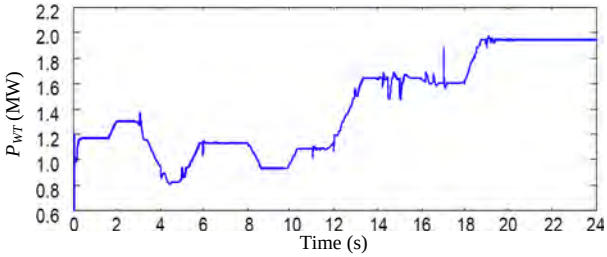

Fig. 12 Wind turbine active power.

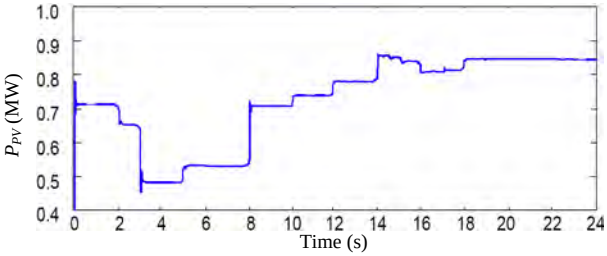

Fig. 13 Photovoltaic active power.

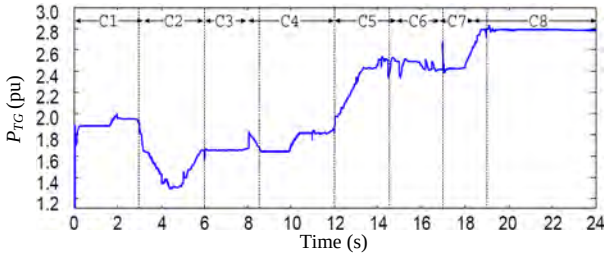

Fig. 14 Total active power generation.

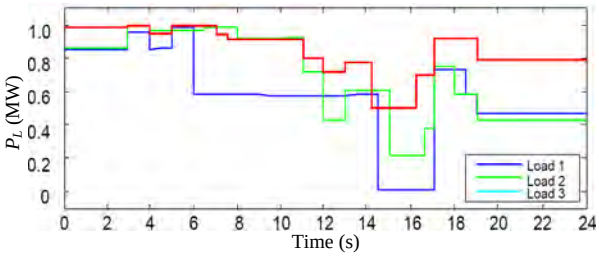

Fig. 15 DC loads .

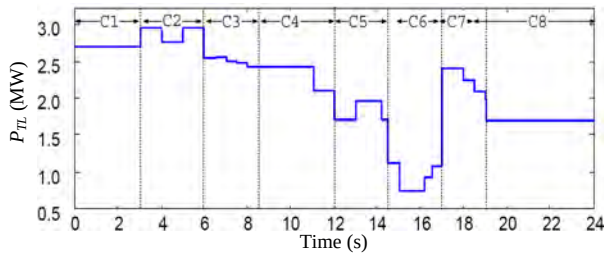

Fig. 16 Total DC loads.

Apart from that, in the simulation results shown from Figs. 10-22, different scenarios have been tested during the simulation to show how the power system will react in response to changes in power generation, load variation and the on-line battery SOC. These

scenarios are explained from Case 1 to Case 8 (C1-C8), and their summaries are presented in Table 4.

Case 1: This case presents the operation mode of DCSG in which the power generated from WT and PV, and load demand are balanced as shown in the simulation results from t = 0 s to t = 3 s. Different DC load capacities have been switched in order to show the demand response operation of the system. Since the SOC of the controllable load (battery) is high and the load power demand can be fulfilled by the controllable load alone, hence the output power of the grid converter is kept at zero as shown in Fig. 20 and V_{dc} is kept constant at the nominal value of 7,100 V as shown in Fig. 22. Therefore, the V_{dc} voltage is kept within the acceptable range in isolated mode.

Case 2: This scenario is shown in the simulation results from t = 3 s to t = 6 s. In this case, even though the SOC is within the desired operating region as shown in Fig. 21, the V_{dc} in Fig. 22 starts to drop due to insufficient power from controllable loads, which are operating at maximum output power as shown in Fig. 18, and low power generation from the RES, as shown in Fig. 14. Hence, the grid converter gives power to the DCSG as shown in Fig. 20 so that the V_{dc} is maintained at the accepted range.

Case 3: From t = 6 s to t = 8.5 s, power generation increases as shown in Fig. 14. Since the SOC is within the desired operating region as shown in Fig. 21, and the batteries can be used to stabilize V_{dc} and maintain it constant at the nominal value of 7,100 V as shown in Fig. 22, therefore, the grid converter power output to the DCSG was abstained.

Case 4: From t = 8.5 s to t = 12 s though the battery can still supply power to stabilize the V_{dc} at 7,100 V, at t = 8.5 s the lower limit of the SOC was approached as shown in Fig. 21. The grid converter was controlled to give power to the DCSG so that SOC can be improved.

Case 5: In this case, the SOC has been improved enough for the battery alone to control the V_{dc} fluctuations as shown in Fig. 21 from t = 12 s to t = 14.5 s. Since the V_{dc} is kept at 7,100 V by the controllable load converter as shown in Fig. 22, therefore, the grid converter gives no power to the DCSG as shown in Fig. 20.

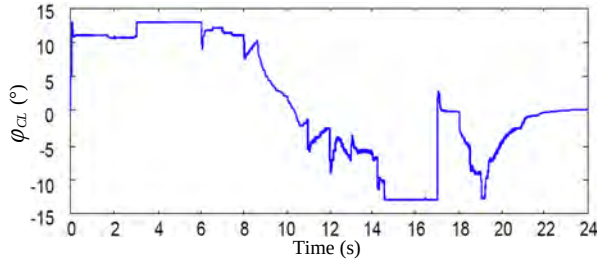

Fig. 17 Phase shift angle of controllable load converter.

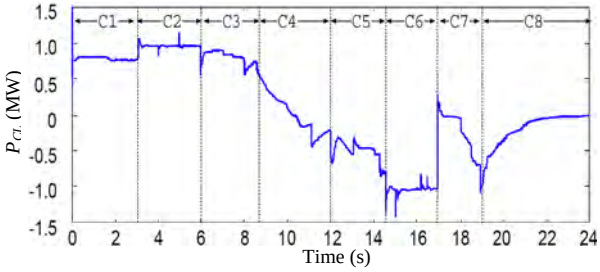

Fig. 18 Controllable load active power.

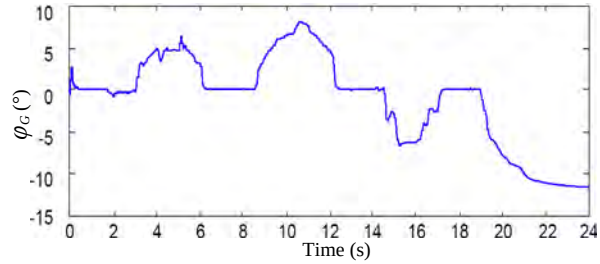

Fig. 19 Phase shift angle of grid converter (φ_G: φ of grid side converter).

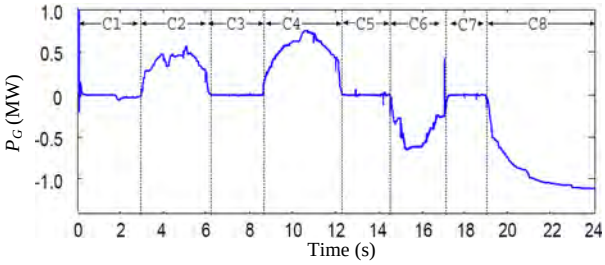

Fig. 20 Grid converter active power.

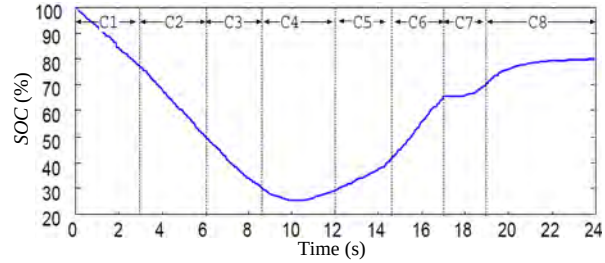

Fig. 21 Controllable load SOC.

Table 6 Simulation results summary.

Cases	Time interval (s)	SOC	Load demand	CL converter	GS converter	V_{dc}
l	0-3	High	Balanced	Control V_{dc}	No power output	Constant at 7,100 V
2	3-6	Within the range	High	Give maximum power	Give power	Within the range
3	6.5-8.5	Within the range	Balanced	Control V_{dc}	No power output	Constant at 7,100 V
4	8.5-12	Low	Balanced	Control V_{dc}	Give power	Constant at 7,100 V
5	12-14.5	Within the range	Balanced	Control V_{dc}	No power output	Constant at 7,100 V
6	14.5-17	Within the range	Low	Take maximum power	Take power	Within the range
7	17-19	Within the range	Balanced	Control V_{dc}	No power output	Constant at 7,100 V
8	19-24	High	Low	No power output	Take power	Constant at 7,100 V

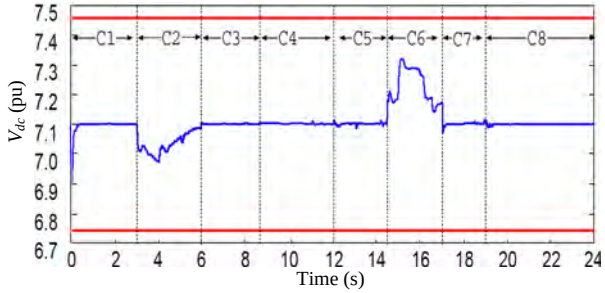

Fig. 22 Distribution line voltage.

Case 6: From t = 14.5 s to t = 17 s, the DC load decreased significantly and caused extra power generated exceeding load demand in the DCSG. Even though the battery SOC is within the desired operating region as shown in Fig. 21, but since it was charging to its full capacity as shown in Fig. 18 and still the extra power tend to increase the V_{dc}, the grid converter was controlled to supply power to the grid in order to keep the V_{dc} at its allowable range as shown in Fig. 22.

Case 7: From t = 17 s to t = 19 s, the DC loads increased as shown in Fig. 16. Since the battery's SOC is in the desired operation region as shown in Fig. 21 and the V_{dc} voltage was kept at the nominal value of 7,100 V as shown in Fig. 22, the grid side converter power flow became zero as shown in Fig. 20.

Case 8: The last scenario was presented from t = 19 s to t = 24 s. The power generated from WT and PV was increased as shown in Fig. 14. It is shown in Fig. 21 that, the SOC approached the maximum charge limit while connected to the grid at t = 19 s. Therefore, the grid side converter controlled to the take extra power exceeding the load demand to prevent the battery from over charging. Hence the SOC was maintained at its safe upper limit as shown in Fig. 21.

4. Conclusions

In this paper, the application of FLC on DABSRC for the DCSG power system was proposed. In order to show the effectiveness of the power system, different simulation scenarios were analyzed and simulation results were presented. It has been shown that, the power system can work under different conditions as analyzed in the aforementioned cases. In its operation, the DCSG transferred power to and from the infinite grid for surplus and deficit, and stabilized the power in regards to RES power generation and load fluctuations. In this work, there was no specific case presenting the isolated mode of operation of the DCSG, but with the scenarios in which the results were presented, it can be determined that, the power system can withstand insolation mode as it resembles those scenarios in which the grid converter power flow was zero (Case 1, Case 3, Case 5 and Case 7).

References

[1] Aizebeokhai, A. P. 2009. "Global Warming and Climate Change: Realities, Uncertainties and Measures." *International Journal of Physical Sciences* 4 (13): 868-79.

[2] Samad, T., and Kiliccote, S. 2012. "Smart Grid Technologies and Applications for the Industrial Sector." *Computers and Chemical Engineering* 47 (4): 76-84.

[3] Wang, W., Xu, Y., and Khanna, M. 2011. "A Survey on the Communication Architectures in Smart Grid." *Computer Networks* 55 (15): 3604-29.

[4] Ito, Y., Yang, Z., and Hirofumi, A. 2009. "A Control Method for Small-Scale DC Power Systems Including Distributed Generators." *Electrical Engineering in Japan* 167 (2): 1236-42.

[5] Kurohane, K., Senjyu, T., Yona, A., Urasaki, N., Goya, T., and Funabashi, T. 2010. "A Hybrid Smart ac/dc Power System." *IEEE Transactions on Smart Grid* 1 (2): 199-204.

[6] Yamauchi, H., Kina, M., Kurohane, K., Uchida, K., Yona, A., and Senjyu, T. 2011. "Operation Principle of Multiple DC Smart Grids." In *Proceedings of the 2011 IEEE Ninth International Conference on PEDS (Power Electronics and Drive Systems)*, 304-9.

[7] Nassor, T., Ziadi, Z., Yona, A., Senjyu, T., and Abdel-Akher, M. 2012. "Comprehensive Analysis of DC Smart Grid Operation." In *Proceedings of the 2012 IEEE International PECon (Conference on Power and Energy)*, 880-5.

[8] Nassor, T. S., Kina, M., Senjyu, T., Yona, A., and Funabashi, T. 2012. "Operation of Multi DC Smart Grids Based on Renewable Energy Sources and Protection of DC Transmission Line." *International Journal of Emerging Electric Power Systems* 13 (3): 1553-779.

[9] Balamurugan, T., and Manoharam, S. 2012. "Fuzzy Controller Design Using Soft Switching Boost Converter for MPPT in Hybrid System." *International Journal of Soft Computing and Engineering* 2 (5): 87-94.

[10] Yong, Y., Xing, L., Shen, G., Zude, Z., and Jihong, W. 2008. "A Battery Charging Control Strategy for Renewable Energy Generation Systems." In *Proceedings of the WCE (World Congress on Engineering)*, 356-61.

[11] Neeraj, S., Bohn, T., Duoba, M., Lohse-Busch, H., and Sharer, P. 2007. "PHEV 'All Electric Range' and Fuel Economy in Charge Sustaining Mode for Low SOC Operation of the JCS VL41M Li-ion Battery Using Battery HIL." Argonne National Laboratory. Accessed July 04, 2015. http://www.transportation.anl.gov/pdfs/HV/463.pdf.

[12] Hu, W., Chen, Z., Wang, Y., and Wang, Z. 2008. "Wind Power Fluctuations Mitigation by DC-Link Voltage Control of Variable Speed Wind Turbines." In *Proceedings of the 43rd International UPEC (Universities Power Engineering Conference)*, 1-5.

[13] Haque, M., Muttaqi, K., and Negnevitsky, M. 2008. "Control of a Stand Alone Variable Speed Wind Turbine with a Permanent Magnet Synchronous Generator." In *Proceedings of the Power and Energy Society General Meeting—Conversion and Delivery of Electrical Energy in the 21st Century*, 1-9.

[14] Rosyadi, M., Muyeen, S. M., Takahashi, R., and Tamura, J. 2012. "A Design Fuzzy Logic Controller for a Permanent Magnet Wind Generator to Enhance the Dynamic Stability of Wind Farms." *Applied Sciences* 2 (5): 780-800.

[15] Wu, F., Zhang, X. P., and Ju, P. 2009. "Small Signal Stability Analysis and Control of the Wind Turbine with the Direct-Drive Permanent Magnet Generator Integrated to the Grid." *Electric Power Systems Research* 79 (12): 1661-7.

[16] Hansen, A. D., and Michalke, G. 2008. "Modelling and Control of Variable-Speed Multi-pole Permanent Magnet Synchronous Generator Wind Turbine." *Wind Energy* 11 (5): 537-54.

[17] Senjyu, T., Sakamoto, R., Urasaki, N., Funabashi, T., Fujita, H., and Sekine, H. 2006. "Output Power Leveling of Wind Turbine Generator for All Operating Regions by Pitch Angle Control." *IEEE Transactions on Energy Conversion* 21 (2): 467-75.

[18] Rahmani, R., Seyedmahmoudian, M., Mekhilef, S., and Yusof, R. 2013. "Implementation of Fuzzy Logic Maximum Power Point Tracking Controller for Photovoltaic System." *Journal of Electrical and Electronics Engineering* 10 (3): 209-18.

[19] Chung, H. H., Tse, K. K., Hui, S., Mok, C. M., and Ho, M. T. 2003. "A Novel Maximum Power Point Tracking Technique for Solar Panels Using a Sepic or Cuk Converter." *IEEE Transactions on Power Electronics* 18 (3): 717-24.

[20] Walker, G. 2001. "Evaluating MPPT Converter Topologies Using a MATLAB PV Model." *Journal of Electrical and Electronics Engineering* 21 (1): 49-56.

[21] Agarwal, V., and Vishwakarma, A. 2009. "A Modified Method for Maximum Power Point Tracking of PV Cell." *Journal of Electrical and Electronic Systems Research* 2 (June): 2161-5.

[22] Tremblay, O., Dessaint, L. A., and Dekkiche, A. I. 2007. "A Generic Battery Model for the Dynamic Simulation of Hybrid Electric Vehicles." In *Proceedings of the VPPC (Vehicle Power and Propulsion Conference)*, 284-9.

[23] Pang, S., Farrell, J., Du, J., and Barth, M. 2001. "Battery State-of-Charge Estimation." In *Proceedings of the American Control Conference*, 1644-9.

[24] Li, X., and Bhat, A. K. S. 2008. "AC Equivalent Circuit Analysis for High-Frequency Isolated Dual-Bridge Series Resonant DC/DC Converter." In *Proceedings of the PESC (Power Electronics Specialists Conference)*, 238-44.

[25] Li, X., and Bhat, A. K. S. 2010. "Analysis and Design of High-Frequency Isolated Dual-Bridge Series Resonant DC/DC Converter." *IEEE Transactions on Power Electronics* 25 (4): 850-62.

[26] Krismer, F., Round, S., and Kolar, J. 2006. “Performance Optimization of a High Current Dual Active Bridge with a Wide Operating Voltage Range.” In *Proceedings of the 37th IEEE PESC (Power Electronics Specialists Conference)*, 1-7.

[27] Biela, J., Aggeler, D., Inoue, S., Akagi, H., and Kolar, J. 2008. “Bi-directional Isolated DC-DC Converter for Next-Generation Power Distribution Comparison of Converters Using Si and SiC Devices.” *The Institute of Electrical Engineers of Japan* 128 (7): 1-10.

Journal of Energy and Power Engineering 9 (2015) 753-759
doi: 10.17265/1934-8975/2015.08.009

Operational Skill and TNA (Training Needs Analysis) for Generation Power Plant

Aouda Arfoa[1], Qais Alsafasfeh[1], Omar Alsaraereh[2] and Jaber Alrawahi[3]

1. Power and Mechatronics Engineering Department, Tafila Technical University, Tafila 66110, Jordan

2. Electrical Engineering Department, Hashemite University, Zarqa 13133, Jordan

3. Wadi Al Jizzi Power Co., Sohar 322, Oman

Received: May 26, 2015 / Accepted: June 19, 2015 / Published: August 31, 2015.

Abstract: Training needs analysis is the preliminary step in a cyclical process which adds to the overall training and progress strategy of staff in a generation power plant or a professional group, questionnaires were distributed among WAJPCO (Wadi Al Jizzi Power Company) staff and their responses were used to conduct a training need and gap analyses with a view to identify the operational skill and the training needs of the generation power plant, the time and travel commitment the industry is willing to invest in employee training, and an understanding of what skills are considered specific to lumber manufacturing and what can be combined with the needs of other industries and taught locally.

Key words: Training needs analysis, power plant, operational skill.

1. Introduction

For a learning generation power plant to grow and develop, its staff must have the necessary operational skills and knowledge to deliver the services required, both now and in the future. To ensure that workforce stays fit for purpose and suitable for repetition, a generation power plant must have an effective training and progress strategy that addresses any performance gaps. Many researchers started working with TNA (training needs analysis) concept with many services like nursing [1], business [2], industry [3] and general education [4], also in Ref. [5], a case study and importance performance analysis are adopted to identify competency gaps. Based on the managerial competency framework, the importance of competency is determined using the Fuzzy Delphi, and the performance is estimated via 360 degree feedback, moreover the TNA is very helpful for the academic purpose at university level in Ref. [6], the outcomes of this study will be crucial to guide UiTM's (Universiti Teknologi MARA's) administration towards the direction of achieving a sustainable high quality academic staff development environment. In Ref. [7], TNA was conducted to enhance the operational skill of the manufacturer operators a three-step method is presented to solve the problem. The method includes key position analysis, key motion cells analysis and key skill cells analysis. Goldstein model, competency model and gap analysis model are introduced as methods to evaluate training needs process, and the practical process about training needs analysis is illustrated in detail, task competency analysis and personnel analysis process was presented in Ref. [8]. This study was aimed at enabling the ET (expert team) gain an indepth understanding of the required fast track capacity building requirements. The situational analysis aimed at giving the ET a quick synopsis of the base line performance in the areas of gas turbine power generation: major components design and construction; gas turbine support systems and major maintenance; operation of gas turbines; control & protection systems

Corresponding author: Qais Alsafasfeh, Ph.D., research fields: power system, renewable energy and nonlinear systems. E-mail: qsafasfeh@ttu.edu.jo, qshashim@yahoo.com.

and power plant controls.

The TNA was aimed at identifying the core training needs in the above areas as well as identification of any essential complimentary skill requirements such as basic IT and management. The whole exercise was aimed at gathering adequate material that would be useful in the designing of the training modules and the capacity building programme as a whole

The specific objectives of training needs assessment were to:

- get baseline information in the areas of gas turbine power generation: major components design and construction; gas turbine support systems and major maintenance; operation of gas turbines; control & protection systems and power plant controls;
- identify core needs in the areas of gas turbine power generation: major components design and construction; gas turbine support systems and major maintenance; operation of gas turbines; control & protection systems and power plant controls. As well as any essential complimentary skills such as IT and management;
- assistance and resources needed. What additional resources are needed to expand capacity?
- preferences regarding training format, length, and travel distance. How should trainings be delivered and where should they be held?

2. Methodology

The study area focused on WAJPCO (Wadi Al Jizzi Power Company), the study start with maintenance department, operation department, planning and procurements and stores department, visits were carried over a period of one week between December 4th-9th, 2014, the methods used to gather critical baseline information to assess the training needs and opportunities of power plant professionals throughout the state. In order to obtain this necessary information, the project team developed a comprehensive set of research questions that informed the creation of two surveys: training needs assessment survey, which targeted power plant professionals; indications for the needs of training, which targeted training courses. Both surveys were carried out as part of a larger effort to develop a comprehensive training plan for Wadi Al Jizzi Power Company, which is due to be released in late December, 2013. More detailed descriptions of the methodology used for each survey is described below. survey containing 65 questions (appendix A and B) was developed by the Petra training group to collect data from various professional groups in Wadi Al Jizzi Power Company in order to determine their familiarity with statewide training needs in power company. Interviews were held with key informants, members Wadi Al Jizzi Power Company and other leaders, staff of maintenance department, operation department, planning and procurements and stores. Focus group discussions were also held with key staff.

The number of responders for each question varies because responses to certain questions throughout the survey routed the responder to a specific set of questions (referred to as branching) and because some responders declined to answer all questions they were asked.

The ET visited the Wadi Al Jizzi Power Company, a simple indications for the needs of training questionnaire was developed and administered to about 70% of the total staff per utility (appendix A and B). The questionnaire was designed in such a way that basic information could be acquired on the skills, qualification, abilities and training needs of the individual.

Interviews were held with key informants, members Wadi Al Jizzi Power Company and other leaders, staff of maintenance department, operation department, planning and procurements and stores. Focus group discussions were also held with key staff available records, databases and documents were reviewed and an assessment made of the processes and management systems in place. The sampling of data reviewed was done randomly but covered information in place over a period of at least two years where applicable. Soft

copies of reports were obtained where possible.

3. Results and Analysis

A questionnaire was used to provide the training needs perception of the staff. The questionnaire was administered by the ET by direct interview and group conference. This needs assessment report is the first reporting of the findings of the needs assessment survey and therefore the full findings of that survey are contained herein. The questionnaire also focused on major areas of training that were pre-determined. The answers provided by the staff give their own perception of their training needs. These are summarized in Figs. 1-7.

The expert team carried out field visits to assess the on-ground condition of operations and assess the areas which were in need for plant personnel to be trained. The field visits targeted maintenance department, operation department, planning and procurements and stores. A check list provided baseline information

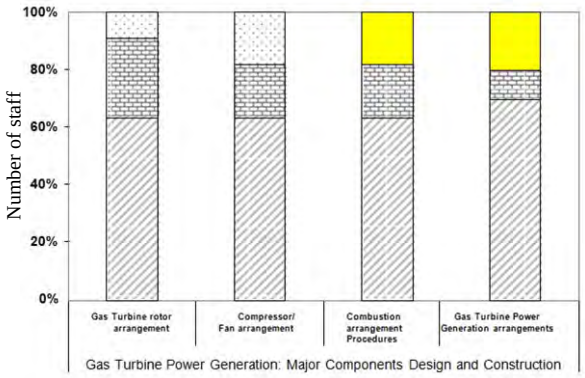

Fig. 1 Staff training aspirations in gas turbine power generation: major components design and construction.

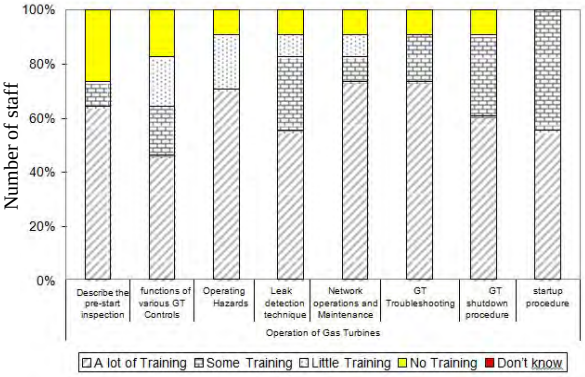

Fig. 2 Staff training aspirations in operation of gas turbine.

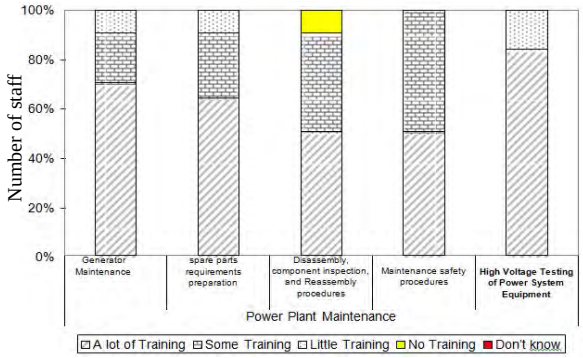

(a)

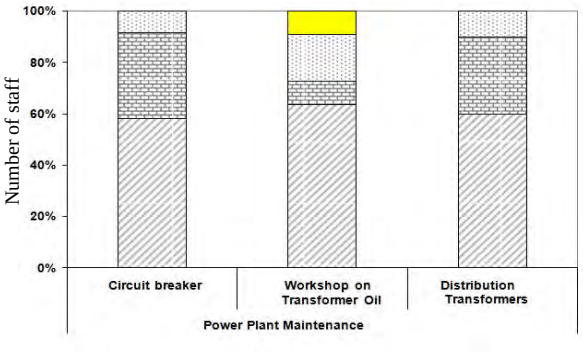

(b)

Fig. 3 Staff training aspirations in power plant maintenance.

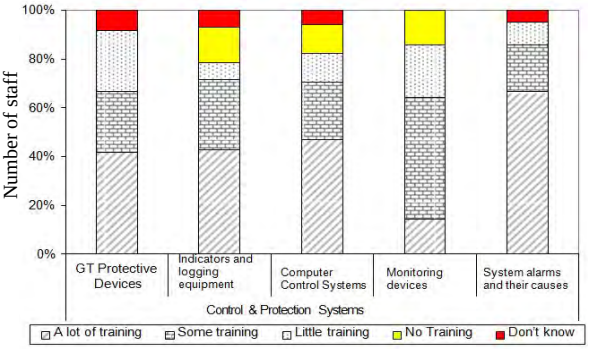

Fig. 4 Staff training aspirations in control & protection systems.

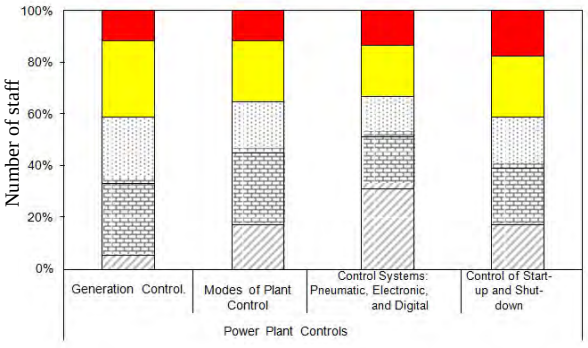

Fig. 5 Staff training aspirations in power plant controls.

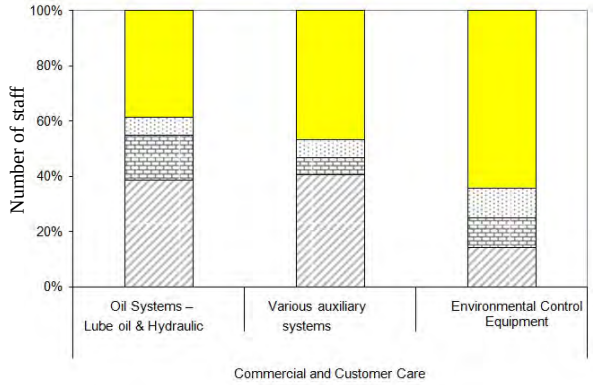

Fig. 6 Staff training aspirations in maintenance.

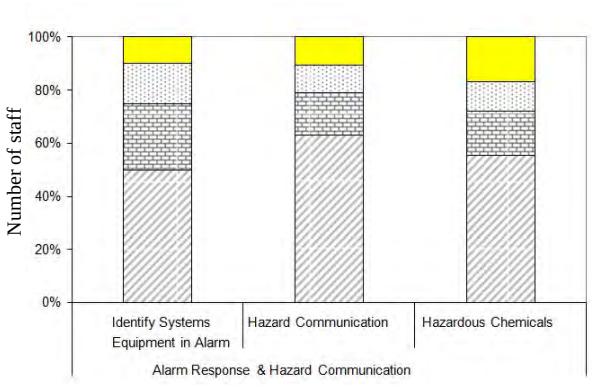

Fig. 7 Staff training aspirations in alarm response & hazard communication.

further enhanced by focused group discussions and interviews. The major findings are described below during the survey, filling the questionnaires and interviews with members of staff (with different ranks) we noticed the following:

- There is a huge gap between the main supervisor and the team working under his supervision. This was obvious in many departments and causing a very weak relationship between the supervisor and his team which consequently lead to lack of trust and losing the soul of teamwork;
- Most of the times employers talk about training and focusing on practical training;
- During filling the questionnaires, we have noted that, there is a sever weakness in speaking and writing English language. It is very important to concentrate on this issue since the staff deal with English manuals and use standard English expressions and training courses for any new equipment usually lectured in English;
- Responders have serious concerns about a number issues, topping the list is cost of maintenance and operations/maintenance. Developing regionally specific case studies could help address some of these concerns;
- The defect report covers the period from December 18, 2010 to November 20, 2013 (approximately 3 years) with total number of 1,060 defects. Around 413 defects have been solved by replacing new part. The replaced parts included the following Table 1.

It can be noted that, the aforementioned parts include some traditional consumables such as fuses, gaskets, belts and isolators. Other major parts included thermocouples, motors, radiators, pumps, tap changers, compressors and torque convertors need rigorous investigation to check the main factors behind repetitive replacing of these parts and proper staff skills for examining and servicing.

Other major findings in Wadi Al-Jizzi Power Station are water leak and oil leak in different locations. Water leak was mainly concentrated and monotonous in the following locations.

Main cooling water pump and aux pump, diesel engine cooler system, Tower 1 stage 5 of radiators, cooling radiator under fans (1-6), VTR1 body joint gasket, cooling water radiator, support leg GT6, side, atomizing air cooler, battery cells, heavy water leak underground from hydrant line near GTS (north side) also oil leak was concentrated and monotonous as well in the following locations.

Diesel engine turbo charger, diesel engine cylinder head cover gasket, accessory gearbox in many parts

Table 1 list of replaced parts.

Thermocouples	Pump contactor	Motor	Fans
Gasket	Fuses	Isolator	Tap changer
Fuel nozzle	Air cooler	Radiator core	belts
Air filters	Motor pump	Carbon brushes	
Flame detectors	Injectors	Torque convertors	
Switches	Compressors		

such as lube oil pump side, drain line pipe, turbine cover and load gearbox (upper case), lube oil cooler 2, distillate of base filter (heavy leak), heat exchanger, HYD (hydraulic filter division) filter cover, exciter bearing, 11 kV side cable box, starting motor, booster air compressor mechanical seal oil, IGV (inlet guide vane) solenoid valve, LO (radiative cooling) cooler east side, transformer gasket and generator bearing.

The survey results show important key findings, as well as gaps that will need to be addressed in the next phase of the project team's work. Among the key findings and gaps are the following sections.

3.1 Gas Turbine Power Generation: Major Components Design and Construction

The questionnaire reflected the following facts on the subject of gas turbine power generation:

- gas turbine rotor arrangement: 90% of the staff needs a lot of training in this aspect and the rest needs slight training;
- compressor/fan arrangement: 80% of the staff needs a lot of training in this aspect and the rest needs slight training;
- combustion arrangement procedures: 80% of the staff needs a lot of training in this aspect and the rest does not need any training;
- gas turbine power generation arrangements: around 76% of the staff needs a lot of training and the rest does not need any training.

Recommendations: The ET recommends an extensive training in all aspects of gas turbine power generation since the questionnaire revealed that more than 80% of the staff requires that.

3.2 Operation of Gas Turbines

The questionnaire reflected the following facts on the subject of operation of gas turbines:

- describe the pre-start inspection: 75% of the staff needs a lot of training in this aspect and the rest does not need any training;
- functions of various GT controls: around 62% of the staff needs a lot of training and 38% requires very little training;
- operating hazards: 70% of the staff requires a lot of training and 30% requires slight training;
- leak detection technique: around 84% of the staff requires a lot of training and the rest requires very little training;
- network operations and maintenance: around 84% of the staff requires a lot of training and the rest requires very little training;
- GT troubleshooting: more than 90% of the staff requires a lot of training in this aspect;
- GT shutdown procedure: more than 90% of the staff requires a lot of training in this aspect;
- startup procedure: 50% of staff requires a lot of training and 50% requires some training.

Recommendations: The ET recommends an extensive training in operations of gas turbines since the questionnaire analysis revealed that more than 82% of the staff requires that.

3.3 Power Plant Maintenance

The questionnaire reflected the following facts on the subject of power plant maintenance:

- generator maintenance: 90% of the staff requires a lot of training and the rest requires very little training;
- spare parts requirements preparation: 90% of the staff requires a lot of training and the rest requires very little training;
- disassembly component inspection and reassembly procedure: 90% of the staff requires a lot of training and the rest requires no training;
- maintenance safety procedures: 50% of staff requires a lot of training and 50% requires some training;
- high voltage testing of power system equipment: 85% of staff requires a lot of training and the rest requires little training;
- circuit breaker: 95% of the staff requires a lot of training and the rest requires very little training;

- workshop on transformer oil: 70% of the staff requires a lot of training and around 30% needs very little training;
- distribution transformers: 95% of the staff requires a lot of training and the rest requires very little training.

Recommendations*:* The ET recommends an extensive training in power plant maintenance aspects since the questionnaire analysis revealed that more than 90% of the staff requires that.

3.4 Control and Protection

The questionnaire reflected the following facts on the subject of control and protection systems:

- GT protective devices: 65% of the staff requires a lot of training, 30% requires very little training and 5% does not know;
- indicators and logging equipment: 78% of the staff requires a lot of training, 14% requires no training and around 8% does not know.
- computer control systems: 85% of the staff requires a lot of training, 10% requires no training and 5% does not know;
- monitoring devices: 85% of the staff requires some training and the rest does not need any training;
- systems alarms and their causes: 85% of the staff requires a lot of training, 10% very little training and 5% does not know.

Recommendations: The ET recommends training in control and protection systems aspects since the questionnaire analysis revealed that more than 79% of the staff requires that.

3.5 Power Plant Control

The questionnaire reflected the following facts on the subject of power plant controls:

- generation control: approximately 40% of the staff requires some training, 20% little training, 30% does not need any training and 10% does not know;
- modes of plant control: 48% of the staff requires some training, 15% little training, 25% requires no training and 12% does not know;
- control systems (pneumatic, electronic and digital): 50% of the staff requires training, 15% little training, 20% does not need any training and 15% does not know;
- control of startup and shutdown: 40% of the staff requires training, 15% little training, 25% does not need any training and 20% does not know.

Recommendations: The ET recommends light training in power plant controls aspects since the questionnaire analysis revealed that around 50% of the staff requires that.

3.6 Gas Turbine Support Systems

The questionnaire reflected the following facts on the subject of

- oil systems—lube oil & hydraulic: 60% of the staff requires a lot of training and 40% does not need any training;
- various auxiliary systems: 50% of the staff requires a lot of training and 50% does not need any training;
- environmental control equipment: 30% of the staff requires training and 70% does not need any training.

Recommendations: The ET recommends light training in GT support systems aspects since the questionnaire analysis revealed that around 47% of the staff requires that.

3.7 Alarm Response & Hazard Communication

The questionnaire reflected the following facts on the subject of:

- identify systems equipment in alarm: 90% of the staff requires a lot of training and 10% does not need any training;
- hazard communication: 90% of the staff requires a lot of training and 10% does not need any training;
- hazard chemicals: 80% of the staff requires a lot of training and 20% does not need any training.

Recommendations: The ET recommends an extensive

training in alarm response and hazard communication aspects since the questionnaire analysis revealed that around 87% of the staff requires that.

3.8 Safety in Power Plant

The questionnaire reflected the following facts on the subject of:

- fire protection: 40% of the staff requires training and 60% does not need any training;
- fire aid: 40% of the staff requires training and 60% does not need any training;
- safety operation: 45% of the staff requires training and 55% does not need any training;
- abnormal operation and record equipment history: 35% of the staff requires training and 65% does not need any training.

Recommendations: The ET recommends a light training in safety aspects since the questionnaire analysis revealed that around 41% of the staff requires.

4. Conclusions

The results from the study indicated that, there are five different categories of power plant staff development programs that are anticipated by the respondents in an effort to improve the productivity and efficiency of the power plant. In light of the results, it is recommended that, WAJPCO established power plant staff development plan based on the priorities listed by the respondents, taking into consideration the differences between the various power plant clusters, as a next step we will conduct the TNA based on KPI (key performance indicator).

References

[1] Dinah, G., Daniel, K., Isabel, W., and Jayne, C. 2004. "Training Needs Analysis. A Literature Review and Reappraisal." *International Journal of Nursing Studies* 41 (5): 471-86.

[2] Pearson, G. A. 1987. "Business Ethics: Implications for Continuing Education/Staff Development Practice." *Journal of Continuing Education in Nursing* 18 (1): 20-4.

[3] Boydell, T. H. 1976. *The Identification of Training Needs.* Portsmouth: British Association for Commercial and Industrial Education, Grosvenor Press.

[4] Walklin, L. 1991. *The Assessment of Performance and Competence: A Handbook for Teachers and Trainers.* London: Stanley Thornes.

[5] Jeou, S. H., and Lin, L. 2013. "Training Needs Assessment in a Hotel Using 360 Degree Feedback to Develop Competency-Based Training Programs." *Journal of Hospitality and Tourism Management* 20: 61-7.

[6] Rohana, O., Fauziah, N., Muna, K. S., Zubaidah, Z. A., and Ismie, R. 2011. "Academic Staff Development in Universiti Teknologi MARA—A Perspective Using Training Need Analysis." Presented at the 2011 ISBEIA (IEEE Symposium on Business, Engineering and Industrial Applications), Langkawi, Malaysia.

[7] Zheng, C., Zhanwen, N., and Pengfei, W. 2011. "Operational Skill Training Needs Analysis for Manufacturing Industry." Presented at the 2011 ISBEIA (IEEE Symposium on Business, Engineering and Industrial Applications), Langkawi, Malaysia.

[8] Jianping, H. 2011. "Training Needs Analysis of Talent Intermediary Organization Based on Goldstein Model." Presented at the 2011 ISBEIA (IEEE Symposium on Business, Engineering and Industrial Applications), Langkawi, Malaysia.

Call for Papers

Dear author,

This is *Journal of Energy and Power Engineering* (ISSN1934-8975), created in Dec. 2007. We are interested in various kinds of professional papers about energy and power. The *Journal of Energy and Power Engineering*, a monthly professional academic journal, is striving to provide the best platform for researchers and scholars worldwide to exchange their latest findings and results.

Current Columns Involve

Thermal Science; Fluid Mechanics; Energy and Environment; Power System and Automation; Power Electronic; High Voltage and Pulse Power; Sustainable Energy.

Information for Authors

1. The manuscript should be original, and has not been published previously. Please don't submit material that is currently being considered by another journal.
2. Manuscripts may be 3000-8000 words or longer if approved by the editor, including abstract, text, tables, footnotes, appendixes, and references. The title should not be exceeding 15 words, and abstract should not be exceeding 150 words. 3-8 keywords required.
3. The manuscript should be in MS Word format, submitted as an email attachment to our email address.

Editorial Procedures

All papers considered appropriate for this journal are reviewed anonymously by at least two outside reviewers. The review process usually takes 4-5 weeks. Papers are accepted for publication subject to no substantive, stylistic editing. The Editor reserves the right to make any necessary changes in the papers, or request the author to do so, or reject the paper submitted. A copy of the edited paper along with the first proofs will be sent to the author for proofreading. They should be corrected and returned to the Editor within seven days. Once the final version of the paper has been accepted, authors are requested not to make further changes to the text.

Submitting of Manuscripts

All manuscripts submitted will be considered for publication. Please visit our website at www.davidpublisher.com for our automatic paper submission systems or as an email attachment to energy@davidpublishing.org, energy@davidpublishing.com, energy-power@hotmail.com and energy@davidpublishing.net.

Journal of Energy and Power Engineering
David Publishing Company
Tel: 001-323-984-7526, 001-323-410-1082; Fax: 001-323-984-7374

Journal of Energy and Power Engineering
Volume 9, Number 8, August 2015

David Publishing Company
1840 Industrial Drive, Suite 160, Libertyville, IL 60048, USA
Tel: 1-323-984-7526, 323-410-1082; Fax: 1-323-984-7374, 323-908-0457
http://www.davidpublisher.com, www.davidpublisher.org
energy@davidpublishing.com, energy@davidpublishing.org, energy-power@hotmail.com

ISSN 1934-8975